Beyond the Standard Models:
Supersymmetric Parameter Scans
&
Waves in Modified Gravity

Jan Øye Lindroos

Dissertation for the degree of Philosophiae Doctor (PhD)

Department of Physics and Technology
University of Bergen

February 25, 2016

Abstract

Two different extensions to the current paradigm of physics is considered, supersymmetric extensions to the standard model of particle physics and modifications to Einstein's general theory of relativity.

In part I we present searches for non-excluded regions of the cMSSM parameter space which could potentially be discovered in searches for SUSY τ events in the ATLAS detector. One gridded scan, pre Higgs discovery, and one mcmc scan taking into account the newly discovered Higgs boson with a mass 125 GeV, presented in the form of a paper. Benchmark models for optimizing the sensitivity of the ATLAS 1 τ analysis for these regions are constructed . We also present the SUSYScanner package, which contains the algorithms implemented for these scans. In particular a multichain adaptive markov chain monte carlo (mcmc) algorithm was developed and a SUSY model responsible for calculating model likelihood. Multiple external packages are used to calculate the observables needed to construct a model likelihood based on current experimental constraints and LHC phenomenology.

In part II, we investigate the propagation of scalar waves induced by matter sources in the context of scalar-tensor theories of gravity with screening mechanisms. We find that effective mass terms and non-linearities in the equation of motion lead to propagation and dispersion velocities significantly different from the speed of light. In particular we find that the propagation of these waves is determined by the group velocity which depends on both the effective mass and the frequency of the signal. This might have direct impact on the behavior and dynamics of nonlinear structures within modified gravity theories with screening. We also discuss potential physical sources of such waves and the relation to the scalar speed of sound used in cosmological perturbation theory.

Acknowledgment

This thesis would not have been possible without the help and support of many:

- First and foremost I would like to thank my thesis advisors Heidi Sandaker, David Mota and Per Osland. Without your knowledge, support, and encouragement this thesis would not have been possible. I'm especially grateful to Heidi for giving me the freedom to explore different areas of research, and for always having my back. I would have given up many times over if it wasn't for your help. I'm also very grateful to David for giving me the opportunity to work on some really interesting projects, and for allowing me to come to Oslo and making me feel welcome.
- Secondly I would like to thank my other collaborators Anna Lipniacka, Thomas Burgess, and Claudio Llinares. You have taught me a lot and it has been a pleasure and a privilege to work with you.
- I would also like to thank my colleagues in Bergen and Oslo for making this a pleasant experience. In particular Ørjan Dale for putting up with me as an office mate, and to Heidi, David, Trygve Buanes, Bertrand Martin, Inga Strümke and Lillian Smestad for proof reading my thesis. I'm very grateful. Thanks also to Henrik Oppen for helping me debug the code.
- Finally, a big thank you to my parents for continued support over the years.

THANK YOU!

Contents

Notation

The conventions used in this thesis closely follow [73]

- **Units**

  Natural units are used throughout

  $$\hbar \equiv c \equiv 1 \quad , \quad M_{Pl} \equiv \frac{1}{\sqrt{8\pi G}} \tag{1}$$

  In these units length, time, mass and energy can all be expressed in the same units

  $$[E] = [m] = [l^{-1}] = [t^{-1}] \tag{2}$$

- **Index Notation**

  Einsteins summation convention is used where equal upper and lower indices are summed over

  $$A^\mu A_\mu \equiv \sum_\mu A_\mu A^\mu \tag{3}$$

  If A_μ and A^μ are trivially related by a euclidean metric, index placement is a matter of convenience. In these case, $A_\mu A_\mu$ and $A_\mu A^\mu$ should be taken to mean the same thing.

- **Spacetime conventions**

  A general spacetime metric is denoted by $g_{\mu\nu}$, and denote the special case of the Minkowski metric by $\eta_{\mu\nu}$. We use the metric signature

  $$\text{sign}\,(g_{\mu\nu}) = (-1, 1, 1, 1)$$

  and denote the determinant of the metric by $g \equiv \det g_{\mu\nu}$. The inverse metric is written $g^{\mu\nu}$ and can be used in conjunction with the metric to raise and lower spacetime indices

$$A^\mu = g^{\mu\nu} A_\nu \quad , \quad A_\mu = g_{\mu\nu} A^\nu \tag{4}$$

The Spacetime position, momentum and derivative four vectors, $x^\mu, p^\mu, \partial_\mu$, are defined by

$$x^\mu = (t, x_i) \quad , \quad p^\mu = (E, p^i) \quad , \quad \partial_\mu = (\partial_t, \partial_{x_i}) \tag{5}$$

We use several different short hands for the differential operator

$$\frac{\partial A^\mu}{\partial x^\nu} = \partial_\nu A^\mu = A^\mu{}_{,\nu} \tag{6}$$

This convention is sometimes also used for non-spacetime derivatives, both for partial and total derivatives in situations where the meaning is clear from the context.

- **Spinors**

The standard symbol used to denote Dirac fermions is Ψ, with ψ and $\eta^\dagger$ used describing left and right chiral fermions respectively

$$\Psi = \begin{pmatrix} \psi_\alpha \\ \eta^{\dagger\dot{\alpha}} \end{pmatrix} \quad , \quad \bar{\Psi} = \Psi^\dagger \gamma^0 = \begin{pmatrix} \eta^\alpha, \psi^\dagger_{\dot{\alpha}} \end{pmatrix} \tag{7}$$

In this representation the gamma matrices can be written

$$\gamma^\mu = \begin{pmatrix} 0 & \sigma^\mu \\ \bar{\sigma}^\mu & 0 \end{pmatrix} \quad , \quad \gamma^5 = \begin{pmatrix} -1 & 0 \\ 0 & 1 \end{pmatrix} \quad , \quad \sigma^\mu = \begin{pmatrix} 1, \sigma^k \end{pmatrix} \tag{8}$$

Where $\sigma^k = -\bar{\sigma}^k$ are the three Pauli matrices

$$\sigma_1 = \begin{pmatrix} 0 & 1 \\ 1 & 0 \end{pmatrix} \quad , \quad \sigma_2 = \begin{pmatrix} 0 & -i \\ i & 0 \end{pmatrix} \quad , \quad \sigma^3 = \begin{pmatrix} 1 & 0 \\ 0 & -1 \end{pmatrix}$$

In chapter 2, we also represent the left and right chiral fermions in terms of Dirac spinors Ψ_L and Ψ_R

$$\Psi_L = \frac{1 - \gamma^5}{2} \Psi = \begin{pmatrix} \psi_\alpha \\ 0 \end{pmatrix} \quad , \quad \Psi_R = \frac{1 + \gamma^5}{2} \Psi = \begin{pmatrix} 0 \\ \eta^{\dagger\dot{\alpha}} \end{pmatrix} \tag{9}$$

The indices of the Weyl fermions $\psi_\alpha, \bar{\eta}^{\dot{\alpha}}$ can be raised and lowered using the antisymmetric spinor metrics $\epsilon_{\alpha\beta}$ and $\epsilon_{\dot{\alpha}\dot{\beta}}$, together with their inverses $\epsilon^{\alpha\beta}, \epsilon^{\dot{\alpha}\dot{\beta}}$. By convention $\epsilon^{12} = 1$ and

$$\psi_\alpha = \epsilon_{\alpha\beta} \psi^\beta \quad , \quad \psi^\alpha = \epsilon^{\alpha\beta} \psi_\beta \quad , \quad \bar{\eta}^{\dot{\alpha}} = \epsilon^{\dot{\alpha}\dot{\beta}} \bar{\eta}_{\dot{\beta}} \quad , \quad \bar{\eta}_{\dot{\alpha}} = \epsilon_{\dot{\alpha}\dot{\beta}} \bar{\eta}^{\dot{\beta}} \tag{10}$$

Indices contracted as ${}^{\alpha}{}_{\alpha}$, ${}_{\dot{\alpha}}{}^{\dot{\alpha}}$ are suppressed

$$\psi\chi = \psi^{\alpha}\chi_{\alpha} \quad , \quad \bar{\eta}\bar{\zeta} = \bar{\eta}_{\dot{\alpha}}\bar{\zeta}^{\dot{\alpha}} \tag{11}$$

With this notation, the Dirac Lagrangian in terms of Weyl spinors can be written up to total derivatives

$$\bar{\Psi}\gamma^{\mu}\partial_{\mu}\Psi - m\bar{\Psi}\Psi = \psi^{\dagger}\bar{\sigma}^{\mu}\partial_{\mu}\psi + \eta^{\dagger}\bar{\sigma}^{\mu}\partial_{\mu}\eta - m\left(\psi\eta + \psi^{\dagger}\eta^{\dagger}\right) \tag{12}$$

Chapter 1

Introduction

Einstein's theory of General Relativity (GR) is the foundation of our modern description of gravitational phenomena, ranging from stellar evolution and planetary dynamics to the evolution of the universe itself. However in order to fit observational data on galactic and cosmological scales it seems necessary to assume a universe dominated by two new forms of energy, called dark energy and dark matter, neither of which can be explained within the standard model of particle physics. Thus if Einstein's theory is correct on these scales one is forced to extend the standard model of particle physics. Low energy supersymmetry (SUSY) is one such extension which provides natural candidates for dark matter in addition to improve on the discrepancy between the observed amount of dark energy and standard model estimates. One of the main goals of the Large Hadron Collider at CERN is to look for SUSY, but due to a large number of new parameters, these models are very difficult to constrain. The main part of my thesis is dedicated to developing tools for finding regions of SUSY parameter space which are consistent with the observed dark matter abundance and other constraints, while being potentially observable at the LHC. This work will be the focus of part I of this thesis.

The fact that we have yet to observe dark matter, other than through gravitational interactions, despite major efforts being made, could be an indication that the inferred dark matter is really a result of modifications to the gravitational sector rather than the matter sector. However, GR has been tested to high accuracy here on earth and in the solar systems, so in order for such modifications to be viable the associated effects must somehow be screened on these scales, while still being able to explain observations on galactic and cosmological scales. Models exhibiting such screening mechanisms are usually referred to as Screened Modified Gravity (SMG). While realistic models for dark matter seem to require rather complicated extensions of GR involving new vector, scalar and tensor fields, simpler extensions involving only scalars provide useful toy models in addition to providing potential dark energy candidates. Screened modified gravity has been studied thoroughly in recent years, but mostly in the static and quasi-static regimes, where dynamical effects in the scalar sector is neglected. Such dynamical effects is the focus of part II of this thesis, with emphasis on wave propagation.

The thesis is structured around two papers: The first paper [37], titled *Finding viable Models in SUSY Parameter Spaces with Signal Specific Discovery Potential* and published in JHEP, resulted from a collaboration with Thomas Burgess, Anna Lipniacka and Heidi Sandaker. It presents an mcmc based scan over the cMSSM parameter space looking for regions interesting from the perspective of an experimental analysis involving τ's. Part I is therefore dedicated to supersymmetric parameter scans, and starts with a review of the standard model and supersymmetry in chapters 2 and 3. This is followed by an overview of the work done related to SUSY parameter scans in chapter 4, focusing on unpublished results. Finally paper I is presented. My contribution to this paper was mainly the development and running of the mcmc code, in addition to being the corresponding author.

The second paper [71], titled *Wave Propagation in Modified Gravity* and published in Phys. Rev. D, presents work done in collaboration with Claudio Llinares and David F. Mota during a 6 month stay at the Institute of Theoretical Astrophysics, University of Oslo. It concerns the propagation of scalar waves from matter sources in modified theories of gravity with additional scalar fields and screening mechanisms with particular emphasis on the propagation velocity. Part II is therefore dedicated to Screened Modified Gravity, and starts with an overview of general relativity and the ΛCDM model in chapter 5. This is followed by brief introduction to modified theories of gravity in chapter 6, before presenting paper II. For this paper, I worked on both the theoretical and numerical analysis, and was also the corresponding author of the paper.

Part I

Supersymmetry

Chapter 2

The Standard Model

This chapter is mainly based on [81], [11]

The Standard Model of particle physics (SM) gives a unified description of how matter interacts on the smallest scales. It includes all the known forces except gravity and has been verified experimentally to great precision since its completion in the 1970's. The last piece of the puzzle, the Higgs boson, was discovered at the Large Hadron Collider (LHC) in 2012. The mathematical framework of the Standard Model is Quantum Field Theory (QFT), where the fundamental constituents are quantized fields, and particles corresponds to excitations in these fields. We start by briefly reviewing the particle content of the model, which is illustrated in fig. 2.1

Matter is described by spinor fields ($s = 1/2$) and comes in the form of quarks and leptons. The quarks interact primarily through the strong nuclear force and bind together in threes to form nucleons. The leptons on the other hand, only interact through the electromagnetic and weak nuclear forces. Furthermore the quarks and leptons are grouped into three families, which have the same structure, but differ in mass. The first family consists of the u (up) and d (down) quarks, which make up protons and neutrons, the electron e, which when combined with the former make up all the atoms in the periodic table, and the nearly massless and weakly interacting electron-neutrino ν_e needed to explain radioactive β-decay. The two additional families are needed to describe particles seen in high-energy colliders and cosmic rays. These particles are much heavier (apart from the neutrinos) and quickly decay into first family particles. Finally, for each particle relativity requires a corresponding antiparticle, which has the same mass but opposite charge.

Forces are described by vector fields ($s = 1$), and the quanta of the fields are known collectively as gauge bosons. The three forces included in the Standard Model are the electromagnetic force mediated by the massless photon, the weak forces mediated by the massive $W^{\pm}$ and Z-bosons and the strong force mediated by eight massless gluons.

The last constituent of the SM is the scalar Higgs field ($s = 0$) whose associated quanta

are called Higgs bosons. This scalar field is needed in the SM to generate masses for the matter particles and the weak gauge bosons.

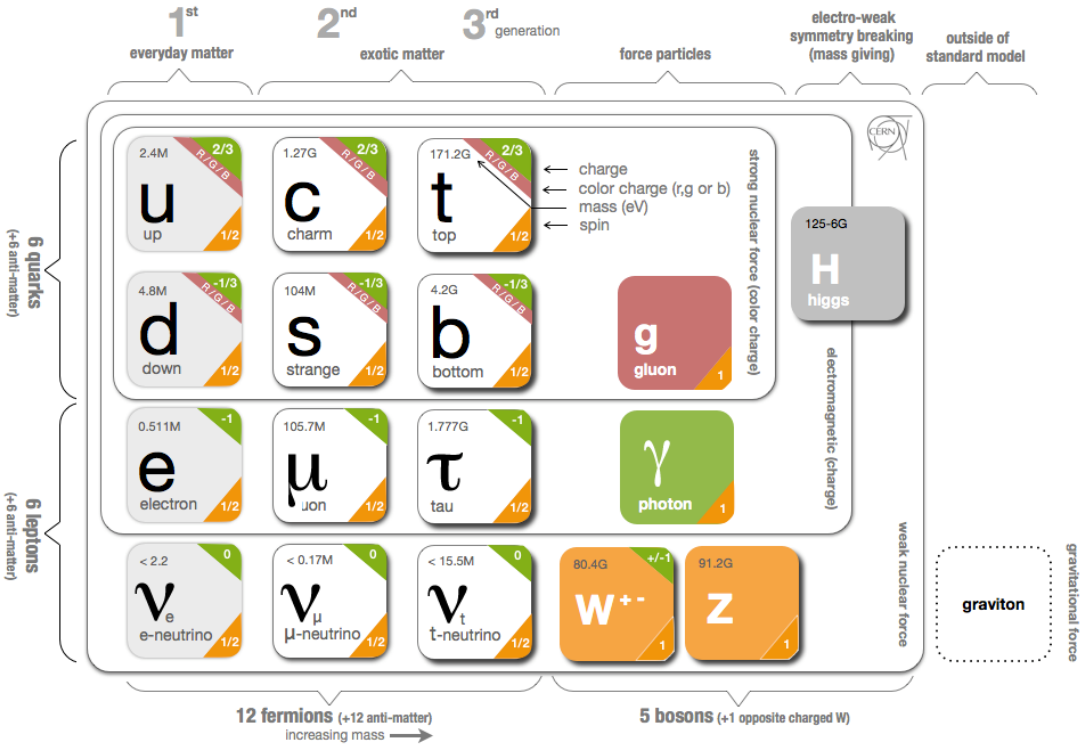

Figure 2.1: Particle content of the Standard Model together with their measured mass, charges and spins. The boxes in which the particles are embedded indicates the gauge boson couplings of different fermions. Taken from [54]

2.1 The Standard Model as a Gauge Theory

The SM is based on the principle of gauge invariance, meaning all interactions are constructed by taking continuous global symmetries of the free matter Lagrangian eq. (2.1)

$$\mathcal{L}_D = i\overline{\Psi}\gamma^\mu\partial_\mu\Psi - m\overline{\Psi}\Psi \tag{2.1}$$

and promoting them to local ones. The simplest example of a gauge theory is based on the invariance under global $U(1)$ transformations, which corresponds to a global change in the complex phase θ of a fermion field Ψ. Since the change is global, it commutes with the differential operator ∂_μ and cancels against the corresponding change in the conjugate field $\bar{\Psi}$, given by eq. (7). However if we allow the phase change to be a function of spacetime,

$\theta \to \theta(x^\mu)$, this is no longer true and the non-vanishing commutator produces a change in the Lagrangian of the form

$$\Psi \to e^{iq\theta(x)}\Psi \quad \Rightarrow \quad \delta\mathcal{L}_D = -q\overline{\Psi}\gamma^\mu\partial_\mu\theta(x)\Psi, \tag{2.2}$$

where q parametrizes the coupling strength. The invariance of $\mathcal{L}$ can be restored by introducing a new vector field, A^μ, which transforms as $\delta A = \partial_\mu\theta(x)$, and has a fermion coupling of the same form as $\delta\mathcal{L}$

$$\mathcal{L}_{int} = q\overline{\Psi}\gamma^\mu A_\mu\Psi, \tag{2.3}$$

To make the new field dynamic the Lagrangian also needs a gauge invariant kinetic term which can be constructed using the field strength tensor $F_{\mu\nu} = \partial_\mu A_\nu - \partial_\nu A_\mu$

$$\mathcal{L}_M = -\frac{1}{4}F^{\mu\nu}F_{\mu\nu}, \tag{2.4}$$

The full Lagrangian can now be neatly written by replacing the ordinary derivative operator ∂_μ with a covariant derivative ∇_μ that commutes with the gauge transformation

$$\partial_\mu \to \ \nabla_\mu = \partial_\mu - iqA_\mu \tag{2.5}$$

$$\mathcal{L}_D \to \mathcal{L}_{EM} = i\overline{\Psi}\gamma^\mu\nabla_\mu\Psi - m\overline{\Psi}\Psi - \frac{1}{4}F^{\mu\nu}F_{\mu\nu} \tag{2.6}$$

The resulting theory is quantum electrodynamics (QED), describing the electromagnetic interactions of fermions.

This prescription for constructing interacting theories can be generalized to more complicated internal symmetries which not only alter the phase of matter fields, but also transform them into each other. More specifically the gauge principle is generalized to $SU(N)$ transformations and the resulting theory is known as Yang-Mills theory. The starting point is again eq. (2.1)

$$\mathcal{L} = i\overline{\Psi}\gamma^\mu\partial_\mu\Psi - m\overline{\Psi}\Psi, \tag{2.7}$$

but now Ψ represents a collection of N fields[1], and the transformations take the form of $N \times N$-matrices

$$\mathbf{U} = e^{ig\theta^a\boldsymbol{\tau}_a} \tag{2.8}$$

By convention g now parametrizes the coupling strength[2], and $\boldsymbol{\tau}_a$ are the N^2-1 generators of $SU(N)$ defined by the commutation relations

[1] Boldface will be used to denote matrices in the group representations. It will be left implicit that the fields then become matrices

[2] In the $U(1)$ case $g\boldsymbol{\tau}^a$ would be the equivalent of q in the electromagnetic case

$$[\tau_a, \tau_b] = f_{abc}\tau_c, \tag{2.9}$$

where f_{abc} are the structure constants of the group. As in the $U(1)$ case, the local transformation $\overline{\Psi} \to \mathbf{U}(x)\overline{\Psi}$ leads to an extra term in the Lagrangian

$$\delta\mathcal{L} = i\overline{\Psi}\gamma^\mu\partial_\mu\mathbf{U}\Psi, \tag{2.10}$$

which is removed by replacing the ordinary derivative ∂_μ with a covariant derivative ∇_μ

$$\nabla_\mu = \partial_\mu - ig\mathbf{V}_\mu(x) \quad , \quad \mathbf{V}_\mu(x) = V_\mu^a(x)\boldsymbol{\tau}_a \tag{2.11}$$

This introduces one new gauge fields $\mathbf{V}_\mu$ for each generator of the group. Requiring ∇_μ to commute with the fermionic gauge transformations leads to gauge field transformations of the form

$$\mathbf{V}'_\mu = \mathbf{U}\mathbf{V}_\mu\mathbf{U}^\dagger - \frac{i}{g}\partial_\mu(\mathbf{U})\mathbf{U}^\dagger \tag{2.12}$$

where the first term is a result of the transformations being non-abelian. The kinetic term for the new gauge fields can be constructed from a generalized field strength tensors $\mathbf{F}_{\mu\nu} = F^a_{\mu\nu}\boldsymbol{\tau}_a$ defined by

$$[\nabla_\mu, \nabla_\nu]\Psi = ig\mathbf{F}_{\mu\nu}\Psi \quad \Rightarrow \quad F^a_{\mu\nu} = \partial_\mu V^a_\nu - \partial_\nu V^a_\mu - g f_{abc} V^b_\mu V^c_\nu \tag{2.13}$$

Again the non-abelian nature of the transformations introduce new terms, which couple the gauge fields to each other. This generalized field strength tensor transforms by a similarity transform

$$\mathbf{F}'_{\mu\nu} = \mathbf{U}^{-1}\mathbf{F}_{\mu\nu}\mathbf{U} \tag{2.14}$$

which leaves the trace of the matrix product invariant, and allows us to construct a gauge invariant kinetic term of the form

$$\mathcal{L}_{gauge} = -\frac{1}{2}\mathrm{Tr}(\mathbf{F}_{\mu\nu}\mathbf{F}^{\mu\nu}) = -\frac{1}{4}F^a_{\mu\nu}F^{\mu\nu}_a \tag{2.15}$$

The self-couplings appearing in the field strength tensor in non-abelian gauge theories give rise to novel properties such as asymptotic freedom and confinement. The full Lagrangian describing these theories is known as the Yang-Mills Lagrangian

$$\mathcal{L}_{YM} = i\overline{\Psi}\left(\gamma^\mu\nabla_\mu - m\right)\Psi - \frac{1}{4}F^a_{\mu\nu}\cdot F^{\mu\nu}_a \tag{2.16}$$

The Standard Model can now be constructed from the group $SU(3)_C \times SU(2)_L \times U(1)_Y$, where we use the notation of [73] and denote family indices by i. The groups $U(1)_Y$ and $SU(2)_L$ give rise to the electromagnetic and weak interactions through the four gauge fields, $B_\mu, W^0_\mu, W^\pm_\mu$. Left handed leptons L_i and quarks Q_i transform as doublets under $SU(2)_L$ and the right handed fermions u_i, d_i and e_i as singlets. The $U(1)$ charge of the different particles, called the hypercharge, is chosen so as to give the correct electric charge after symmetry breaking, see section 2.2. $SU(3)_C$ gives rise to the strong interactions mediated

by 8 gluons fields G_μ. Each quark comes in three different coloured states and transform as triplets under $SU(3)_C$. Using these naming convention the massless SM Lagrangian can be written as

$$\mathcal{L}_{SM} = i\bar{Q}_i\gamma^\mu\nabla_\mu Q_i + i\bar{u}_i\gamma^\mu\nabla_\mu u_i + i\bar{d}_i\gamma^\mu\nabla_\mu d_i + i\bar{L}_i\gamma^\mu\nabla_\mu L_i + i\bar{e}_i\gamma^\mu\nabla_\mu e_i \tag{2.17}$$

Where it is left implicit that the content of the covariant derivative of the different fields is determined by their individual transformation properties. The absence of mass terms in the Lagrangian is due to the peculiar nature of the weak force and leads to several complications. For one, the weak force is short ranged which indicate massive gauge bosons, but explicit mass terms for the gauge fields break gauge symmetry. In addition fermion mass terms also break gauge invariance, since these terms mix the left and right-handed chiral states which transforms differently under $SU(2)$. Of course one could contemplate simply throwing away gauge symmetry at this point, but it turns out that the resulting theory is non-renormalizable and violates unitarity[11]. The resolution to these problems in the Standard Model is to include a complex scalar field with a non-zero vacuum expectation value (vev), which couples to the gauge bosons and fermions. The appearance of a non-zero vev breaks electroweak symmetry leading to mass terms for the fermions and gauge bosons, in addition to a real scalar field, the Higgs field. This mechanism for introducing symmetry breaking terms is called spontaneous symmetry breaking, and it has been shown that gauge theories with spontaneous symmetry breaking are both renormalizable and unitary.

2.2 Electroweak Symmetry Breaking

Masses for the gauge boson and the fermions are dynamically generated by introducing a gauge invariant complex $SU(2)$ doublet scalar field H

$$H = \begin{pmatrix} H^+ \\ H^0 \end{pmatrix} \quad , \quad H' = e^{i\left(\frac{1}{2}\theta_y(x) + \theta^a(x)\tau_a\right)}H \tag{2.18}$$

where the weak hypercharge of the scalar is chosen to be $Y = \frac{1}{2}$. The dynamics of the scalar field is governed by the Lagrangian

$$\mathcal{L}_H = (\nabla^\mu H)^\dagger(\nabla_\mu H) - V(H^\dagger H) \tag{2.19}$$

$$V(H^\dagger H) = -\mu^2 H^\dagger H + \lambda\left(H^\dagger H\right)^2 \tag{2.20}$$

The important feature with regards to dynamical symmetry breaking is that, while the Lagrangian is invariant under the SM gauge group, the vacuum state is not, leading to a non-zero vacuum expectation value (vev) for the scalar as illustrated in fig. 2.2. To first approximation the vev, $\langle H \rangle$, is given by the minimum of the classical potential, which for eq. (2.20) results in

$$\langle H \rangle \approx \sqrt{\frac{\mu^2}{2\lambda}} = \frac{v}{\sqrt{2}} \tag{2.21}$$

The specific choice of vacuum state by nature breaks the original $SU(2)_L \times U(1)_Y$ symmetry, but leaves a new $U(1)$ symmetry to be associated with the electromagnetic field.

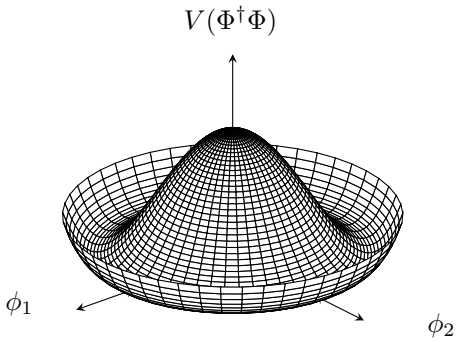

Figure 2.2: A qualitative plot of the Higgs potential $V(H^\dagger H)$ as a function of the components of the $SU(2)$ doublet H

We want this vacuum to be electrically neutral which can be achieved by choosing an SU(2) gauge so that H^+ vanishes, and a $U(1)$ gauge so that H^0 is real. This choice of gauge is called the unitary gauge, and allows us to write the field in terms of real fluctuations $h(x)$ around the vacuum expectation value v.

$$H = \frac{1}{\sqrt{2}} \begin{pmatrix} 0 \\ v + h(x) \end{pmatrix} \tag{2.22}$$

The real scalar field $h(x)$ is the famous Higgs field, whose associated quanta are the Higgs bosons. In terms of v and $h(x)$, eq. (2.20) becomes rather complicated, but can be split into three terms

$$\mathcal{L}_H = \mathcal{L}_{Higgs} + \mathcal{L}_{M_G} + \mathcal{L}_{int} \tag{2.23}$$

$\mathcal{L}_{int}$ contains cubic and quartic interaction terms between the Higgs boson and the gauge fields, while $\mathcal{L}_{Higgs}$ describes the dynamics of the free Higgs field

$$\mathcal{L}_{Higgs} = \partial_\mu h \partial^\mu h - \frac{1}{2} m_h^2 h^2 - \sqrt{\frac{\lambda}{2}} m_h h^3 - \frac{1}{4}\lambda h^4 \quad , \quad m_h = \sqrt{2}\mu \tag{2.24}$$

which in addition to the mass term, m_h^2, also contains cubic and quartic self-couplings. The last term, $\mathcal{L}_{M_G}$, contains the mass terms for the gauge bosons, which by denoting $V_\mu^a = (B_\mu, W_\mu^0)$, can be written in the form

$$\mathcal{L}_{M_G} = \frac{1}{2} m_W^2 \left[W_\mu^{+\dagger} W^{+\mu} + W_\mu^{-\dagger} W^{-\mu} \right] + \frac{1}{2} M_{ab}^2 V^{a\mu} V_\mu^b \tag{2.25}$$

$$m_W = \frac{gv}{2} \quad , \quad \left(M_{ab}^2 \right) = \frac{v^2}{4} \begin{pmatrix} g'^2 & -gg' \\ -gg' & g^2 \end{pmatrix} \tag{2.26}$$

Diagonalizing the mass matrix M_{ab} results in one massless eigenstate, which corresponds to the electromagnetic field A^μ, and a massive one, Z^μ, which is responsible for weak scattering processes such as the scattering of electrons and neutrinos. The states is usually written in terms of the Weinberg angels θ_W

$$\cos\theta_W = \frac{g}{\sqrt{g^2 + g'^2}} \quad , \quad \sin\theta_W = \frac{g'}{\sqrt{g^2 + g'^2}} \tag{2.27}$$

which allows us to write the neutral electroweak mass eigenstates as a standard rotation of the original gauge fields B_μ and W_μ^0

$$A_\mu = \sin\theta_W W_\mu^0 + \cos\theta_W B_\mu \quad , \quad m_A = 0 \tag{2.28}$$

$$Z_\mu = \cos\theta_W W_\mu^0 - \sin\theta_W B_\mu \quad , \quad m_Z = \frac{m_W}{\cos\theta_W} \tag{2.29}$$

In order to associate A_μ with the electromagnetic field we need to assign the correct hypercharges Y to the fermions. This is achieved by writing the neutral currents in terms the mass eigenstates A_μ, Z_μ

$$g' \cos\theta_W \left(T_3^i + Y^i \right) \overline{\Psi}_i \gamma^\mu A_\mu \Psi_i + \left(\cos^2\theta_W T_3^i - \sin^2\theta_W Y^i \right) \overline{\Psi}_i \gamma^\mu Z_\mu \Psi_i \tag{2.30}$$

where Ψ_i is a general left or right-handed field labelled by its $SU(2)$ charge, called the weak isospin T_3^i, and the weak hypercharge Y^i. Associating A_μ with the electromagnetic field gives the electric charge and coupling strength $q = eQ$ in terms of the electroweak ones

$$q = g' \cos_W\theta \left(T_3^i + Y^i \right) \quad , \quad e = g' \cos\theta_W \quad , \quad Q = \left(T_3^i + Y^i \right) \tag{2.31}$$

Through these relations the theory parameters can be determined from measurements of f.ex the electric charge and the masses of W and Z. From the measured values of masses and couplings at the weak scale one can infer the corresponding tree level value of the Higgs vev v. f.ex using the measured values for the mass of the Z boson, the elementary electric charge e, and the Weinberg angle at m_Z [76] gives

$$m_Z \approx 91.2\text{GeV} \quad , \quad \alpha_{em} = \frac{e^2}{4\pi} \approx \frac{1}{128} \quad , \quad \sin^2\theta_W = 0.231 \tag{2.32}$$

$$\rightarrow \qquad v(m_Z) = \frac{m_Z \sin(2\theta_W)}{2\sqrt{\pi\alpha_{em}}} \approx 246 \text{ GeV} \tag{2.33}$$

The relation between the weak isospino and hypercharge T_3, Y and the electric charge Q is known as the Gell-Mann-Nishijima relation. Table 2.1 lists the charge assignments required to give the correct electric charge in the Standard Model. The right-handed neutrino has $Q = Y = T_3 = 0$ and decouples completely from the electroweak forces. For this reason they are usually omitted from the standard model, although observed neutrino oscillations indicate that they do exist in some form or another [58]. Another thing to note is that the sum over fermion hypercharges vanish, which ensures the cancellations of certain anomalies in the standard model and will force the introduction of at least one new Higgs doublet in it's supersymmetric extensions.

Fermions	$\boldsymbol{\nu_e}$		$\boldsymbol{e}$		$\boldsymbol{u}$		$\boldsymbol{d}$	
Chirality	L	R	L	R	L	R	L	R
Electric Q	0	0	-1	-1	$+\frac{2}{3}$	$+\frac{2}{3}$	$-\frac{1}{3}$	$-\frac{1}{3}$
Isospin T_3	$+\frac{1}{2}$	0	$-\frac{1}{2}$	0	$+\frac{1}{2}$	0	$-\frac{1}{2}$	0
Hypercharge Y	$-\frac{1}{2}$	0	$-\frac{1}{2}$	-1	$+\frac{1}{6}$	$+\frac{2}{3}$	$+\frac{1}{6}$	$-\frac{1}{3}$

Table 2.1: Charge assignment for the first generation of the Standard Model. The other families are identical copies in terms of the electroweak quantum numbers

Masses for the fermions can also be generated through gauge invariant couplings to the scalar field known as Yukawa terms. The most general mass terms that can be added are[3]

$$\mathcal{L}_Y = -\left(\lambda_e^{ij}\overline{L}_i H e_{Rj} + \lambda_u^{ij}\overline{Q}_i H u_{Rj} + \lambda_d^{ij}\overline{Q}_i H_C d_{Rj} + h.c\right) \quad , \quad H_C = i\boldsymbol{\sigma}_2 H^{\dagger T} \tag{2.34}$$

where $h.c$ denotes the Hermitian conjugate. The new terms are invariant both under $SU(2)$, since L, Q, H and H_C transforms identically under $SU(2)$, while in the $U(1)$ case the transformation of H and H_C cancel the difference between left-handed and right-handed fields. After symmetry breaking the Yukawa couplings give rise to mass terms in addition to a coupling to the Higgs field proportional to the mass.

$$\mathcal{L}_Y = -(1 + \frac{H}{v})\left(m_{ij}^e \overline{e}_L^i e_R^j + m_{ij}^u \overline{u}_L^i u_R^j + m_{ij}^d \overline{d}_L^i d_R^j + h.c\right) \quad , \quad m_{ij} = \frac{\lambda_{ij} v}{\sqrt{2}} \tag{2.35}$$

The procedure for adding masses to the fermions is more ad hoc than in the case of the gauge bosons, and all the fermion couplings must be set by hand through the Yukawa couplings. However, the additional Higgs couplings appearing when generating masses in this way resolves the problems associated with the pure mass terms [11]. The mass matrices m_{ij} can in general be non-diagonal and complex without spoiling either gauge invariance or renormalizability [81], and can be diagonalized by introducing different mass eigenstates

[3] neglecting the right-handed neutrinos

for the left-handed and right-handed fields. This leads to family mixing in the quark sector, where the amount of mixing is parametrized by the Cabbibo-Kobayashi-Maskawa (CKM) matrix.

2.3 Problems with The Standard Model

Though the Standard Model has been tremendously successful in explaining experimental data and predicting novel phenomena, the Standard Model is far from the last word. First and foremost the Standard Model does not include gravity, and finding a consistent way of including gravity in a fundamental quantum description of nature remains one of the biggest challenges in modern physics. Solving this problem seems to require more radical modifications to the underlying framework than modifying the Standard Model Lagrangian. In addition there are several issues which can be addressed by extending upon the Standard Model symmetry group and field content:

- **Fine tuning problem**

  This problem refers to the apparent fine tuning needed to get the observed low energy Higgs mass parameter in eq. (2.20), $m_h^2 \sim (100\text{GeV})^2$. If we consider the Standard Model is valid up to some scale Λ the low energy effective parameter will receive loop corrections as compared to the bare parameter m_{h0}^2 at the cut off scale, see fig. 2.3.

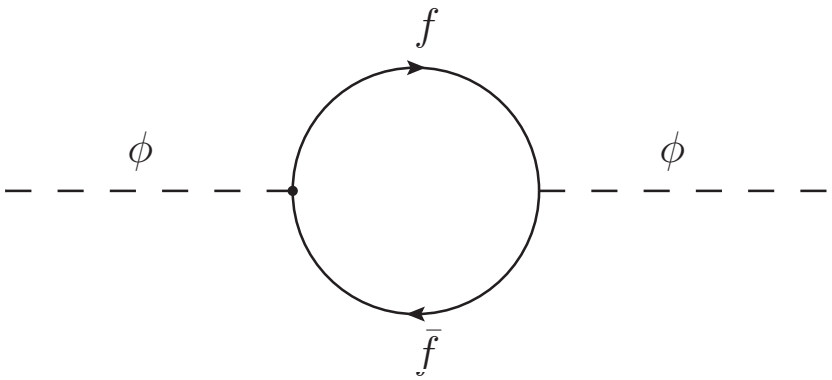

Figure 2.3: quadratic SM correction to the Higgs mass parameter m_h^2 from fermion loops

  This is not a unique feature of the Higgs mass, however unlike the other SM mass parameters the corrections are quadratic rather than logarithmic

$$m_h^2 = m_{h0}^2 + \delta m_h^2(\Lambda) \quad , \quad \delta m_h^2(\Lambda) \propto \Lambda^2 \tag{2.36}$$

  This means that if Λ is considerably larger then 100GeV, a fine tuning of the bare parameter is necessary to account for the smallness of the effective parameter. The appearance of quadratic rather than logarithmic corrections can be traced back to

the principle of technical naturalness due to t'Hooft [85], which states that a mass parameter m^2 is naturally small when a symmetry is restored in the limit $m \to 0$. This symmetry ensures that perturbative corrections to the parameter vanish when $m \to 0$, which is not the case for quadratic divergences and the allowed corrections are at most logarithmic $\delta m^2 \propto m^2 \ln(\Lambda^2/m^2)$. The masses of the SM fermions are protected by chiral symmetry and gauge bosons by gauge symmetry, but no such symmetry is restored by setting $m_h^2 = 0$ hence the appearance of quadratic divergences One way out of this problem is to postulate that the theory breaks down close to the electroweak scale thereby rendering Λ small. This is the idea behind technicolor, where the scalar field is a composite of techniquarks interacting through a new strong force to form a condensate, analogous to the pion in QCD. Although very attractive from a theoretical point of view, since the mechanism already has precedence in known physics, this approach is hard to reconcile with electroweak precision measurements and also typically gives rise to flavour changing neutral currents [80]. Another approach is to somehow extend the technical naturalness argument to the scalar, and this is how low energy supersymmetry provides a solution to the problem. By introducing a new symmetry relating scalars to fermions, the chiral symmetry protecting the fermion also protects the scalar [45].

- **Dark Matter and Dark Energy**

  Although the Standard Model is extremely successful in explaining data from high energy experiments, the model does not compare well with observations on cosmological scales. If one assumes that the gravitational physics is correctly described by general relativity on large scales (galactic scales and beyond) one is led to the conclusion that only 5% of the energy density of the universe can be given a satisfactory explanation within the Standard Model. The remaining energy density seems to be in the form of some pressureless (weakly interacting) fluid, suitably named dark matter, comprising roughly 25% of the total energy density, and a negative pressure component, called dark energy, making up the remaining 70%, see fig. 2.4.

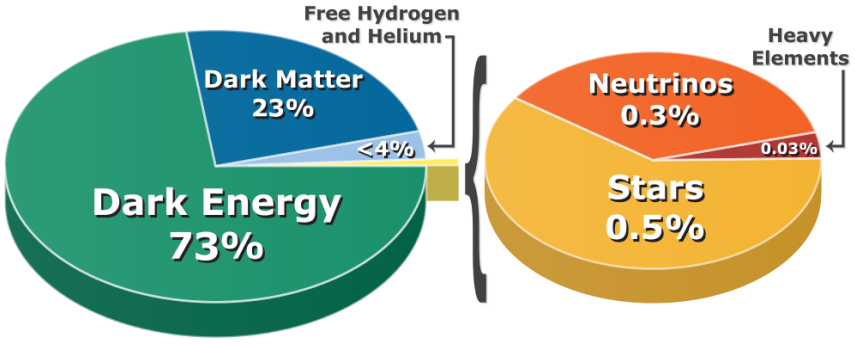

Figure 2.4: Composition of our universe as inferred from cosmological data, taken from [60]

The Standard Model does predict some dark matter, mainly in the form of neutrinos

and dark macroscopic objects such as black holes and brown dwarfs, but estimated abundance is not nearly enough to account for everything. Assuming the discrepancy is not due to incorrect gravitational physics the simplest explanation is the existence of at least one new type of weakly interacting particle, collectively referred to as WIMPs. In supersymmetric extensions of the Standard Model, the lightest supersymmetric particle (LSP) provides a good candidate since it naturally is both electrically neutral and sufficiently abundant to account for the observed energy density. When it comes to dark energy, the Standard Models does predict a negative pressure component to the total energy density, in the form of vacuum energy, however naive order of magnitude predictions give an energy density roughly 120 orders of magnitude too large. Supersymmetry does not provide any satisfactory solution to this problem, albeit it greatly improves upon the discrepancy, reducing it to 57 orders of magnitude [25].

In the following section we will briefly go over the main features of low energy supersymmetry and in particular the Minimal Supersymmetric Standard Model (MSSM).

Chapter 3

Supersymmetry

This chapter is mainly based on This chapter is mainly based on [73], [80],[49] and [18].

As mentioned at the end of last chapter, many of the problems facing the Standard Model can be alleviated by extending the symmetry group of the Standard Model. In particular the fine tuning problem has been a major driving force in the construction of Beyond the Standard Model (BSM) extensions. One way of resolving the issue is by introducing a new symmetry relating scalars to fermions, and ny doing so extending the stabilizing effects of the chiral symmetry to the scalar sector. We thus want to consider a symmetry of the form

$$\delta\phi = \epsilon\psi \quad , \quad \delta\phi^\dagger = \epsilon^\dagger\psi^\dagger \tag{3.1}$$

where ψ is a two-component Weyl fermion, and ϵ an infinitesimal two component spinor parametrizing the transformation. Such a transformation can be written in terms of four fermionic generators, which are commonly written in terms of a Weyl spinor Q and it's conjugate $Q^\dagger$. These fermionic generators obey anticommutation relations which through its Lorentz structure should be proportional to a Lorentz vector. It turns out that this has to be the generators of translation, P_μ, because introducing additional generators carrying Lorentz indices would constrain the theory to such an extent as to allow for no scattering at all [80]. Thus the anticommutator of the generators $Q, Q^\dagger$ takes the form

$$\left\{Q_\alpha, Q^\dagger_{\dot\beta}\right\} = -2\sigma^\mu_{\alpha\dot\beta}P_\mu, \tag{3.2}$$

where the numerical constant is purely conventional. Unlike the internal symmetry group of the Standard Model, these transformations mix with ordinary translations [1], and supersymmetry can therefore be seen as an extension of the spacetime symmetry group. This indicates that the new transformations should apply to everything not just the Higgs scalar as originally intended, and supersymmetry therefore predicts that each fermion has a bosonic superpartner and vice versa. In supersymmetric extensions of the Standard Model, these new superpartners give rise to new loop corrections to the Higgs mass, which cancel

[1] And also with rotations and boosts, as can be seen by looking at the full set of commutator relations for the Super-Poincare algebra

the quadratic divergences discussed in chapter 2. The diagram cancelling the quadratic divergences from fig. 2.3 is shown in fig. 3.1.

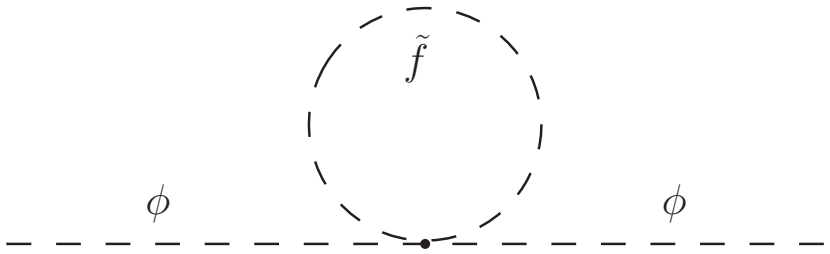

Figure 3.1: sfermion loop correction to the Higgs mass parameter μ^2 to cancels fermion loop in fig. 2.3

In the minimal extension of the Standard Model, called the MSSM, each fermion is paired up with a spin 0 particle called a sfermion, the top t with the stop $\tilde{t}$, the bottom b with the sbottom $\tilde{b}$, and so on. Furthermore each gauge boson is paired up with a spin 1/2 gaugino, the B's with binos $\tilde{B}$, the W's with Wino's $\tilde{W}$ and so on. In order for the MSSM to be anomaly free, it is not possible to generate the up-type and down-type fermion masses using the same Higgs field and the Higgs sector must be extended to a two Higgs doublet with corresponding spin 1/2 superpartners called Higgsinos. The Higgsinos mix with the Winos and the Binos to form 4 neutral neutralinos $\chi^0_{1,2,3,4}$ and two charged charginos $\chi^{\pm}_{1,2}$.

The relation between supersymmetry and spacetime generators indicate that supersymmetric field theories are most naturally represented by extending spacetime into what is called superspace. This is done by introducing a set of new fermionic coordinates and constructing coordinate representations of the SUSY algebra. In this way the particles and their superpartners fit nicely into representations of the superspace symmetries, called supermultiplets, in a similar manner as ordinary particles correspond to representations of the Minkowski spacetime symmetries. Introducing superspace requires a lot of new formalism which is not in any way needed for the work done in this thesis and as such, we simply state the results without proof and refer the reader to [73] for a proper construction of the theory. For supersymmetric extensions of the standard model we need two different supermultiplets. The matter and Higgs fields, are grouped together with their respective superpartners into what are called chiral supermultiplets Φ

$$\Phi = (\psi, \phi, F) \tag{3.3}$$

where ψ denotes a two-component Weyl fermion and ϕ a complex scalar. The field F contained in the supermultiplet is an auxiliary complex scalar field, needed in order to match the number of fermionic and bosonic degrees of freedom off shell. On shell these fields will be algebraically related to ϕ. The transformation properties of a supermultiplet

S can be inferred from the SUSY algebra eq. (3.2), by considering infinitesimal SUSY transformation parametrized by the two component spinor ϵ

$$\delta S = -i\left(\epsilon Q + \epsilon^\dagger Q^\dagger\right) S \tag{3.4}$$

For the chiral supermultiplet Φ, this leads to the following transformations of the component fields

$$\delta\phi = \sqrt{2}\epsilon\psi \tag{3.5}$$
$$\delta\psi_\alpha = \sqrt{2}\left(\epsilon_\alpha F - i\epsilon^{\dagger\dot{\beta}}\sigma^\mu_{\alpha\dot{\beta}}\partial_\mu\phi\right) \tag{3.6}$$
$$\delta F = -\sqrt{2}\epsilon^\dagger\bar{\sigma}^\mu\partial_\mu\psi \tag{3.7}$$

where we see the fermion ψ and the scalar ϕ being related as desired, eq. (3.1). The gauge fields A_μ and their fermionic superpartners λ belong to a different representation of the SUSY algebra, called vector supermultiplets V

$$V = (A^\mu, \lambda, D) \tag{3.8}$$

where D is an auxilliary real scalar needed for consistency off shell. For the vector supermultiplet, the components transform as

$$\delta A_\mu = -\frac{1}{2}\left(\epsilon^\dagger\bar{\sigma}_\mu\lambda - \lambda^\dagger\bar{\sigma}_\mu\epsilon\right) \tag{3.9}$$
$$\delta\lambda_\alpha = \frac{1}{\sqrt{2}}\left(\epsilon_\alpha D + \frac{i}{2}\epsilon_\beta\sigma^\mu_{\alpha\dot{\alpha}}\bar{\sigma}^{\nu\dot{\alpha}\beta}F_{\mu\nu}\right) \tag{3.10}$$
$$\delta D = -i\left(\epsilon\sigma^\mu\partial_\mu\lambda^\dagger + \partial_\mu\lambda^\dagger\bar{\sigma}^\mu\epsilon\right) \tag{3.11}$$

Using these ingredients we can now construct a supersymmetric gauge theory based on the standard model gauge group. The resulting Lagrangian takes the form

$$\mathcal{L}_{SUSY} = \psi_i^\dagger\bar{\sigma}^\mu\nabla_\mu\psi_i + \nabla_\mu\phi_i^\dagger\nabla^\mu\phi_i - \frac{1}{4}F_a^{\mu\nu}F^a_{\mu\nu} + i\lambda_a^\dagger\bar{\sigma}^\mu\nabla_\mu\lambda_a \tag{3.12}$$
$$-\frac{1}{2}\left(\frac{\partial W}{\partial\phi_i\partial\phi_j}\psi_i\psi_j + c.c\right) - g(\phi_i^\dagger\boldsymbol{\lambda}\psi_i - \psi_i^\dagger\boldsymbol{\lambda}\phi_i) \tag{3.13}$$
$$-\left(F_i^\dagger F^i + \frac{1}{2}D_a^2\right) \tag{3.14}$$

where ∇_μ are the $SU(3)_C \times SU(2)_L \times U(1)_Y$ gauge covariant derivatives, and $F^a_{\mu\nu}$ denote the field strength tensors for the gauge fields. W is called the superpotential and contains the potential terms for the chiral supermultiplets. The auxiliary fields F and D are, as already mentioned, related to the scalar fields ϕ_i through algebraic equations of motion

$$F_i^\dagger = -\frac{\partial W}{\partial \phi^i} \quad , \quad D_a = -g\phi^\dagger \boldsymbol{\tau}_a \phi \tag{3.15}$$

The Lagrangian, eqs. (3.12) to (3.14), is the supersymmetric equivalent of the Yang-Mills Lagrangian of section 2.1, but with the scalars necessary for electroweak symmetry breaking appearing naturally. The first line of the action contains the usual matter and gauge kinetic terms with the corresponding terms for the sfermions and gauginos. The second line contains terms coupling the fermions, scalars and gauginos, in addition to mass terms for the fermions and gauginos if one of the scalars acquires a non-zero vev. Finally the last line is the scalar potential written in terms of the auxiliary fields. In the Minimal Supersymmetric Standard Model, which we turn to next, this term will contain the Higgs potential responsible for electroweak symmetry breaking.

3.1 Minimal Supersymmetric Standard Model

The Minimal Supersymmetric Standard Model (MSSM) can now be constructed by associating each left and right handed fermion of the Standard Model with a chiral supermultiplet and the gauge bosons with vector supermultiplets with the same charge assignment as in the SM. This results in a theory which reproduces the gauge couplings of the standard model, but with analogous couplings of equal strength involving the superpartners, see fig. 3.2.

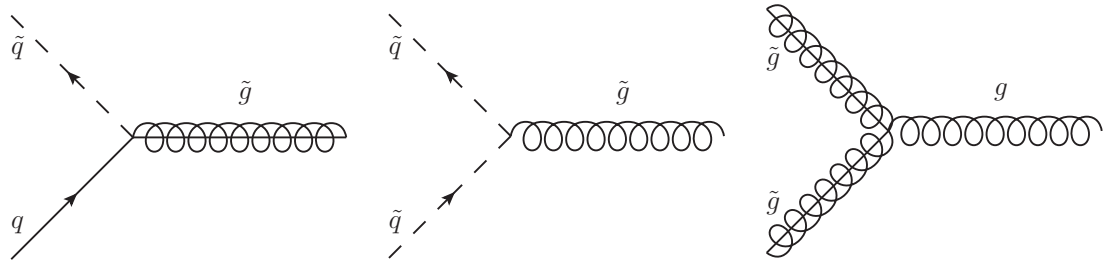

Figure 3.2: Examples of additional strong gauge couplings between quarks q, squarks $\tilde{q}$, gluons g and gluinos $\tilde{g}$ in the MSSM [50]

The only extension needed compared to the SM is the addition of a second Higgs doublet in order to give mass to both up type and down type quarks. In the standard model one Higgs doublet was sufficient because the charge conjugate of the Higgs scalar can be used to generate masses for the down type quarks eq. (2.34). This is not possible in the supersymmetrized version for multiple reasons. One reason is that the superpotential has to be a polynomial in left chiral supermultiplets only, which inhibits the use of the charge conjugate. In addition the extra fermion due to a single Higgs chiral supermultiplet gives rise to a gauge anomaly [73] which needs to be cancelled by an additional fermion with opposite hypercharge. In the MSSM this is done by having a second Higgs supermultiplet

Names		spin 0	spin 1/2	$SU(3)_C$, $SU(2)_L$, $U(1)_Y$
squarks, quarks	$\mathcal{Q}$	$(\tilde{u}_L \;\; \tilde{d}_L)$	$(u_L \;\; d_L)$	$(\mathbf{3}, \mathbf{2}, +\frac{1}{6})$
(×3 families)	$\mathcal{U}$	$\tilde{u}_R^\dagger$	$u_R^\dagger$	$(\overline{\mathbf{3}}, \mathbf{1}, -\frac{2}{3})$
	$\mathcal{D}$	$\tilde{d}_R^\dagger$	$d_R^\dagger$	$(\overline{\mathbf{3}}, \mathbf{1}, +\frac{1}{3})$
sleptons, leptons	$\mathcal{L}$	$(\tilde{\nu} \;\; \tilde{e}_L)$	$(\nu \;\; e_L)$	$(\mathbf{1}, \mathbf{2}, -\frac{1}{2})$
(×3 families)	$\mathcal{E}$	$\tilde{e}_R^\dagger$	$e_R^\dagger$	$(\mathbf{1}, \mathbf{1}, +1)$
Higgs, Higgsinos	$\mathcal{H}_u$	$(H_u^+ \;\; H_u^0)$	$(\tilde{H}_u^+ \;\; \tilde{H}_u^0)$	$(\mathbf{1}, \mathbf{2}, +\frac{1}{2})$
	$\mathcal{H}_d$	$(H_d^0 \;\; H_d^-)$	$(\tilde{H}_d^0 \;\; \tilde{H}_d^-)$	$(\mathbf{1}, \mathbf{2}, -\frac{1}{2})$

Table 3.1: Chiral supermultiplets in the Minimal Supersymmetric Standard Model. The spin-0 fields are complex scalars, and the spin-1/2 fields are left-handed two-component Weyl fermions.

Names	spin 1/2	spin 1	$SU(3)_C$, $SU(2)_L$, $U(1)_Y$
gluino, gluon	$\tilde{g}$	g	$(\mathbf{8}, \mathbf{1}, 0)$
winos, W bosons	$\tilde{W}^\pm \;\; \tilde{W}^0$	$W^\pm \;\; W^0$	$(\mathbf{1}, \mathbf{3}, 0)$
bino, B boson	$\tilde{B}^0$	B^0	$(\mathbf{1}, \mathbf{1}, 0)$

Table 3.2: Gauge supermultiplets in the Minimal Supersymmetric Standard Model.

$\mathcal{H}_d$ responsible for generating masses for the down type quark, in addition to the ordinary Higgs field denoted $\mathcal{H}_u$. The naming conventions for the multiplets of the MSSM closely follow those of [73], see tables table 3.1 and table 3.2.

This notation is similar to that used for the Standard Model, with the exception that all fermions are written in terms of two component Weyl spinors rather than the 4-dimensional Dirac spinors. For example, the right handed Dirac electron e, appearing in equation 2.17, can be written in terms of a right handed Weyl e_R

$$e = \begin{pmatrix} 0 \\ e_R \end{pmatrix} \quad , \quad \bar{e}\gamma^\mu \partial_\mu e = e_R \bar{\sigma}^\mu \partial_\mu e_R^\dagger \tag{3.16}$$

The left chiral superfield $\mathcal{E}$ describing the right handed electron should thus contain the left handed fermion $e_R^\dagger$ and its scalar partner which by convention is written $\tilde{e}_R^\dagger$. With the particle content and gauge charges specified, the only thing remaining is the MSSM superpotential W_{MSSM}. The most general renormalizable superpotential consistent with the SM symmetries is [18]

$$W_{MSSM} = \lambda_u^{ij}\mathcal{Q}_i\mathcal{H}_u\mathcal{U}_j - \lambda_d^{ij}\mathcal{Q}_i\mathcal{H}_d\mathcal{D}_j - \lambda_e^{ij}\mathcal{L}_i\mathcal{H}_d\mathcal{E}_j + \mu\mathcal{H}_u\mathcal{H}_d \tag{3.17}$$

$$+ \lambda_{ijk}\mathcal{L}_i\mathcal{L}_j\mathcal{E}_k + \lambda'_{ijk}\mathcal{L}_i\mathcal{Q}_j\mathcal{D}_k + \lambda''_{ijk}\mathcal{U}_i\mathcal{D}_j\mathcal{D}_k + \kappa_i\mathcal{L}_i\mathcal{H}_u \tag{3.18}$$

where the scalar products of the $SU(2)$ doublets are antisymmetric, $\mathcal{Q}\mathcal{H} = \epsilon_{ab}\mathcal{Q}^a\mathcal{H}^b$, and i and j run over the three families. The terms in the second line of eq. (3.18) break either baryon or lepton number and can be removed by imposing a new discrete symmetry called R-parity. Under this symmetry Standard model fields are even and superpartners odd, which implies that sparticles must be pair produced and that the lightest supersymmetric particle (LSP) is stable. If the LSP is also weakly interacting it provides a suitable dark matter candidate.

Of the remaining terms, the first three give rise to the usual Higgs-fermion couplings in addition to couplings between Higgsinos, sfermions and fermions. Here y_{ij} are the same Yukawa couplings given in eq. (2.34). The μ-term in the superpotential gives rise to Higgs mass terms in the Lagrangian, which together with quartic Higgs terms coming from the D^2-term can accommodate electroweak symmetry breaking in a manner similar to that discussed in chapter 2. However the corresponding masses for the superpartners will be identical, a generic feature of supersymmetry which follows from the fact that the supersymmetry generators Q and $Q^\dagger$ commute with the generators of spacetime translations and by extension the mass operator $P^\mu P_\mu$. Furthermore the superpartners also couple with the same strength as the standard model particles making them easy to produce with today's particle accelerators, so if supersymmetry is realized in nature it must be broken at low energy. In order to keep the desired stabilizing feature of supersymmetry, the resulting SUSY breaking terms should not reintroduce the quadratic divergences we set out to remove. This is usually referred to as soft SUSY breaking.

3.1.1 Supersymmetry Breaking in the MSSM

SUSY can be broken softly by having a vacuum state that breaks the symmetry in a manner analogous to electroweak symmetry breaking in the Standard Model. The condition needed for this to occur can be inferred from the anticommutator eq. (3.2) by taking the trace

$$\frac{1}{4}\sum_\alpha \left\{Q_\alpha, Q^\dagger_{\dot\alpha}\right\} = P_0 = H \tag{3.19}$$

If SUSY is broken by the vacuum, then $Q\left|0\right\rangle \neq 0, Q^\dagger\left|0\right\rangle \neq 0$, which through eq. (3.19) requires a non-zero vacuum energy $\left\langle 0\right| H \left|0\right\rangle > 0$. As we would like to keep Lorentz invariance intact, this should occur in the scalar part of the potential, given by eq. (3.14). This means that in order to break SUSY we need either

$$\langle F\rangle \neq 0 \quad , \quad \langle D\rangle \neq 0 \tag{3.20}$$

This is referred to F-type and D-type SUSY breaking, where D-term breaking requires adding a linear D-term associated with an Abelian gauge symmetry [73].

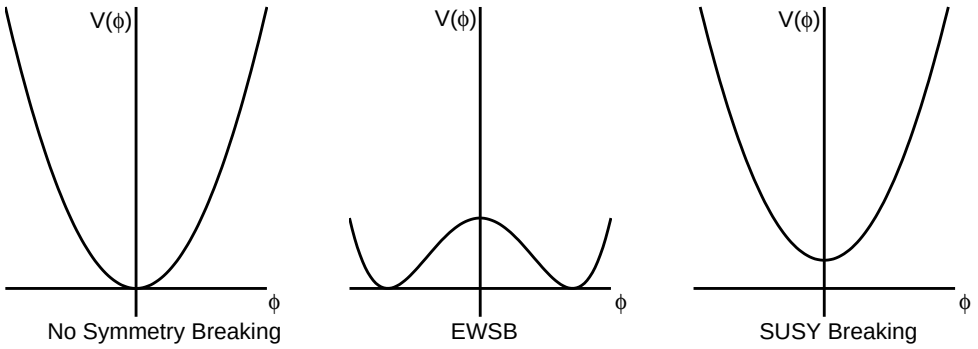

Figure 3.3: Different potential shapes and their associated symmetry breaking

As can be seen from the transformation properties of the supermultiplets, eq. (3.6) and (3.10), the vacuum state of the fermionic component is no longer invariant under SUSY when the associated auxiliary field (F, D) acquires a vev, and results in additional fermionic degrees of freedom called Goldstinos. These play a similar role in spontaneous SUSY breaking as the Goldstone bosons in EWSB. When SUSY is gauged, these are "eaten" by the superpartner of the graviton, called the gravitino.

It turns out that breaking SUSY using the F or D-terms associated with the Standard Model fields is problematic and leads to scenarios which typically predict sfermions or sleptons lighter than their SM partners. In order to generate viable SUSY breaking terms, it therefore seems necessary to extend the theory by introducing a hidden sector where SUSY breaking can occur, see fig. 3.4. This sector is connected to the MSSM part through what are called messenger fields which mediate SUSY breaking to the visible part of the theory.

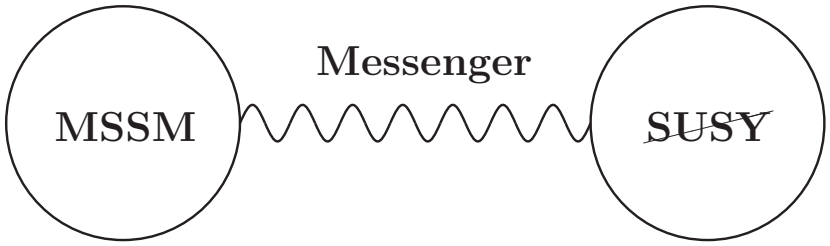

Figure 3.4: Qualitative diagram of the assumed SUSY breaking in the MSSM

In accordance with t'Hooft's naturalness argument these terms should carry positive mass dimension so that the associated divergences are logarithmic. The allowed terms consistent

with the SM gauge symmetries are mass terms for the gauginos, sfermions and the Higgs, in addition to trilinear sfermion Yukawa couplings.

$$\begin{aligned}\mathcal{L}_{soft} = &-\frac{1}{2}\left(M_3\tilde{g}\tilde{g} + M_2\tilde{W}\tilde{W} + M_1\tilde{B}\tilde{B} + c.c\right) \\ &- \left(a_{uij}\tilde{u}_i\tilde{Q}_j H_u - a_{dij}\tilde{d}_i\tilde{Q}_j H_d - a_{eij}\tilde{e}_i\tilde{L}_j H_d + c.c\right) \\ &- m^2_{Qij}\tilde{Q}^\dagger_i\tilde{Q}_j - m^2_{Lij}\tilde{L}^\dagger_i\tilde{L}_j - m^2_{uij}\tilde{u}_i\tilde{u}^\dagger_j - m^2_{dij}\tilde{d}_i\tilde{d}^\dagger_j - m^2_{eij}\tilde{e}_i\tilde{e}^\dagger_j \\ &- m^2_{H_u}H^\dagger_u H_u - m^2_{H_d}H^\dagger_d H_d - (bH_u H_d + c.c)\end{aligned} \tag{3.21}$$

$\mathcal{L}_{soft}$ contains more than 100 new parameters, but many of the new terms lead to additional contributions to flavour mixing and CP violation, which are heavily constrained by experiment. To avoid such unwanted contribution it is usual to assume that the sfermion mass matrices $\mathbf{m}$ are diagonal and the trilinear couplings $\mathbf{a}$ are proportional to the Yukawa couplings

$$\mathbf{m}^2_{Q,L,u,d,e} = m^2_{Q,L,u,d,e}\mathbb{1} \quad , \quad \mathbf{a}_{u,d,e} = A_{u,d,e}\mathbf{y}_{u,d,e} \quad , \quad \mathbf{y}_{u,d,e} \approx y^{33}_{u,d,e} \tag{3.22}$$

where the trilinear couplings $A_{u,d,e}$, in addition to the gaugino masses $M_{1,2,3}$ and μ, are assumed to be real. This ensures that the only CP violation comes from the usual Standard Model CKM matrix. Models imposing phenomenological constraints directly on the low energy Lagrangian, are usually referred to as phenomenological MSSM (pMSSM) models, where the constraints given in eq. (3.22) reduce the number of free parameters down to 24. In the pMSSM model considered in chapter 4 the masses of the first two generations of sfermions are also assumed to be degenerate, reducing the number of parameters to 19.

3.1.2 the MSSM Mass Spectrum

Electroweak symmetry breaking in the MSSM proceed along the same lines as in the standard model, but is more complicated due to the existence of the additional Higgs field H_d

$$H_u = \begin{pmatrix} H^+_u \\ H^0_u \end{pmatrix} \quad , \quad H_d = \begin{pmatrix} H^0_d \\ H^-_d \end{pmatrix} \tag{3.23}$$

However the basic ingredients are the same; We want to have a Higgs potential V_H with a minima away from the origin so that the Higgs fields acquire non-zero vevs. As in the SM we want this vacuum to be uncharged, which from the hypercharge assignment in table 3.1 means we want

$$\langle H_u \rangle = \begin{pmatrix} 0 \\ v_u \end{pmatrix} \quad , \quad \langle H_d \rangle = \begin{pmatrix} v_d \\ 0 \end{pmatrix} \tag{3.24}$$

One of the charged components can be set to zero by a SU(2) transformation, and it can be shown that in order for the potential to have a minimum, the other charged component must also vanish in the vacuum, and the vevs v_u and v_d must have opposite phases. This means both can be made real simultaneously by a U(1) transformation. It is therefore sufficient to consider the neutral Higgs part of the MSSM scalar potential, given by eq. (3.14).

$$V_{H^0} = \left(|\mu|^2 + m_{H_u}^2\right)|H_u^0|^2 + \left(|\mu|^2 + m_{H_d}^2\right)|H_d^0|^2 - \left(bH_u^0 H_d^0 + c.c\right) + \frac{g^2 + g'^2}{8}\left(|H_u^0|^2 - |H_d^0|^2\right)^2 \tag{3.25}$$

Here the quadratic terms come from the F-term in the scalar potential and the quartic couplings from the D-term leading to an MSSM quartic coupling completely determined by the $U(1)$ and $SU(2)$ gauge couplings. For the potential to have a non-zero minimum given by

$$\frac{dV_{H^0}}{dH_u^0} = \frac{dV_{H^0}}{dH_d^0} = 0 \quad , \tag{3.26}$$

two additional requirements on the parameters are needed

$$b < |\mu|^2 + \frac{1}{2}\left(m_{H_u}^2 + m_{H_d}^2\right) \tag{3.27}$$

$$b^2 > \left(|\mu|^2 + m_{H_u}^2\right)\left(|\mu|^2 + m_{H_u}^2\right) \tag{3.28}$$

The first constraint is required for the potential to be bounded from below along the direction $H_u = H_d$, where the D-term vanishes, while the second one is needed to prevent a stable minimum at the origin. These relations are not satisfied if the SUSY breaking parameters vanish, which means that EWSB in the MSSM also requires SUSY-breaking [49]. As in the Standard Model, the vevs v_u and v_d give rise to mass terms for the gauge bosons through the scalar covariant derivative in eq. (3.12). This allows us to relate the MSSM vevs to the Z mass and electroweak gauge couplings in the same way as in the Standard Model, eq. (2.29)

$$v_u^2 + v_d^2 = v^2 = \frac{2m_Z^2}{g^2 + g'^2} \approx (174\text{GeV})^2 \quad , \tag{3.29}$$

and express v_u and v_d in terms of the SM vev v and their ratio

$$\tan\beta = \frac{v_u}{v_d} \quad , \quad v_u = v\sin\beta \quad , \quad v_d = v\cos\beta \tag{3.30}$$

Requiring EWSB in accordance with eq. (3.29) allows us to eliminate two of the five Higgs parameters in the MSSM through the equations

$$\mu^2 + m_{H_u}^2 - b\cot\beta - \frac{M_Z^2}{2}\cos(2\beta) = 0 \tag{3.31}$$

$$\mu^2 + m_{H_d}^2 - b\tan\beta - \frac{M_Z^2}{2}\cos(2\beta) = 0 \tag{3.32}$$

In the pMSSM scans discussed in chapter 4, these parameters are taken to be $\tan\beta$ and $|\mu|^2$, in addition to one of the additional Higgs mass eigenstates, m_{A0}, appearing as a consequence of the extra Higgs doublet.

Higgs Masses

In the Standard model three of the real degrees of freedom related to the complex doublet are 'eaten' by the W,Z bosons, leaving only one real Higgs scalar field h. In the MSSM there are five physical degrees of freedom after EWSB, and the five related mass eigenstates are two CP even neutral Higgs scalars, h_0, H_0, two charged scalars $H^\pm$ and the CP-odd neutral scalar A_0 with tree level masses given by

$$m_{A_0}^2 = 2\mu^2 + m_{H_u}^2 + m_{H_d}^2 \tag{3.33}$$

$$m_{h_0,H_0}^2 = \frac{1}{2}\left(m_{A0}^2 + m_Z^2 \pm \sqrt{(m_{A0}^2 - m_Z^2)^2 + 4m_Z^2 m_{A_0}^2 \sin^2(2\beta)}\right) \tag{3.34}$$

$$m_{H^\pm}^2 = m_{A_0}^2 + m_W^2 \tag{3.35}$$

Gaugino Masses

The Higgs fermionic superpartner, the Higgsinos, mixes with the electroweak gauginos through the second term in eq. (3.13), which couples the Higgses, the Higgsinos and the gauginos. This leads to off-diagonal terms in the mass matrix after EWSB, and gives rise to four neutral eigenstates, called neutralinos $\chi^0_{1,2,3,4}$, and four charged eigenstates called charginos $\chi^\pm_{1,2}$. The neutralino mass matrix in terms of the neutral gauge eigenstates $\tilde{\chi}^0 = (\tilde{B}, \tilde{W}^0, \tilde{H}_u^0, \tilde{H}_u^0)$ is given by

$$\mathbf{M}_{\chi^0} = \begin{pmatrix} M_1 & 0 & -\frac{g'v_d}{\sqrt{2}} & \frac{g'v_u}{\sqrt{2}} \\ 0 & M_2 & -\frac{gv_d}{\sqrt{2}} & -\frac{gv_d}{\sqrt{2}} \\ -\frac{g'v_d}{\sqrt{2}} & -\frac{gv_d}{\sqrt{2}} & 0 & -\mu \\ \frac{g'v_u}{\sqrt{2}} & -\frac{gv_u}{\sqrt{2}} & -\mu & 0 \end{pmatrix} \tag{3.36}$$

The diagonal M_1 and M_2 terms comes from the SUSY breaking gaugino mass terms, while the μ-term comes from the MSSM superpotential through the first term in eq. (3.13). The analytic expressions for the eigenvalues of the neutralino mass matrix are in general long

and complicated, however when the mixing terms are small, the four neutralino mass states will decouple into a bino like $\chi^0 \approx \tilde{B}$, a wino-like $\chi^0 \approx \tilde{W}$ and two Higgsino like mass eigenstates $\chi^0 \approx (\tilde{H}_u \pm \tilde{H}_d)/\sqrt{2}$, with masses approximately given by the mass parameters M_1, M_2 and $|\mu|$ in addition to small perturbative corrections

$$m_{\chi^0_{\tilde{B}}} \approx M_1 - \frac{m_Z^2}{\mu^2 - M_1^2} \quad , \quad m_{\chi^0_{\tilde{W}}} \approx M_2 - \frac{m_W^2}{\mu^2 - M_2^2} \tag{3.37}$$

$$m_{\chi^0_{\tilde{H}}} \approx |\mu| + \frac{m_Z^2(\text{sign}(\mu) \mp \sin 2\beta)(\mu \pm [M_1 \cos^2\theta_W + M_2 \sin^2\theta_W])}{2(\mu \pm M_1)(\mu \pm M_2)} \tag{3.38}$$

Which of these is the lightest depends on the specific model parameters. The chargino mass matrix on the other hand, mixes the four charged winos and Higgsinos, and in the basis $\tilde{\chi}^\pm = (\tilde{W}^+, \tilde{H}_u^+, \tilde{W}^-, \tilde{H}_u^-)$ it takes the form

$$\mathbf{M}_{\chi^\pm} = \begin{pmatrix} 0 & \mathbf{X}^T \\ \mathbf{X} & 0 \end{pmatrix} \quad , \quad \mathbf{X} = \begin{pmatrix} M_2 & g v_u \\ g v_d & \mu \end{pmatrix} \tag{3.39}$$

After diagonalization this leads to two physical mass eigenstates $m_{\chi_1^\pm}$ and $m_{\chi_2^\pm}$

$$\begin{aligned} m_{\chi^\pm_{1,2}} =& \frac{1}{2}\left(|M_2|^2 + |\mu|^2 + 2m_W^2\right) \\ & \pm \frac{1}{2}\sqrt{\left(|M_2|^2 + |\mu|^2 + 2m_W^2\right)^2 - 4\left|\mu M_2 - m_W^2 \sin 2\beta\right|^2} \end{aligned} \tag{3.40}$$

The only remaining gaugino is the gluino $\tilde{g}$, which is the superpartner of the gluon. Since the gluinos carry colour they cannot mix with any of the other MSSM particles and their masses are therefore simply given by the soft braking mass M_3 at the weak scale.

Sfermion Masses

The sfermions mixing in the MSSM is very complicated in general, receiving contributions from both the D-terms and the F-terms in the scalar potential in addition to receiving soft SUSY breaking contributions from both the explicit sfermion mass terms and the trilinear couplings. Without any constraints on the soft breaking terms any sfermion with the same charge, R-parity and colour can mix, giving three 6×6 mass matrices for the charged sfermions, $(\tilde{u}_{iL}, \tilde{u}_{iR}), (\tilde{d}_{iL}, \tilde{d}_{iR}), (\tilde{e}_{iL}, \tilde{e}_{iR})$, and a 3×3 matrix for the neutrinos ν_{Li}. However if one assumes the phenomenologically motivated simplifications given in eq. (3.22), family mixing can be neglected and the mass matrices decouple into independent 2×2 matrices one for each species

$$\mathbf{M}^2_{\tilde{f}} = \begin{pmatrix} m^2_{\tilde{f}_L} + m^2_f + \Delta_{\tilde{f}_L} & v\left(a^*_f \cos\beta - \mu y_f \sin\beta\right) \\ v\left(a_f \cos\beta - \mu y_f \sin\beta\right) & m^2_{\tilde{f}_R} + m^2_f + \Delta_{\tilde{f}_R} \end{pmatrix} \tag{3.41}$$

$$\Delta_{\tilde{f}} = \frac{1}{2}\left(T^{\tilde{f}}_3 g^2 - Y^{\tilde{f}} g'^2\right)\left(v_d^2 - v_u^2\right) \tag{3.42}$$

Due to the smallness of the Yukawa couplings for the first two generations, the off-diagonal terms can be neglected. This is not the case for the third generation superpartners where the mixing can be significant and leads to mixed mass eigenstates $\tilde{f}_1, \tilde{f}_2$. This mixing is most significant for the stops due to its large Yukawa coupling, but if $\tan\beta$ is sufficiently large then the mixing of sbottom and stau can also be important. The large mixing in the stop mass matrix leads to a large mass between the two mass eigenstates and for this reason the lightest stop is often the lightest squark.

3.1.3 SUSY Breaking Scenarios

The large number of SUSY breaking parameters in the MSSM, even after imposing phenomenological constraints, make the theory difficult to probe both experimentally and theoretically. It is therefore common to look at specific SUSY breaking scenarios where the low energy SUSY breaking parameters can be related to a much smaller set of input parameter at higher energy. If the mediation of SUSY breaking to the MSSM sector is flavour blind then the resulting SUSY breaking terms obey conditions similar to those presented when considering the pMSSM. One such scenario is that of gauge mediated supersymmetry breaking (GMSB), where the SUSY breaking in the hidden sector is transmitted via messenger fields which couple to the MSSM sector of the theory indirectly through gauge interactions. Another popular idea is that SUSY breaking is mediated by gravitational interactions, and the constrained MSSM (cMSSM) falls into this category. As the cMSSM parameter space was the focus of paper I, we will briefly review this model, where we follow the treatment in [76] closely

The cMSSM

In the cMSSM, the underlying high energy theory is supergravity, which results from gauging supersymmetry. Gravity provides a natural mechanism for mediating SUSY breaking effects since the coupling is universal and extremely small, e.g suppressed by inverse powers of the Planck mass M_{Pl}. In the minimal supergravity (mSUGRA) framework the resulting SUSY breaking terms take a particularly simple form at some high energy (X), where the gaugino masses , scalar masses and the trilinear couplings become universal

$$M_{1,2,3}(X) = m_{1/2} \quad , \quad \mathbf{m}^2_{Q,L,u,d,e}(X) = m_0^2 \mathbb{1} \quad , \quad \mathbf{a}_{u,d,e}(X) = A_0 \mathbf{y}_{u,d,e} \tag{3.43}$$

These parameters are related to the SUSY breaking terms at the weak scale through the renormalization group equations (RGE), see fig. 3.5, and in the case of the gauginos, the RGE flow leads to a simple relations between the universal mass $m_{1/2}$ and the weak scale masses $M_{1,2,3}(Z)$

$$M_3(M_Z) = \frac{g_s}{g} M_2(M_Z) \approx 3.5 M_2(M_Z) \tag{3.44}$$

$$M_1(M_Z) = \frac{5g'^2}{3g^2} M_2(M_Z) \approx 0.5 M_2(M_Z) \tag{3.45}$$

This again simplifies the parameter dependence of the neutralino mass matrix, eq. (3.36), which only depends on the gluino mass $m_{\tilde{g}}$, the Higgs mass parameter μ and the ratio of the Higgs vevs $\tan\beta$. The weak scale squark masses depend primarily on the universal scalar and gaugino masses m_0 and $m_{1/2}$, and the universality at high energy also ensures no additional flavour mixing or CP violation from the SUSY breaking terms. The universality conditions given above reduces the number of input parameters to five: the universal masses $m_{1/2}$ and m_0, the trilinear coupling A_0, and the Higgs mass parameters μ and b_0. The latter two can be related to the measured Z mass m_Z and $\tan\beta$, which allows us to remove μ and b_0 in favour of $\tan\beta$ and the sign of mu, leaving only four parameters and a sign

$$m_0 \ , \ m_{1/2} \ , \ A_0 \ , \ \tan\beta \ , \ \mathrm{sign}(\mu) \tag{3.46}$$

The superpartner of the graviton, the gravitino $\tilde{G}$, is also a free parameter, but due to the extremely small coupling, the gravitino does not affect the RGE evolution of the MSSM parameters. The model defined by eq. (3.46) is what is usually called the cMSSM and is sometimes distinguished from mSUGRA models where additional relations between the parameters might exist. A typical weak scale mass spectrum resulting from cMSSM is shown in fig. 3.5

Typically the cMSSM has a neutralino LSP, which with its weak coupling makes it a potential dark matter candidate. However most parts of the cMSSM parameter space give a neutralino relic density that is too large and additional suppression mechanisms are needed to bring the relic density within observational bounds. One region where such suppression occurs is the $\tilde{\tau}$ coannihilation region, where the neutralino and the lightest $\tilde{\tau}$ masses are nearly degenerate, which leads to an enhanced $\tilde{\tau}$-$\tilde{\chi}_1^0$ coannihilation cross section. This allows for sufficient annihilation of neutralinos in the early universe to pass constraints on the dark matter relic density. The effects of experimental constraints on the cMSSM parameter space will be considered in more detail in chapter 4.

3.1.4 SUSY Solutions to SM Problems

Before we move on to the exploration of supersymmetric parameter spaces, we briefly revisit the problems discussed at the end of chapter 2.

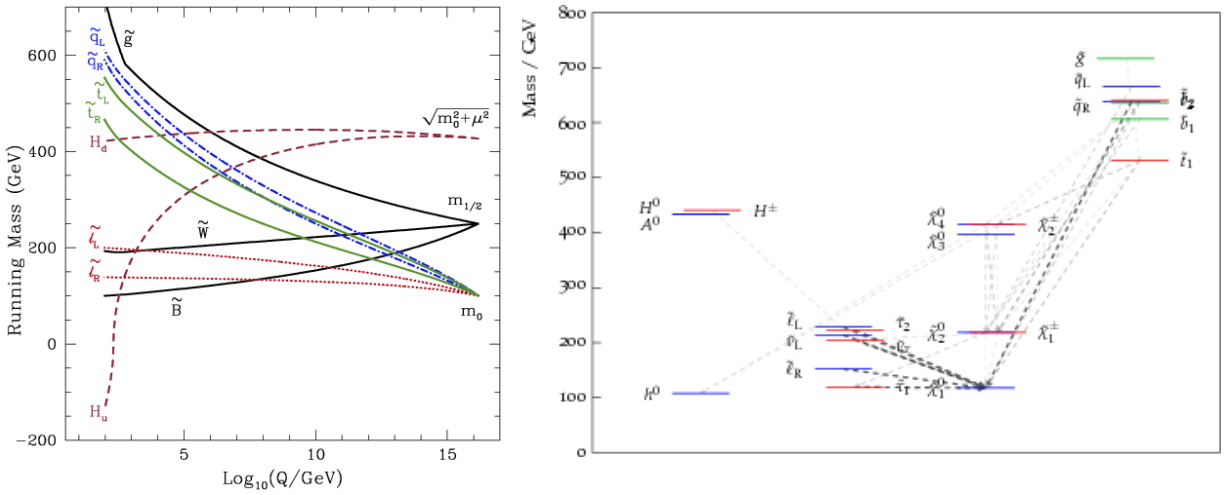

Figure 3.5: Right: Running of parameters from high energy (GUT) to the weak scale, taken from [77]. Left: Typical cMSSM spectrum, taken from [14]

- **Hierarchy Problem Revisited**

  The Hierarchy problem was one of the main reasons for introducing low energy supersymmetry, and in exact supersymmetry the new loop corrections to the Higgs mass cancel the Standard Model corrections exactly. This is no longer true in the MSSM where SUSY is broken, but as already mentioned the soft nature of the breaking terms ensures that the resulting corrections are at most logarithmic in the cut off Λ. Given soft breaking terms of order m^2_{soft}, the leading loop correction take the form [73]

$$\delta m_h^2 \propto m^2_{soft} \ln\left(\frac{\Lambda}{m_{soft}}\right) \tag{3.47}$$

  Thus if the superpartners are not too heavy $m_{soft} \lesssim 1\text{TeV}$, the MSSM stabilizes the Higgs mass. It should be noted that in solving the hierarchy problem, supersymmetry introduces a new problem referred to as the μ-problem. This refers to the lack of explanation for why the SUSY-respecting μ parameter and the SUSY breaking mass terms are of roughly the same order of magnitude, although they are seemingly unrelated. For a more detailed description and proposed solutions to the μ-problem, see [73].

- **Dark Matter Revisited**

  Due to R-parity, the Lightest Supersymmetric Particle (LSP) is stable and if weakly interacting provides a potential candidate for dark matter. The MSSM has several particles that fit the bill: The scalar sneutrino $\tilde{\nu}$, the neutralino χ_1^0 and the gravitino $\tilde{G}$ all fit the basic requirements. Sneutrino dark matter is heavily constrained by direct detection experiments [31] for masses below the TeV scale. Of the remaining

two, neutralino dark matter is most commonly considered and is also the scenario we consider in our scans. In this case, dark matter is assumed to be in thermal equilibrium in the early universe so that the dark matter production rate equals the annihilation rate. However as the universe expands, the annihilation rate drops until it is no longer sufficient to keep dark matter in equilibrium. At this point the dark matter decouples from the cosmic plasma and the comoving relic density becomes approximately constant. This mechanism, called thermal freeze out allows for much larger dark matter densities compared to equilibrium evolution, see figure 3.6.

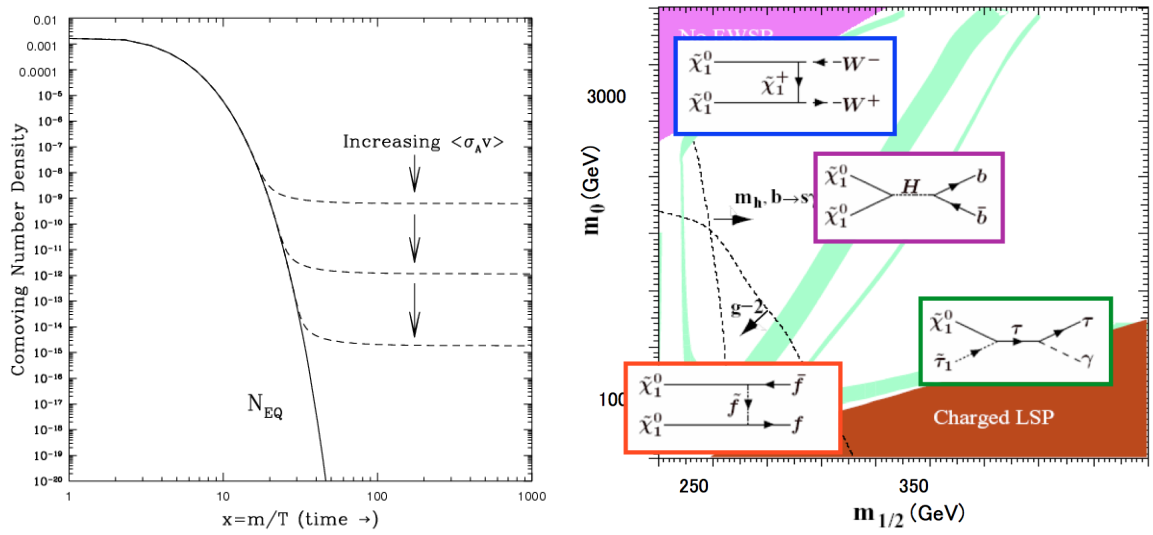

Figure 3.6: Left: Evolution of the comoving relic density as a function of inverse temperature for different thermally averaged annihilation cross sections. The solid line shows the equilibrium evolution of the comoving density. Taken from [31] Right: Plot showing the regions of cMSSM parameter space allowed by dark matter constraints (light green) and the enhanced processes associated with these regions. The band bordering the charged LSP region corresponds to the $\tilde{\tau}$ -coannihilation region and the associated diagram is given in the green box. Modified version of plot taken from [41]

The temperature at which this freeze out occurs, T_f, depends on the thermally averaged dark matter annihilation cross section $\langle \sigma v \rangle$, with higher cross sections giving a lower T_f and hence a smaller relic density. Assuming weak scale couplings and a mass in the range $m_\chi \sim 100\text{GeV} - 1\text{TeV}$ gives estimates for the relic densities roughly of the right order of magnitude, and this fact is sometimes referred to as the WIMP miracle. This is however a rough estimate, and as already mentioned the cMSSM generally gives too large relic densities, apart from small regions where the annihilation cross section is enhanced, see figure 3.6.

Despite having all these attractive features, there is still no indication from experiment that supersymmetry is realized in nature. This is not for the lack of trying as major efforts

are being made to determine whether low scale SUSY exists. In particular the Large Hadron Collider (LHC) at CERN [34] has the search for SUSY as one of its major goals. By accelerating protons through a 27 km long ring of superconducting magnets and having them collide in two general purpose detectors, ATLAS and CMS, the LHC is able to create sufficient energy to produce supersymmetric particles at the TeV scale.

Chapter 4

SUSY Parameter Scans

4.1 Introduction

The large number of free parameters in the MSSM give rise to large variations in the predicted phenomenology at colliders such as the LHC. If one wants to discover SUSY using a specific analysis focusing on specific phenomenological features, it is therefore important to know in advance which regions of parameter space are most promising, so the analysis can be optimized accordingly. The two main criteria for an interesting region from this perspective are how well the model fits current experimental data, and how well suited the analysis is for probing this region. Finding such regions has been the aim of our scan effort which gives it a slightly different perspective from other SUSY parameter scans [16, 14, 17, 84], which usually focus on finding precise best fit regions given current experimental data. Rather than trying to compete with the numerous projects dedicated to constructing such high resolution likelihood maps, our aim was to develop tools we could use to construct benchmark models suitable for optimizing the analysis done by our group, namely the ATLAS SUSY 1τ analysis. In what follows we present the results of these scans and the tools developed, where we focus on the unpublished results, leaving the published results for paper I.

In our approach we do not aim to give any precise measure of fit, but rather to get a crude idea of what regions are interesting. Based on these regions we then construct benchmark models based on phenomenological properties. The work was initiated in 2011 by Therese Sjursen, Thomas Burgess and Anna Lipniacka, who found that the official ATLAS cMSSM grids available at the time contained no models both detectable with τ's, and in accordance with basic experimental constraints on dark matter relic density, Higgs mass, and rare decays such as $b \to s + \gamma$. The ATLAS grids where all constrained to 2-dimensional m_0-$m_{1/2}$ planes with $\tan\beta < 40$, whereas the theoretical limit is closer to $\tan\beta \sim 60$ [1], and $A_0 \in \{0, 500\}$ GeV. As the constraints are sensitive to large values for these parameters, an extended search was initiated focusing on high $\tan\beta \in [30, 55]$, and an extended range for

[1] Beyond this limit, the Yukawa couplings receive large non-perturbative corrections

the trilinear coupling A_0. At this stage I started my PhD and started working on running scans and analyzing results. Using a grid scan over all the cMSSM parameters we were able to find multiple regions containing interesting models, which were summarized in a set of proposed benchmark models for optimizing the 1τ-analysis for 5fb^{-1} of data. This initial search will be covered in section 4.2.

Ultimately it was decided to focus on GMSB for the 5fb^{-1} 1τ-analysis [5], so none of the benchmark models were used. Despite this there was continued interest in the cMSSM within the Bergen analysis group, and it was decided to aim for benchmarks for 20 fb^{-1} instead. However by that time, around the end of 2011, there was already indications of a Higgs mass in the region of a 125GeV [1], whereas the models we found all had Higgs masses below 120GeV. It was therefore necessary to extend the search range and also increase the resolution of the search. Even for the simple cMSSM parameter space, the gridded scan approach initially used becomes hopelessly inefficient, and to perform scans on reasonable timescales using local computing resources required the implementation of a more sophisticated scanning algorithm. For this purpose we opted for a Markov Chain Monte Carlo (MCMC) approach [55], where we used the experimental constraints together with a measure of LHC discoverability to construct a target distribution quantifying how interesting models are from the point of view of discovery. Initial results, which later turned out to be due to a bug in the Higgs mass calculation of `FeynHiggs` 2.9.0 [64], indicated the existence of multiple disconnected regions of interest. Such disconnected regions are problematic to sample using ordinary mcmc as these algorithms tend to get stuck at local maxima. In order to tackle this problem we further developed our mcmc method to employ multiple adaptive mcmc chains with a multimodal sampling distribution. We also developed an algorithm for clustering the interesting models according to their phenomenology so as to automate the construction of benchmark models. This approach was then applied to look for regions of parameter space discoverable with τs using ATLAS 2012 data, and the results were published in summer 2013 [37]. This work will be discussed briefly in section 4.3 with the details given in paper I.

At the start of 2014, in connection with the recently initiated effort by ATLAS to interpret 2012 results in terms of the 19-parameter pMSSM, it was decided to extend our approach to the pMSSM and run II data. This presented a host of new challenges; First and foremost, the mere increase in the dimensionality of parameter space from 4 to 19 gives a drastic increase in search volume, which requires more computational resources even with the use of advanced scanning algorithms. Secondly, prompted in part by the efforts made by ATLAS to interpret existing analysis in pMSSM, and also by the growing use of LHC analysis in other scan efforts, it was decided to try also implementing these in our mcmc target distribution. This requires more detailed event simulation and analysis then what was used for our cMSSM paper making the calculation of constraints for each model much more computationally expensive. In order to tackle these computational issues we decided to adapt the code for running on the Bergen based supercomputer Hexagon. The code used for the cMSSM scan was based on shared memory parallelization, i.e on using multiple cpus

on a single computing node, while running on Hexagon requires distributed memory parallelization to allow running simultaneously on multiple nodes. We therefore had to adapt the scan algorithm to also allow for MPI parallelization. To this end the code was totally rewritten so as to decouple the scan and model dependent parts of the code, making it easy to extend and modify both model calculations and scan algorithms independently. This not only allowed us to implement both shared and distributed memory parallelization simultaneously, but also to create a more general framework including multiple different scan algorithms and where new models can be easily implemented without having detailed knowledge of the scan algorithm. At the time of writing this is still a work in progress, but the current state is presented in section 4.4.

All the code used to perform these scans where written in *python*, making heavy use of the *scipy* library [67]

4.2 Gridded CMSSM Scan

The first scan in which I participated was the search for more realistic cMSSM benchmark models for optimizing the 7 TeV Bergen 1τ-analysis. At the time, the analysis group was focusing on the cMSSM and had already performed a scan over the region of parameter space covered by the two ATLAS cMSSM high $\tan\beta$ grids, in search of non-excluded models with τ-rich signals [36]. The ATLAS grids consisted of 231 points with $\tan\beta = 40$, the top mass fixed at $m_t = 173$ GeV and $\mu > 0$. The first grid had $A_0 = 0$ GeV with $m_{1/2} \in [100, 340]$ GeV in steps of 30 GeV, and $m_0 \in [120, 1160]$ GeV in steps of 40 GeV below, and 80GeV above $m_0 = 240$ GeV. The other grid had $A_0 = 500$ GeV with m_0 starting at 240 GeV. In order to find viable models with τ-rich signals this search focused on a particular region of the cMSSM parameter space known as the $\tilde{\tau}$-$\tilde{\chi}_1^0$ coannihilation region, where the $\tilde{\chi}_1^0$ and the $\tilde{\tau}$ are the LSP and NLSP respectively, and where the mass splitting between the two is small, $\Delta M(\tilde{\chi}_1^0, \tilde{\tau}) < 20$ GeV. The small mass splitting gives an enhanced coannihilation cross-section which helps reduce the dark matter relic density to within cosmological bounds. Furthermore, since the $\tilde{\tau}$ is the lightest slepton in this region, the heavier neutralinos preferably decay into $\tau\tilde{\tau}$-pairs. This enhancement of branching fraction makes SUSY decays of the form fig. 4.1 particularly interesting, where the initially produced squark or gluino decay in multiple steps into final states containing the lightest neutralino and two τs.
With this in mind, preliminary constraints on the mass spectrum were implemented to focus on models in the coannihilation region where this decay chain was kinematically allowed. In addition the production cross section for the initial squark or gluino in the decay chain had to be observable using 2010 data, which roughly translated into an upper bound on the lightest squark or gluino mass of around 800 GeV.

For each model in the ATLAS grids the low energy mass spectrum and several observables where calculated using publicly available tools, including the dark matter relic density, Ωh^2

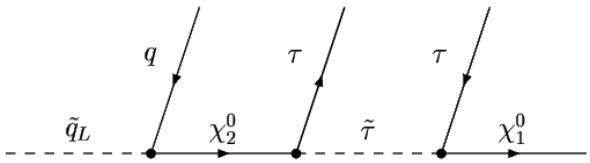

Figure 4.1: SUSY cascade decay giving a τs in the final state in a addition to jets and missing energy in the form of the LSP

and Br $(b \to s + \gamma)$, see section 4.2.1 for more details. Of the 231 models, none passed all constraints on the calculated observables and already disfavoured models had to be used as benchmark models for the 2010 analysis paper [36], see fig. 4.2.

Since none of the models in the existing ATLAS grids where physically viable it was decided to extend the scan range, in search of more suitable benchmark models, and in particular the high $\tan\beta$ region was considered interesting due to its influence on the Higgs mass. At this time I started working on the project and using code already developed, we extended the scan to higher values of $\tan\beta$ and multiple values for the trilinear coupling A_0, both positive and negative. This resulted in a set of benchmark points which where presented to the analysis group in November 2011.

4.2.1 Numerical Tools and Set Up

In order to calculate the model properties for the gridded scan we used `darkSUSY` 5.0.5 [56] in combination with `PROSPINO` 2.1 [28]. These tools where called from a python based wrapper which ran over the multidimensional grid using nested for loops, calling the external tools for each model and parsing the output. First `darkSUSY` was called to calculate the weak scale mass spectrum and decay rates using a built in version of `ISAJET`[78], in addition to the dark matter relic density and multiple accelerator constraints. In order to speed up calculations, the relic density was only calculated for models passing the accelerator and kinematic constraints. Subsequently, `PROSPINO` was called to calculate the 7 TeV $pp \to \tilde{g}\tilde{q}, \tilde{q}\tilde{q}$ and $\tilde{g}\tilde{g}$ NLO cross-section for the models passing the relic density constraint. As the NLO cross section calculation is very computationally expensive, these were calculated in parallel using simple bash scripting.

4.2.2 Search Range and Constraints

The scan was done by setting up a 5-dimensional grid made up of 1138270 models, where the parameter range and resolution chosen for the parameters are given in table 4.1
The upper limits for the scalar and gaugino masses m_0 and $m_{1/2}$ where chosen in part based on SUSY naturalness and potential ATLAS reach, while the lower limits on the masses where based on ATLAS exclusion limits from the 35pb^{-1} of 7 TeV data, see fig. 4.2.

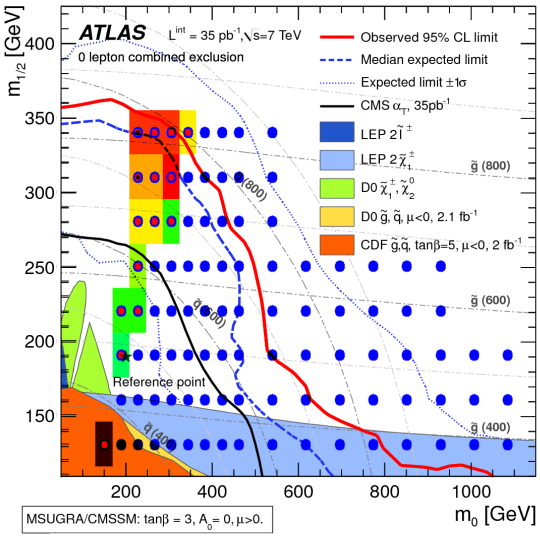

ATLAS scan

Figure 4.2: Scan over ATLAS grid with $\tan\beta = 40$, $A_0 = 0$ and $\text{sign}(\mu) = +1$ superimposed onto the 35 pb^{-1} ATLAS 0-lepton exclusion limits for $\tan\beta = 3$, $A_0 = 0$ and $\text{sign}(\mu) = +1$. The blue circles indicates points scanned, with red filling indicating τ-decay modes. The squares indicate the Higgs mass, with red and yellow passing the mass constraint $m_h 0 > 110$ GeV. The two points with black dots correspond to the points chosen as benchmark models. Taken from [36]

x	$[x_{\min}, x_{\max}]$	dx	#
m_0	$[400, 1200]$	5	161
$m_{1/2}$	$[300, 800]$	5	101
A_0	$[-1000, 1000]$	500	5
$\tan\beta$	$[30, 60]$	5	7
$\text{sign}[\mu]$	$\{-1, +1\}$	–	2
Total # points			1138270

Table 4.1: Parameter Range for gridded cMSSM Scan

The values chosen for the trilinear coupling A_0 where chosen so as to extend the range covered by the ATLAS grids and also consider negative values of A_0. The $\tan\beta$ range was restricted to high $\tan\beta$ regions, where the upper limit is the maximal value allowed by `darkSUSY`and is set to ensure that the Yukawa couplings remain perturbative [23]

For a model to be considered viable, it is required to pass the following constraints

- **Theoretical (`ISAJET`):** $\tilde{\chi}_1^0$ LSP, correct EWSB, no tachyons

  These are consistency checks performed during the spectrum calculation and are necessary conditions for reliable model calculations

- **Accelerator (`darkSUSY`):** Sparticle mass, $\text{Br}(b \to s\gamma)$, ρ-parameter, invisible Z width

  These constraints are checked internally by `darkSUSY` as described in [57]. Of particular interest is the branching fraction for the charmless bottom decay , $\text{Br}(b \to s\gamma)$ and the Higgs mass m_{h0}. $\text{Br}(b \to s\gamma)$ is required to lie within 2σ of the experimental best-fit value [27]

  $$\text{Br}(b \to s\gamma) = (3.55 \pm 0.42) \cdot 10^{-4} \tag{4.1}$$

  where a theoretical uncertainty of $\sigma_{th} = 0.33$ is assumed. The Higgs mass constraint is based on the combined LEP lower limit $m_{h0} > 114.4$ GeV [26]. Due to uncertainties in the calculated Higgs mass, primarily from the exact value of the top mass, and the fact that the Higgs mass limits assume a standard model Higgs, a more conservative constraint was chosen.

  $$m_{h0} > 110 \text{ GeV} \tag{4.2}$$

- **Kinematic:** $M_{\tilde{q}/\tilde{g}} > M_{\tilde{\chi}_2^0} > M_{\tilde{\tau}_1} > M_{\tilde{\chi}_1^0}$

  This is the requirement imposed for the SUSY cascade decay in fig. 4.1 to be kinematically allowed

- **Coannihilation:** $5\text{ GeV} < \Delta M(\tilde{\tau}_1, \chi_1^0) < 20\text{ GeV}$

  Constraint on $\tilde{\tau}_1, \chi_1^0$-mass splitting in order to ensure efficient coannihilation. The lower limit is imposed to ensure that the second τ in the decay chain is sufficiently energetic to be observed.

- **Relic Density:** $\Omega_\chi h^2 \in (1 \pm 0.3)\Omega_{\text{obs}} h^2$

  Constraint on the dark matter relic density coming from WMAP7 $\Omega_{\text{obs}} h^2 = 0.1138$ [70][2]. Again the uncertainties used are primarily calculational, since the relic density is extremely sensitive to the exact value of the $\tilde{\tau}_1, \chi_1^0$-mass splitting in the coannihilation region.

- **NLO cross-section:** $\sigma_{NLO} > 0.01$ pb

  Finally, the cross section constraint is chosen such that we would expect to see at least some SUSY events in the 2011 (2012) data, corresponding to a projected integrated luminosity of $\mathcal{L}_{int} \approx 5$ (20) fb^{-1} and roughly 50 (200) SUSY events.

4.2.3 Results and Benchmark Models

Although we scanned the cMSSM parameter space for sign(μ) = ± 1, only models with positive sign survived all the constraints. This is mainly due to the lack of a coannihilation region for all but the largest negative values of A_0, with the remaining models having cross sections of order 10^{-4} *pb*. Furthermore almost all the points at $\tan\beta = 60$ fail already at spectrum generation due to perturbative breakdown, with none of the remaining models being consistent with both accelerator constraints and the kinematic requirements. For this reason we chose to focus on positive sign(μ) with the highest $\tan\beta$-planes also omitted. A summary of the impact of the different constraints are given in table 4.2

The impact of the theoretical constraints are most significant at high $\tan\beta$ and for large negative values of A_0. This is mainly due to a larger portion of the low m_0 region giving a $\tilde{\tau}$-LSP, as can be seen from fig. 4.3. For large negative values of A_0, a significant fraction of the low $m_{1/2}$ region also fails due to incorrect EWSB [24].

Of the accelerator constraints, Br($b \to s + \gamma$) is the most stringent, affecting the low $m_{1/2}$-m_0 region, where negative SUSY contributions to the branching fraction make it smaller than the experimental value [22]. However, as can be seen from fig. 4.3, the Higgs mass is often small compared to the LEP limit of $m_{h0} < 114.4$ GeV which would give stringent constraints on the low $m_{1/2}$ region for all but the largest negative A_0 if taken at face value, see fig. 4.4.

[2]This value was actually not the best fit presented in this paper which was $\Omega h^2 = 0.1109$, but rather corresponds to an input parameter for a bias test. The impact of this difference is negligible for out purposes

Constraint	# Passed	# sign(μ) = +1	# sign(μ) = −1
Theory	808308	456136	352172
Accelerator	584612	425027	159585
Coannihilation & Kinematics	3685	3658	27
Ωh^2	857	850	7
$\sigma_{NLO} > 0.01$	140	140	0

Table 4.2: Summary of effect of the different constraints

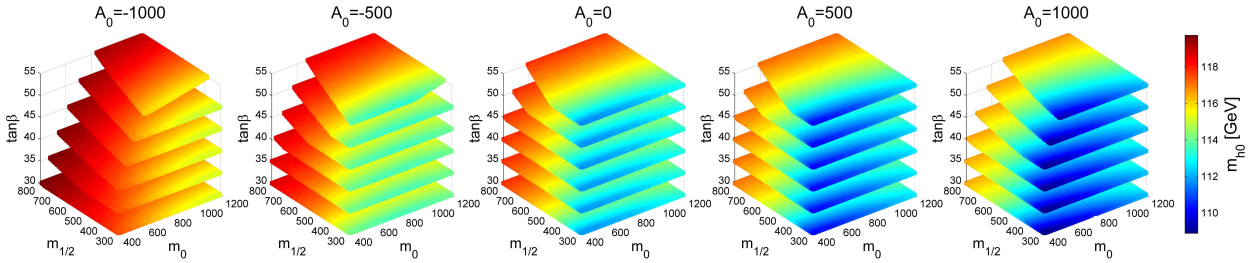

Figure 4.3: 3D map of models after theory exclusion for sign(μ) = +1 where the colormap indicates the Higgs mass. The missing regions along the $m_{1/2}$ axis is due to a $\tilde{\tau}$-LSP, while the region along the m_0-axis for high tan β and large negative A_0 is due to incorrect EWSB.

When it comes to the kinematic and coannihilation constraints, the gluino and the lightest squark are generally heavier than $\tilde{\chi}_2^0$ and the mass splitting between the $\tilde{\chi}_2^0$ -$\tilde{\chi}_1^0$ mass splitting is also generally larger than 20 GeV. This means that satisfying the coannihilation constraint is sufficient for the kinematic requirements to be fulfilled since the mass of the neutralino is roughly proportional to the sfermion mass $m_{1/2}$, and the $\tilde{\tau}_1$ mass is roughly proportional to the scalar mass m_0. The region where they are almost degenerate forms bands around the $\tilde{\tau}$-LSP boundary seen in fig. 4.3, and requiring this mass difference to be in the range 5 GeV $< \Delta M(\tilde{\tau}_1, \chi_1^0) <$ 20 GeV drastically reduces the available parameter space as seen in fig. 4.5.

The bands remaining after the coannihilation constraint is further narrowed by the direct constraint on the neutralino relic density calculated by `darkSUSY`. This is due to coannihilation being either too efficient close to the $\tilde{\tau}$-LSP boundary yielding too small relic densities, or not sufficient enough for the largest mass splittings, giving too high relic densities. Furthermore in the high tan β region the $\tilde{\tau}$-$\tilde{\chi}_1^0$coannihilation overlaps with the so called Higgs-funnel region [51] where the relic density is further suppressed by direct annihilation of two neutralinos into the heavy neutral Higgses H_0 and A_0. This leads to

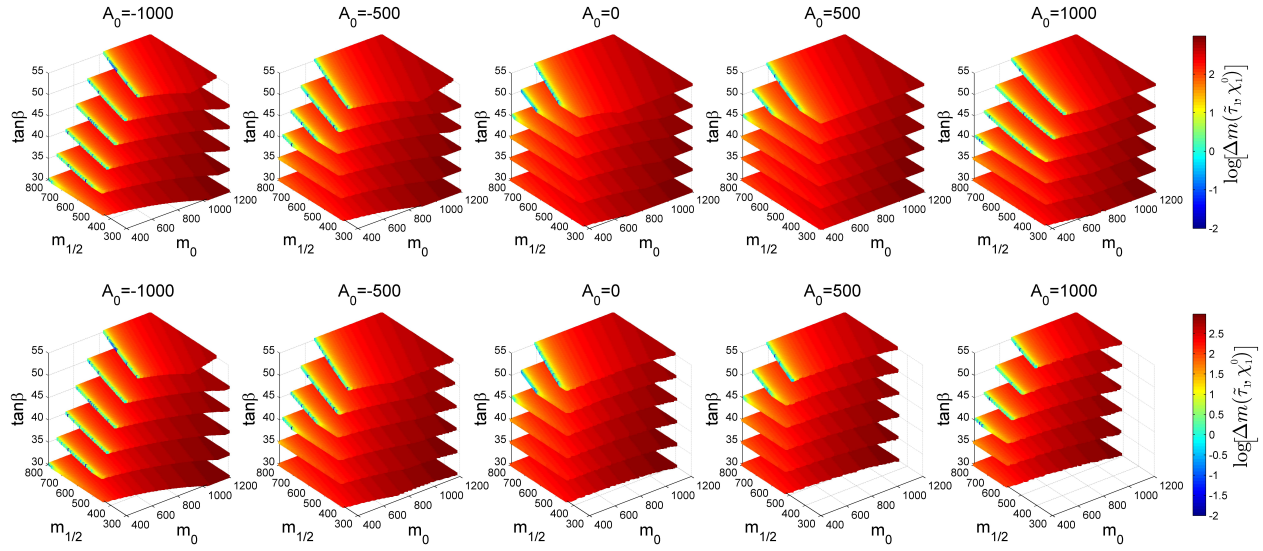

Figure 4.4: Top: 3D map of models after theory exclusion, where the colormap this time indicates the $\tilde{\tau}_1$-$\tilde{\chi}_1^0$ mass splitting. Bottom: Same plot but using the LEP Higgs mass limit $m_{h0} < 114.4$ GeV directly.

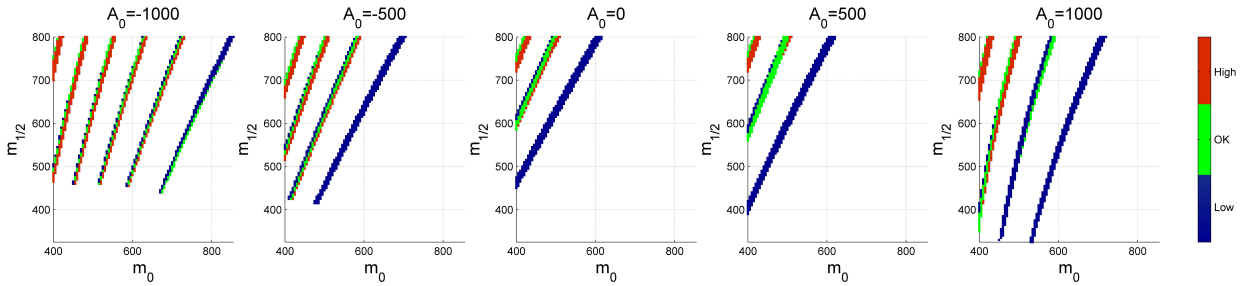

Figure 4.5: Coannihilation strips projected onto the mass plane, where the strips are shifted to the right with higher $\tan\beta$. The colormap indicates whether or not the relic density is within the allowed range.

the exclusion of almost all remaining models at $\tan\beta = 55$.

Finally the NLO cross section which was calculated for the remaining 850 models cuts away a considerable portion of the high $m_{1/2}$ region, due to the cross-section decreasing exponentially with the mass of the lightest squark/gluino. After all constraints only 140 models remain as distributed in fig. 4.6, where large values for the trilinear coupling A_0 are favoured.

This is mainly due to the coannihilation regions shifting to higher values of m_0 with in-

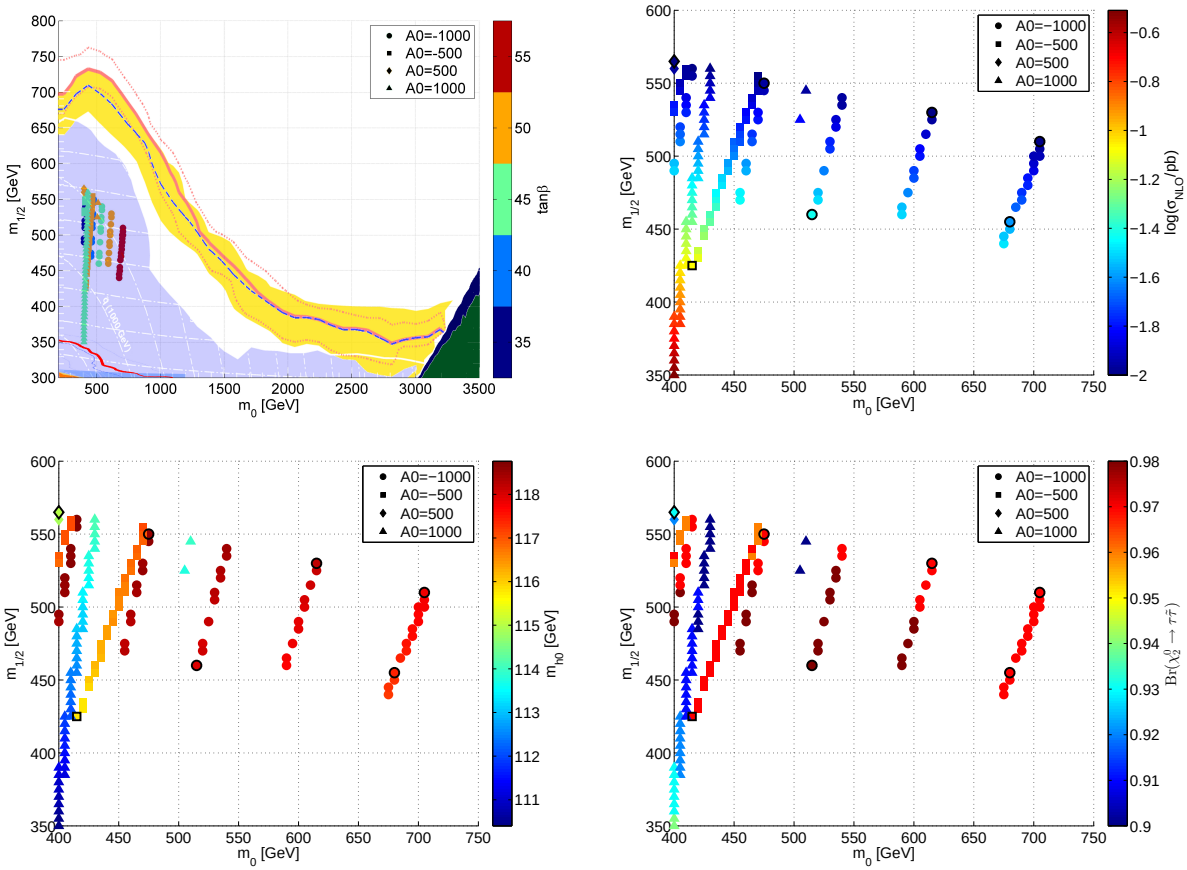

Figure 4.6: Final models projected onto the mass plane, where the colormap indicates the value of $\tan\beta$. top left: models with respect to ATLAS 0-lepton exclusion limits shown in fig. 4.2 (lower solid red line) together with the 4.7fb^{-1}, 7 TeV and 5.8fb^{-1}, 8 TeV 0-lepton limits [2] for $\tan\beta = 10$, $A_0 = 0$ and $\text{sign}(\mu) = +1$ (light blue shaded region and the upper solid red line respectively). Top right and bottom: The same models with the colormap indicating the LHC SUSY cross section σ_{NLO} (top right), the Higgs mass m_{h0} (left bottom) and branching fraction to τs, $\text{Br}(\chi_2^0 \to \tilde{\tau}\tau)$ (right bottom). The points with heavy black borders correspond to the presented benchmark models.

creasing $|A_0|$, allowing for lower values of $m_{1/2}$, which again leads to higher LHC cross sections. Furthermore, due to the A_0 dependence of the Higgs mass seen in fig. 4.4 and fig. 4.6 the models remaining at $A_0 = 1000$ GeV give small Higgs masses compared to the LEP limit. This leaves the regions with large negative values of A_0 as the most promising. Of these models a selection of 7 benchmark models where suggested as shown in table 4.3 and fig. 4.6. Particular emphasis was put on the $A_0 = -1000$ GeV which seemed like the most promising, but two models with $A_0 = \pm 500$ GeV were also included. The models with $A_0 = 1000$ GeV were omitted from the list of benchmark points due to the whole

region being at odds with the LEP Higgs mass constraint.

m_0	$m_{1/2}$	A_0	$\tan\beta$	$\mathrm{Br}(\chi_0^2 \to \tilde{\tau}\tau)$	M_{h_0}	Ωh^2	σ_{NLO}[pb]	err_{NLO}[pb]
705	510	-1000	55	0.9718	117.81	0.082	0.01	0.0016
680	455	-1000	55	0.9744	117.42	0.095	0.025	0.0016
400	565	500	50	0.9306	115.03	0.091	0.01	0.002
415	425	-500	50	0.9727	115.79	0.096	0.084	0.002
615	530	-1000	50	0.9735	118.21	0.102	0.01	0.0016
515	460	-1000	45	0.9783	117.96	0.092	0.038	0.0017
475	550	-1000	40	0.9731	118.56	0.099	0.011	0.0019

Table 4.3: Suggested sample points

These models where presented at one of the ATLAS *SUSY with τs* meeting with the aim of getting centrally produced monte carlo samples for the 5fb^{-1} 1τ analysis. As already mentioned this did not happen primarily due to the decision of combining the 1τ with the 2τ analysis focusing on GMSB rather than cMSSM. Regardless of this it was decided to aim for a paper describing the search with the focus shifted towards models suitable for a 20fb^{-1} analysis. However by this time (early 2012) new experimental data required us to rethink our approach. First of all the new combined ATLAS Higgs results [1] seemed to indicate a Higgs mass around 125 GeV which was incompatible with all the models from the initial scan. Secondly, new results from CMS [40] and [8] gave much stronger limits on the SUSY sensitive branching fraction $\mathrm{Br}(B_s \to \mu\mu)$ making this a more important constraint to consider. In addition the initial grid search indicated that the allowed regions actually correspond to hypersurfaces of the full parameter space, which is banded due to the coarse grained gridding. In order to get a more detailed map of these surfaces and to incorporate the new constraints a more efficient search algorithm was needed. This was the starting point for the new mcmc based scan effort briefly described in the next section and more thoroughly in paper I.

4.3 MCMC Based cMSSM Scan

The basic idea for this scan was to combine the experimental and theoretical constraints with a measure for the discovery potential to construct a likelihood distribution P. Using this likelihood as the target distribution in an mcmc based scan allowed us to focus on the most interesting regions as quantified by the likelihood, without spending valuable computational resources on sampling low likelihood regions. From the set of models ob-

tained, a representative set of benchmark points were selected based on phenomenological properties of the models. To construct a measure for the discovery potential, additional simulation of LHC SUSY events were performed using `Pythia` 8 [83], which allowed us to get a leading order estimate for the SUSY tau-production at the LHC, in addition to several phenomenological parameters such as the mean number of taus, transverse momentum and missing energy. These parameters where subsequently used to cluster the models according to phenomenology using a g-means clustering algorithm [62], from which benchmark models where constructed. The implementation of this mcmc approach took nearly a year to complete, involving several iterations of the algorithm. Beginning with a simple Metropolis-Hasting algorithm [63], the code was parallelized and made adaptive in order make the algorithm more efficient and to account for potentially separated high likelihood regions. Over this period several updates of the various constraints where included, most notably the discovery of the decay $B_s \to \mu\mu$ [7], and the Higgs particle [4]. The details of the analysis is given in paper I, which presents a set of 10 benchmark models potentially discoverable using the 2012 LHC data set.

The results of the scan were used as a basis for one of the cMSSM grids studied by Knut Dundaas Mora in his master thesis [75], and one of the benchmark models were used in a study of additional non-holomorphic soft SUSY breaking terms to the MSSM [88]. None of the models were used directly in the ATLAS 21fb^{-1} analysis [3], which again mainly focused on GMSB. However limits where interpreted in a high Higgs mass cMSSM grid defined by $A_0 = -2m_0, \tan\beta = 30$, which corresponds to a plane in parameter space similar to the region found by our scan. The main result of the work however, was the actual framework which was built to be easily adaptable to other simplified SUSY scenarios such as GMSB and to make it easy to customize the likelihood both with regards to experimental constraints and criteria for discoverability. The plan was to continue refining the code and perform similar studies for GMSB and other signatures, in addition to making the tool publicly available. However as the end of the first cMSSM study coincided with the start of my stay as a guest researcher at the University of Oslo, this plan was put on hold until the start of 2014. By this time the focus was starting to shift from simplified models to more complicated scenarios such as the pMSSM, and in order to handle the increased complexity it was necessary to upgrade our framework . As already mentioned this lead us to build a new modular framework, but also required the implementation of new constraints and changing several of the external tools used for calculating observables. This project, which is a work in progress, is the topic of the next section.

4.4 MCMC Based pMSSM Scan

Early 2014, the ATLAS collaboration started an effort to apply multiple existing analysis to dark matter compatible regions of pMSSM which resulted in a summary paper for Run 1 [6]. This effort took as a staring point a pre-existing scan of the 19 parameter pMSSM made by Tom Rizzo et. al [38], consisting of roughly 300000 models passing a large set

of experimental constraints. In addition to the constraints used for our cMSSM scan, this set included direct detection limits on dark matter from LUX [12] and COUPP [29] and XENON100 [21], the $(g-2)_\mu$ constraint discussed in paper I, and several additional constraints on B-meson decays. A subset of these models having a potentially observable cross section where used to constrain pMSSM using multiple ATLAS analysis, where our group in Bergen was responsible for the implementation of the τ-analysis. However the ATLAS pMSSM sample was found using a uniform random scan, which as already discussed becomes inefficient for high-dimensional parameter spaces. The plan was therefore to use our mcmc based scan algorithm, implementing the same set of constraints, and see whether additional acceptable regions of parameter space exist which might have been missed due to the uniform sampling technique. However in order to perform such a scan several obstacles needed to be overcome, including changing external tools and adding new observables used for model evaluation and rewriting the algorithm to accommodate running on supercomputers.

4.4.1 Updated Tools and Observables

First we needed to implement the additional constraints and preferably use the same set of tools to ensure any differences where due to scan algorithm rather than discrepancies between calculated observables. In terms of the tools used this amounted to changing spectrum generator from `ISAJET` to `SOFTSUSY` [13] and `SUSY-HIT` [47], and using `micrOMEGAs` [30] rather than `darkSUSY` for calculating relic density related parameters. In addition we wanted more precise predictions for the LHC phenomenology. To this end we used `MadGraph` [19] to calculate pMSSM scattering amplitudes, and set up `Pythia` so as to use these for event generation. We also included `Delphes` [44] in order to include detector simulations. Furthermore Rizzo et. al implemented several modifications to `micrOMEGAs` and `SUSY-HIT` including updating hard-coded SM parameters and corrections to the calculation of sparticle decays. With their help we where able to update our versions of these tools so as to have matching SM parameters and settings, however we did not have the resources or expertise to implement the more substantial modifications, such as the improved sparticle decay calulations. The new tools and related parameters are listed in table 4.4
The ATLAS analysis included several constraints we did not consider in our scan, and many of them turned out to be far from easy to implement. We therefore decided to initially focus on what we considered to be the most important additions, namely the neutralino nucleon cross sections $\sigma_{\chi N}$ needed for direct detection constraints from LUX, COUPP and XENON100 . Furthermore as the SUSY contributions to the invisible Z-width $\Delta\Gamma_Z^{\text{inv}}$ were checked by `ISAJET` but not by `SOFTSUSY` this had to be implemented using analytic expressions for the leading order contributions calculated in [46].

4.4.2 SUSYScanner: Parallelized Scanning Tool

The main obstacle in implementing a pMSSM version of the scan was handling the increased dimensionality of the parameter space, which leads to a huge increase in search

Tool	**Information used**
SOFTSUSY3.5.1 & SUSY-HIT1.4 (modified)	SUSY masses and decays
FeynHiggs2.10 & HiggsBounds 3.8.1	Higgs sector
micrOMEGAs3.5.5 (modified)	$\sigma_{\chi N}$,$\Omega_\chi h^2$, $\mathbf{Br}\,(B_s \to \mu\mu)$, $\mathbf{Br}\,(b \to s\gamma)$,$(g-2)_\mu$,$\Delta\rho$
Pythia8.2 w. MG procs	σ_{LO}, showered LHC events
Delphes3.1.2 (PROSPINO2.1)	Detector simulation, object reconstruction (NLO k-factors)

Table 4.4: Software tools and resulting information employed in this work. Average values from Pythia are for final states objects with $|\eta| < 2.5$ and $p_T > 20$GeV.

volume. Although the use of mcmc relieves this problem, more models are still needed to get an acceptable resolution. In addition, constructing the initial map over high likelihood regions for the original mcmc algorithm required random sampling whose efficiency depends critically on the dimensionality of parameter space. Based on these considerations, in addition to our local computing resources being strained, we decided to modify the code for running on the Bergen supercomputer Hexagon, which potentially could speed up the efficiency of the algorithm considerably by using many more chains to increase sampling rate, while at the same time using multithreading for speeding up cross section calculations. Being able to use supercomputers also opens up for the possibility to perform more accurate analysis of each model using larger Pythia samples for each model, including detector simulations and NLO calculations, and even performing crude cut based analysis on the events to implement existing ATLAS constraints. The code used for the cMSSM scan was based on the python module `multiprocessing` [82] which is built for shared memory parallelization and restricted to running multiple processes on a single machine. However Hexagon consists of many linked machines (nodes) and requires distributed memory parallelization (MPI) in order to use more than a single node. We therefore had to rewrite the code to also be able to use MPI, through the python module `MPI4py` [43]. At this point several independent scripts had been written to perform random uniform scans, grid scans and mcmc scans, and at least the mcmc and uniform random scans had to be modified to use MPI, and to scan over pMSSM rather than the simpler cMSSM. In addition there was some interest in continued use of the scan codes after the end of my PhD, which would be made much easier by having the different scan algorithms and parallelization schemes in a single code. We therefore decided to combine the existing scripts into a single framework where the choice of algorithm, parallelization scheme etc. could easily be changed by the user through a steering file. Furthermore we also wanted to make the code modular to allow users to implement new models and scan algorithms without having to rewrite the whole code. In the process, the adaptive mcmc algorithm used in [37] was modified to run without needing an initial guess for the proposal distribution. If no initial distribution is provided, the algorithm launches the mcmc chains using only local steps and constructs

the global proposal distribution on the fly based on previous results. At the moment this works fairly well in low dimension $D \lesssim 6$, but leads to instabilities as the dimensionality increases. This is a flaw in the current implementation rather than the algorithm as previous versions have been stable up to at least 19 dimensions.

The product of this effort is the code `SUSYScanner` which is available for download at `https://github.com/JanLindroos/SUSYScanner`. At the time of writing, uniform random, gridded and ordinary mcmc algorithms have been tested on multiple machines in multiprocessing mode, but the new implementation of the adaptive mcmc algorithm should be optimized and tested more thoroughly and is therefore currently only available in the development branch of the code. Furthermore tests of the latest updates to the code have not yet been performed on hexagon and may present some problems. In particular the removal of the dill module [74] necessary for running the code at UiO is expected to cause some problems, and the installation of the SUSY tools must probably be done manually[3].

The code SUSYScanner is built in a modular fashion with four main components: A parallelization library responsible for launching parallel chains and handling communication, the algorithm library which performs the actual sampling and contains the different sampling algorithms, a model class defining the model to be sampled and a steering file specifying the choice of parallelization scheme, sampling algorithm and model. In addition it contains libraries for handling IO and maintenance tasks. The main features of the program structure is illustrated in fig. 4.7

The code is run by launching `run_scan.py` which takes the path to a steering file as input argument. This steering file is then parsed and the user provided input is passed to a launcher which is responsible for launching multiple parallel scans using the parallelization scheme, sampling algorithm and model specified in the steering file. a few example steering files are provided with the code. The model independent output of the code is a delimiter separated data file containing model IDs, weights, likelihoods, error codes and input parameters in addition to any parameters calculated based on the input parameters. More detailed information can be found in the provided README file.

At the moment two models have been implemented:

- **Gaussian Mixture Model**
  The first model is a Gaussian mixture model, which is a collection of differently weighted multivariate normal distributions. In addition to the model class, which does little more than calculate the log likelihood, the model contains a distribution library containing tools to generate mixture models. The examples folder contains steering files for a uniform random scan, an ordinary multichain mcmc scan, and an

[3] In order to ease manual installation, the installation script contains an *extract* option which extracts the tools to the correct location without installing them.

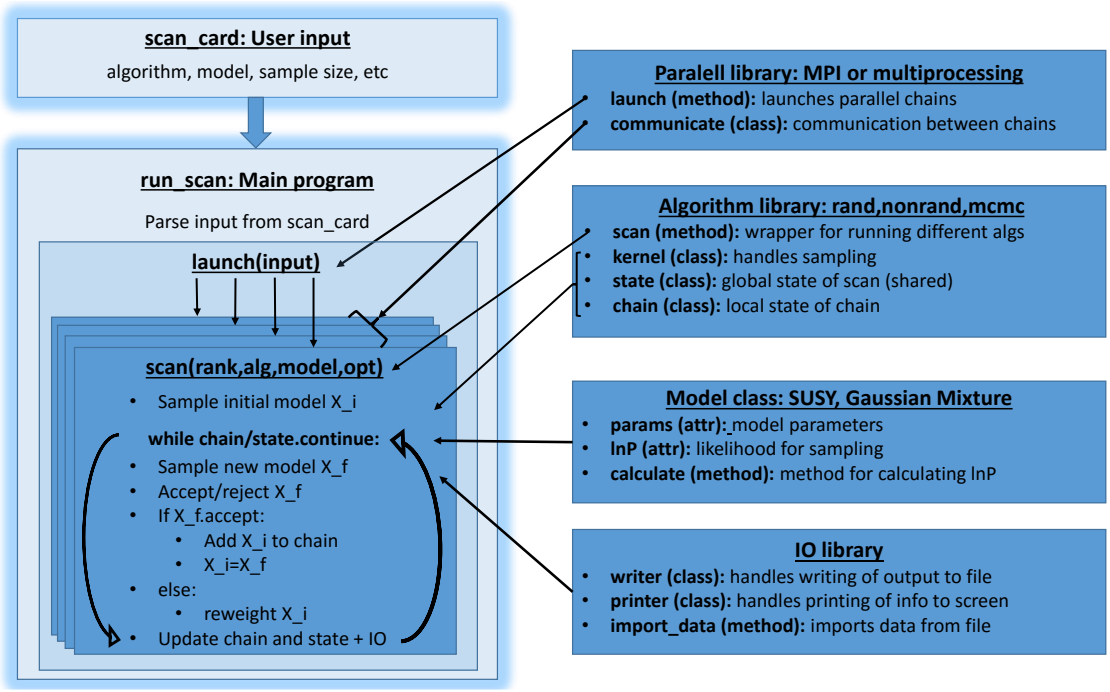

Figure 4.7: Schematic representation of the SUSYScanner structure

adaptive mcmc scan (in the dev branch) of this model. This provides a convenient test bench for both scan algorithms and clustering algorithms since the distribution can be analytically integrated and has a well defined number of clusters. As a test of the different algorithms we consider a Gaussian mixture with three components of equal weight in 6 dimensions given with the analytically marginalized 2D distribution given in figure 4.8

we can now compare the analytic distribution with the results obtained using the random, ordinary mcmc and adaptive mcmc samplers. Each algorithm is run for roughly 10 minutes using 20 chains, where the models are required a minimum likelihood of $\ln P_{\min} = -10$ to be accepted. The resulting marginalized likelihood distributions are shown in figure 4.9, where the third component is hardly visible in this projection, but is situated just above the origin

These plots show some typical features of the different samplers. First of all we see that already in 6 dimensions, the uniform random sampler is much less efficient, this is due to the fact that it samples the whole volume rather then exclusively in the high likelihood regions. Secondly we see that although the ordinary mcmc algorithm gives a good approximation for each component individually it fails at giving the correct relative size. This is due to the fact that the individual chains are unable to traverse the low likelihood regions in between the two main components and hence each individual chain only samples a single component. This is solved by the large jumps implemented into the adaptive mcmc, where all chains now sample all three

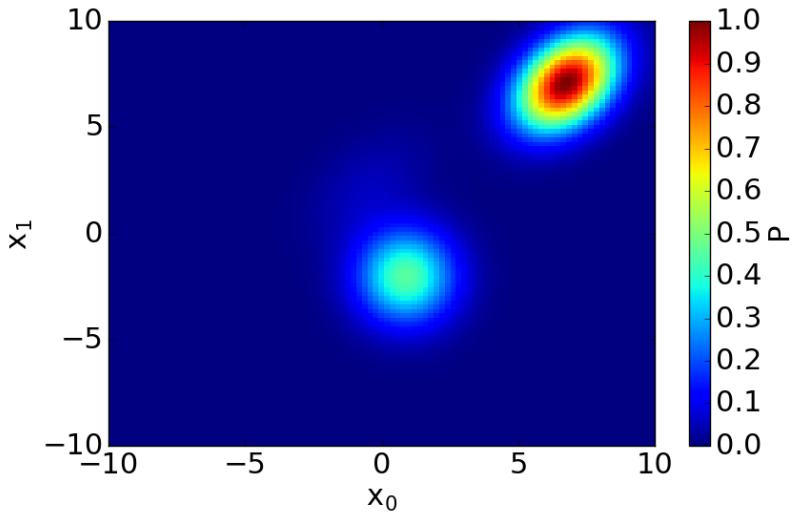

Figure 4.8: Analytically marginalized test distribution for a three component Gaussian mixture

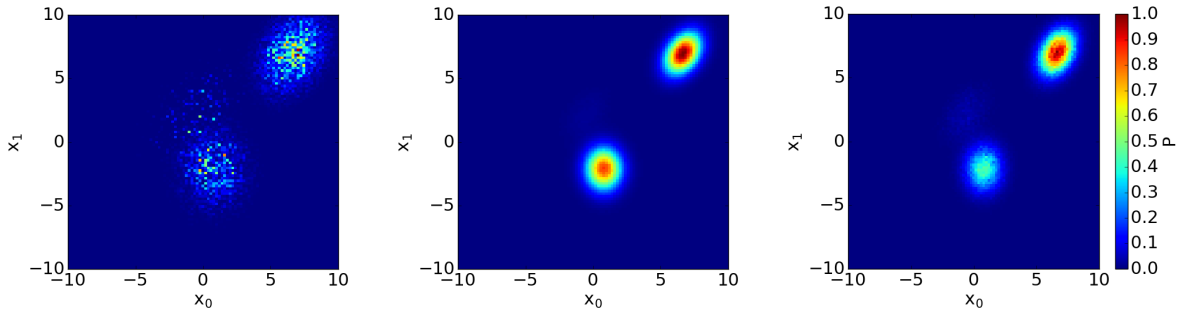

Figure 4.9: Comparison of scan results for three different algorithms which ran for roughly 10 minutes over the Gaussian mixture model shown in figure 4.8. Left: uniform random, middle: multichain mcmc, right: adaptive multichain mcmc

components.

- **SUSY Model**

  The SUSY model is responsible for everything SUSY related and contains the external tools used for calculating the mass spectrum and observables. These are called from a library containing wrapper methods for these tools, where the information about the model is propagated between the tools using the slha interface [15]. The details of the SUSY model such as the specific choice of breaking mechanism, constraints imposed and details of the LHC event generation can all be set in the steering files. A schematic representation of the SUSY model class is given in figure 4.10

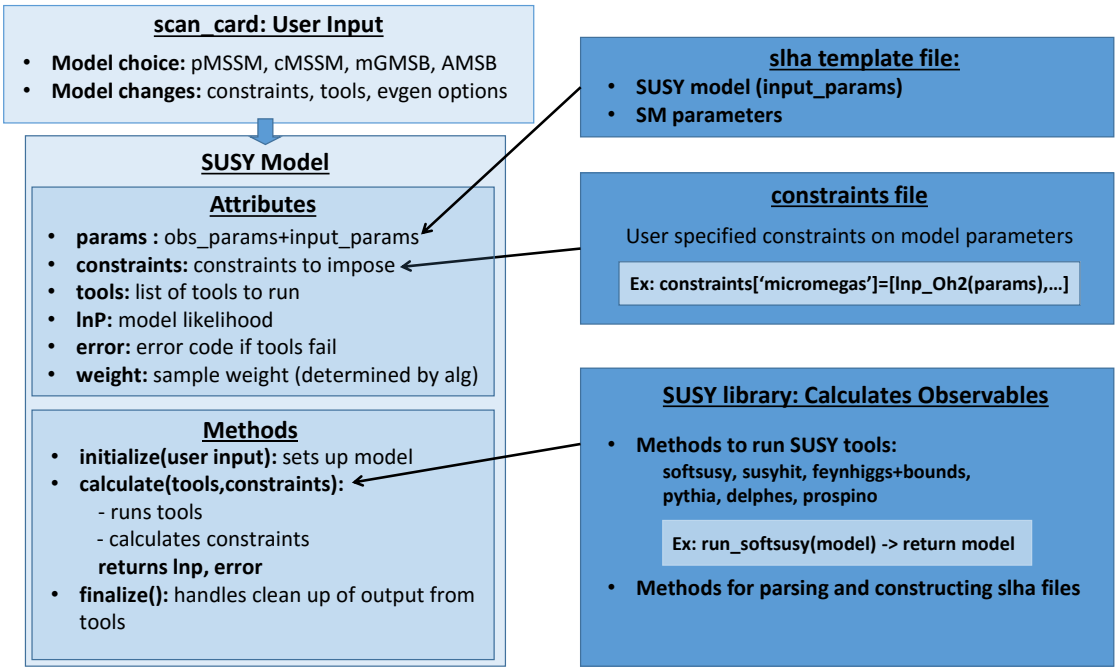

Figure 4.10: Schematic representation of the implementation of SUSY in the code

In addition to the default parameter data file, the user can also specify additional output to keep, namely the slha files produced by the spectrum generators, `HEPMC` event files [48] produced by `Pythia` and `ROOT` files [35] from `Delphes` containing reconstructed events. These are intended for the implementation of LHC constraints, which is currently not implemented. Finally the model also contains an installation script for setting up the external tools.

4.4.3 ATLAS Comparison

In order to validate the tool chain we were given access to the full ATLAS pMSSM sample, where we focus on a subset containing 113357 models with a bino like neutralino $\tilde{\chi}_1^0$Ůsing the same model parameters we recalculated all the observables except for the LHC cross section. Of these models, 31 where rejected, 7 due to LEP constraints on the chargino mass and 24 due to NaNs in the `SUSY-HIT` decay tables. For the remaining models we checked the agreement of several different distributions for the observables used to constrain the models, see figure 4.11. In general we found good agreement between the two samples

The LHC production cross sections was checked for small random subsets of the ATLAS sample for earlier iterations of the tool, but not yet for the new framework. In order to implement ATLAS constraints in the likelihood function it is also necessary to validate the simulated signal samples obtained using `Pythia`and `Delphes`. As should be clear from this review, the SUSYScanner package still has some way to go with regards to reaching the

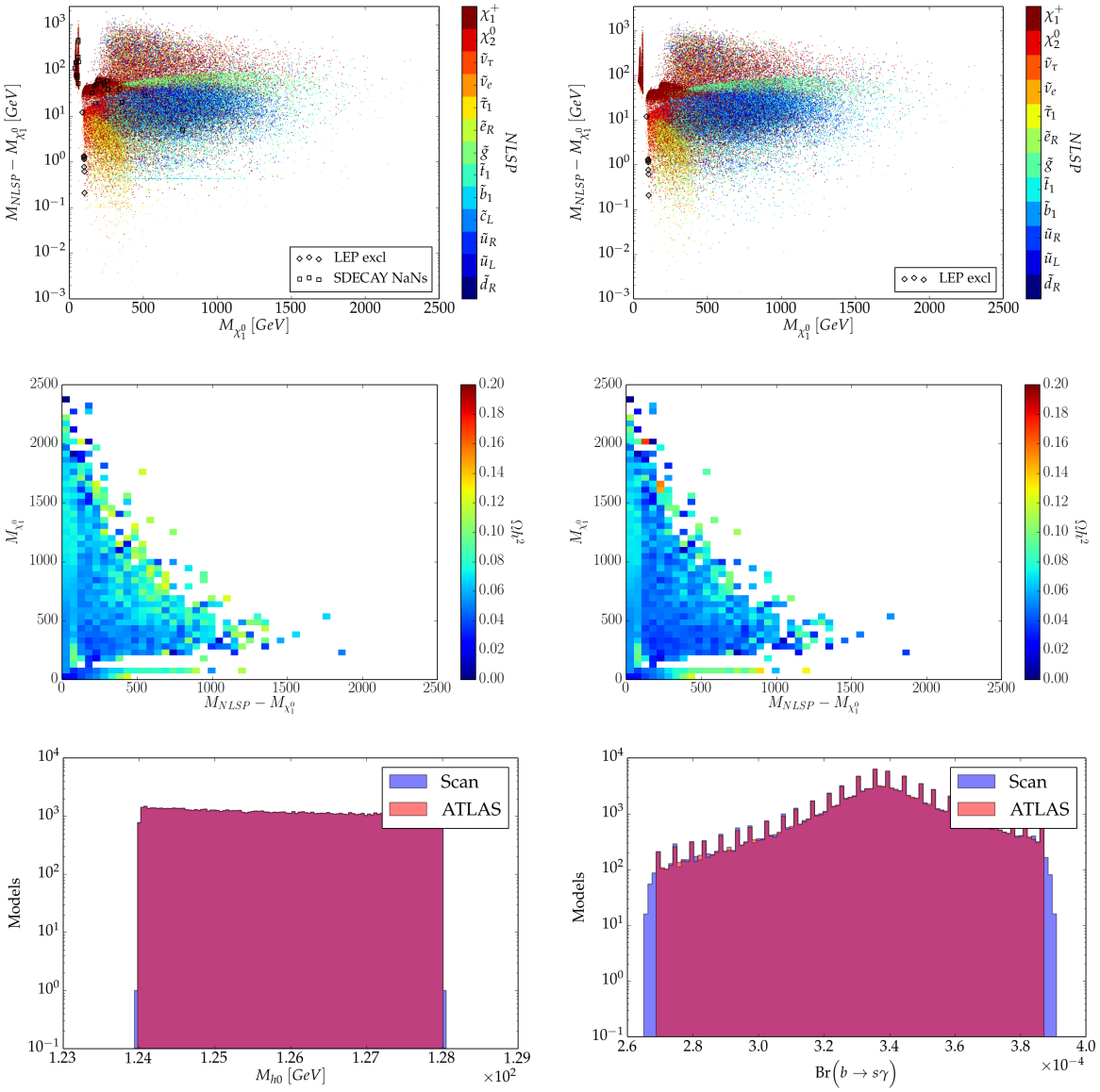

Figure 4.11: Comparison of between some important observables as computed by Rizzo et. al and the corresponding values found running our tool chain. Top: NLSP distribution as a function of the LSP mass and NLSP-LSP mass splitting. Middle: Mean relic density as a function of the same parameters. Bottom: Overlapping histograms showing the Higgs mass distribution (left) and branching fraction $Br(b \to s + \gamma)$ (right)

goals set out at the beginning of this section. The work needed to bring the package to a state where large scale scans over the pMSSM may be attempted should be fairly straight forward, and should not take too much time, given the project is continued.

Paper I

Finding Viable Models in SUSY Parameter Spaces with Signal Specific Discovery Potential

JHEP

Published for SISSA by Springer

Received: *January 9, 2013*
Revised: *June 28, 2013*
Accepted: *July 17, 2013*
Published: *August 20, 2013*

Finding viable models in SUSY parameter spaces with signal specific discovery potential

Thomas Burgess, Jan Øye Lindroos, Anna Lipniacka and Heidi Sandaker

Department of Physics and Technology, University of Bergen, Muséplassen 2, 5006 Bergen, Norway

E-mail: thomas.burgess@ift.uib.no, jan.lindroos@ift.uib.no, heidi.sandaker@ift.uib.no, anna.lipniacka@ift.uib.no

Abstract: Recent results from ATLAS giving a Higgs mass of 125.5 GeV, further constrain already highly constrained supersymmetric models such as pMSSM or CMSSM/mSUGRA. As a consequence, finding potentially discoverable and non-excluded regions of model parameter space is becoming increasingly difficult. Several groups have invested large effort in studying the consequences of Higgs mass bounds, upper limits on rare B-meson decays, and limits on relic dark matter density on constrained models, aiming at predicting superpartner masses, and establishing likelihood of SUSY models compared to that of the Standard Model vis-á-vis experimental data. In this paper a framework for efficient search for discoverable, non-excluded regions of different SUSY spaces giving specific experimental signature of interest is presented. The method employs an improved Markov Chain Monte Carlo (MCMC) scheme exploiting an iteratively updated likelihood function to guide search for viable models. Existing experimental and theoretical bounds as well as the LHC discovery potential are taken into account. This includes recent bounds on relic dark matter density, the Higgs sector and rare B-mesons decays. A clustering algorithm is applied to classify selected models according to expected phenomenology enabling automated choice of experimental benchmarks and regions to be used for optimizing searches. The aim is to provide experimentalist with a viable tool helping to target experimental signatures to search for, once a class of models of interest is established. As an example a search for viable CMSSM models with τ-lepton signatures observable with the 2012 LHC data set is presented. In the search 105209 unique models were probed. From these, ten reference benchmark points covering different ranges of phenomenological observables at the LHC were selected.

Keywords: Supersymmetry Phenomenology

ArXiv ePrint: 1210.7020

doi:10.1007/JHEP08(2013)098

JHEP08(2013)098

Contents

1 Introduction

Supersymmetry (SUSY) may alleviate many of the problems associated with the Standard Model of particle physics (SM) if the mass of the superpartners lies close to the TeV-scale [1, 2]. Furthermore, it provides a natural dark matter candidate in the form of the Lightest Supersymmetric Particle (LSP), if R-parity is conserved [3]. However, even the simplest SUSY extension of the SM, the so called Minimal Supersymmetric Standard Model (MSSM), introduces over 100 new free parameters making them very difficult to experimentally constrain. On the other hand a large part of the MSSM parameter space is already ruled out, as it would lead to unobserved phenomena like non-conservation of lepton numbers, flavour changing neutral currents or large CP violation [4]. It is therefore common practice to look at constrained models that assume a partial unification of parameters at some high energy scale and where the dynamics of the high energy theory ensures more viable phenomenologies [5]. The minimal SUper GRAvity model (mSUGRA) [6] is an example of such a constrained model where the SUSY parameters are assumed to unify at the GUT scale into five universal parameters, a common scalar mass m_0, a common gaugino mass $m_{1/2}$, the ratio between the SUSY Higgs vacuum expectation values $\tan\beta$, a common trilinear Higgs-sfermion coupling A_0, and the sign of the Higgsino mass parameter μ. In the "lighter" version of it, the so called constrained MSSM (CMSSM) [7–9], the gravitino mass is not forced to unify at the same scale as other gaugino masses. In NUHM (Non-Universal Higgs Masses) [10, 11] models, the Higgs boson masses do not unify with the sfermion masses to a common m_0.

JHEP08(2013)098

ATLAS and CMS experimental searches for SUSY usually present results only in two-dimensional slices of the parameter space of some simplified model assuming fixed values for other parameters [12, 13]. Due to complicated dependence of physical masses and thus experimental signatures on all the model parameters, it is easy to leave specific corners of the model space unexplored in such an approach, leaving out regions where experimental search may have large discovery potential. This has led several theoretical groups [14, 15] to reinterpret experimental searches in different regions of parameter space with help of simplified simulators of detector response like DELPHES [16] or PGS [17]. This approach can be relatively reliable for moderately simple experimental signatures involving jets and missing transverse energy ($\not{E}_T$), but it cannot be trusted for more difficult experimental objects like photons or tau leptons.

MCMC based parameter inference has been successfully employed to find the most viable region of the full parameter spaces, based on requirements that the models should be in accordance with recent experimental constraints [14, 15], including these on the Higgs boson mass and rare B-mesons decays. While such scans provide a more complete picture of the still allowed regions of parameter space they do not consider whether these parameter space regions are within experimental reach. This poses difficulties for experimentalists when trying to make direct use of the results.

In this paper, a MCMC-based framework for determining the part of non-excluded model parameter space where a given experimental signature can be observed is presented. By adding a signature specific discoverability parameter to the set of current experimental constraints, the interesting regions of the parameter space are found. Models from these regions are then partitioned according to phenomenology using a clustering algorithm to enable an automatized construction of reference points for optimizing experimental searches. This step distinguishes our approach from existing similar frameworks, for example [18]. The procedure is applicable to a wide range of signatures and models, and is intended as a tool for experimentalist to extend limits to more interesting regions of parameter space. It is important to note that we do not intend to find the true maximal likelihood regions, as the discoverability measure does not reflect any existing constraint. In order to provide a proof of concept, a concrete example defining a non-excluded part of CMSSM parameter space which could be discoverable with τ-leptons in the 2012 LHC data is outlined.

The paper is structured as follows: section 2 discusses the publicly available software tools used to calculate low energy CMSSM observables, scan and clustering algorithms, as well as the specific constraints and phenomenological parameters used. Section 3 describes the results of the scan and the phenomenological reference points constructed. Appendix A explains the details of the algorithm implementation and presents cross-checks of the effects of experimental constraints with other existing results. In section 4, a summary and comments on the procedure are provided.

2 Algorithms and tools

Experimental constraints on dark matter relic density Ωh^2 as well as on rare processes such as $B_s \to \mu\mu$ and $b \to s + \gamma$ set strict bounds on the parameter space of CMSSM (see for

JHEP08(2013)098

example [15]). Furthermore, the Higgs boson mass of 125.5 GeVas measured by ATLAS [19] is hard to accomodate in CMSSM, making the fraction of viable models within current experimental reach extremely small. This renders simple uniform scans highly inefficient. A rough random scan made to explore the parameter dependence in CMSSM, gave a fraction of 10^{-5} models in accordance with current experimental constraints. Therefore, more advanced techniques need to be employed to get a representative picture of the discoverable and non-excluded regions of parameter space in an efficient way.

The approach used in this paper is to employ a likelihood distribution P, that reflects how well models fit the data and their discovery potential, to perform a guided random walk through parameter space using Markov Chain Monte Carlo [20]. This increases the search efficiency as the parameter space is sampled according to the distribution P thus less time is spent sampling low likelihood regions. In this work an adaptive MCMC is implemented, where the likelihood map is based on the compatibility of low energy properties of CMSSM models with experimental and theoretical constraints, and discovery potential. These properties are calculated using several publicly available software tools.

2.1 Software tools

A series of publicly available software tools is used to calculate the low energy parameters needed to check experimental constraints on the SUSY models, and to construct the likelihood map used in the MCMC scan. Parameters are passed between the different tools using the SLHA-interface [21]. The tools are called in sequence starting with the least computationally costly, and after each step the likelihood is updated based on the available parameters. Each component (i) of the likelihood is constructed to have a maximal value of P_i=1 so that the likelihood always decreases as the chain progresses. This makes it possible to check for rejection after every step in the tool sequence, and enables early termination of the calculations for a large fraction of low likelihood models.

In the first step, `ISAJET` with `isaRED` [22] is used to run the GUT scale universal parameters down to the electroweak scale, calculate $\mathbf{Br}\,(B_s \to \mu\mu)$, and to check whether the models are allowed by several theoretical constraints, including requirements of a $\tilde{\chi}_1^0$ LSP and correct electroweak symmetry. In the next step, `FeynHiggs` [23] and `HiggsBounds` [24] are used to recalculate and check if the model fulfills experimental constraints on the Higgs sector. Afterward, the dark matter relic density, Ωh^2, and $\mathbf{Br}\,(b \to s + \gamma)$ is calculated using `darkSUSY` [25], which also checks against experimental constraints on sparticle masses from LEP $\Delta\rho$ and Z-width (see for example [26, 27]). Finally, 1000 pp signal events at $\sqrt{s} = 8$ TeV are generated using `Pythia` [28] in order to get a leading order estimate of the SUSY cross-section, $\sigma_{\rm LO}$, and to calculate the fraction of events $(\mathbf{Br}_\tau, \mathbf{Br}_{jet} \ldots)$ containing respectively at least one τ, e, μ, jet with pseudorapidity in the central part of the detector, $|\eta| < 2.5$, and sufficiently large momentum in the plane perpendicular to the beam axis, $p_T > 20$ GeV, and the average number of these objects per SUSY event $(n_\tau, n_{jet} \ldots)$. For each of these objects, the average p_T is calculated for the two with the highest transverse momentum. The average missing transverse energy per event, $\not{E}_T$, is also calculated.

The software tools and their employment are summarized in table 1.

JHEP08(2013)098

Tool	Information used
`ISAJET` 7.83 & `isaRED`	SUSY masses, $\mathbf{Br}\,(B_s \to \mu\mu)$
`FeynHiggs` 2.9.4 & `HiggsBounds` 3.8.1	Higgs sector
`darkSUSY` 5.1.1	$\Omega_\chi h^2$, $\mathbf{Br}\,(b \to s + \gamma)$
`Pythia` 8.175	$\sigma_{\rm LO}$,$\mathbf{Br}$, $\langle n, p_{T1}, p_{T2}\rangle$ for $\tau, e, \mu,$ jet,$\langle \not{E}_T\rangle$

Table 1. Software tools and resulting information employed in this work. Average values from `Pythia` are for final states objects with $|\eta| < 2.5$ and $p_T > 20$GeV.

2.2 Likelihood map and experimental constraints

The likelihood map P used to explore CMSSM parameter space is constructed by combining a likelihood $P_{\rm exp}$ based on experimental and theoretical constraints with an ad-hoc likelihood related to the expected number of events with tau leptons, P_τ. Here P_τ is based on the probability of producing observable τ-leptons with $21/fb$ of the LHC data collected in 2012. P_τ can be easily replaced by another likelihood function related to observability of any signal of interest. The likelihoods are normalized so that each individual contribution P_i has a maximal value $\max(P_i) = 1$. Thus, the full likelihood becomes:

$$P_{\rm tot} = P_{\rm exp} \cdot P_\tau \quad and \quad P_{\rm exp} = \prod_i P_i\,, \tag{2.1}$$

where P_i are the likelihoods related to experimental limits and theoretical constraints. Some of P_i are either 0 or 1 as specified in table 2. These include most of theoretical constraints, limits checked internally by the software tools used. For other experimentally measured quantities Gaussian errors are assumed and the resulting likelihoods are continuous. Gaussian distributions around the central experimental values are used for $\mathbf{Br}\,(b \to s + \gamma)$, $\mathbf{Br}\,(B_s \to \mu\mu)$, and the Higgs mass, while for the relic density a uniform distribution is chosen with a Gaussian tail above the best observational value. The latter accepts models with the relic density lower than the recent Planck result [29], allowing for other unknown sources except of CMSSM neutralinos to contribute to the relic density. The central values and standard deviations used are $\Omega h^2 = 0.1199 \pm 0.0027$ for the relic density [29], $\mathbf{Br}\,(b \to s + \gamma) = (3.55 \pm 0.42) \cdot 10^{-4}$ [30] for the charmless b-quark decay, with a theoretical uncertainty $\sigma_{th} = \pm 0.33 \cdot 10^{-4}$ [31], and $\mathbf{Br}\,(B_s \to \mu\mu) = (3.2 \pm 1.5) \cdot 10^{-9}$ [32]. For the Higgs mass, the combined ATLAS best fit from the $H \to \gamma\gamma, 4l$ channels is used [19], with a theoretical uncertainty $\sigma_{th} = \pm 1.5$GeV is assumed [33], giving $m_{h0} = (125.5 \pm 1.7)$ GeV. The experimental and theoretical constraints are summarized in table 2. The 2011 and 2012 ATLAS and CMS results of direct searches for SUSY in R-parity conserving channels are not included in the present work.The reason for it is two-fold. Firstly, the high Higgs mass translates in CMSSM into rather high sparticle masses, on the border of the present direct searches sensitivity. Secondly, our aim is to propose precise regions, where this sensitivity should be checked, and not to exclude them from our scans. Results obtained by ATLAS and CMS experimenters using dedicated detector response simulations to translate

JHEP08(2013)098

Constraints	**Likelihoods $\mathbf{P_i}$**	**Values**
$\tilde{\chi}_1^0$ LSP, Correct EWSB, No tachyons ...	OK: 1 Not OK: 0	`ISAJET` 7.81
Sparticle masses, $\Delta\rho$, Z-width	OK: 1 Not OK: 0	`darkSUSY` 5.0.5
OK Higgs sector	OK: 1 Not OK: 0	`HiggsBounds` 3.7.0
$\mathbf{Br}(B_s \to \mu\mu)$	$\exp\left[\frac{(\mathbf{Br}_{\mathrm{B_s}}-\mu_{\mathrm{B_s}})^2}{-2\sigma^2_{\mathrm{B_s}}}\right]$	$\left[\mu_{\mathrm{B_s}}, \sigma_{\mathrm{B_s}}\right] = \left[3.2, 1.5\right] \cdot 10^{-9}$
Ωh^2	$\exp\left[\frac{(\Omega h^2 - \min(\Omega h^2, \mu_\Omega))^2}{-2\sigma^2_\Omega}\right]$	$\left[\mu_\Omega, \sigma_\Omega\right] = \left[1.199, 0.027\right] \cdot 10^{-1}$
$\mathbf{Br}(b \to s + \gamma)$	$\exp\left[\frac{(\mathrm{Br}_{\mathrm{bsg}}-\mu_{\mathrm{bsg}})^2}{-2\sigma^2_{\mathrm{bsg}}}\right]$	$\left[\mu_{\mathrm{bsg}}, \sigma_{\mathrm{bsg}}\right] = \left[3.55, 0.42\right] \cdot 10^{-4}$
m_{h0}	$\exp\left[\frac{(m_{h0}-\mu_{h0})^2}{-2\sigma^2_{h0}}\right]$	$\left[\mu_{h0}, \sigma_{h0}\right] = \left[125.5, 1.7\right]$ GeV

Table 2. Experimental and theoretical constraints used and the associated likelihoods.

the present limits into other regions of parameter space should be more reliable than ones employing only approximate modelling of detectors response. We thus prefer to use this opportunity to provide tools to experimenters so that they can choose somewhat more interesting regions of SUSY parameter space to present their results.

The discoverability likelihood P_τ is chosen as a Poissonian *discoverability* measure constructed from the sum of likelihoods for observing a given number of tau events, $N_\tau \geq 1$, given the expected number of events containing at least one τ, $\langle N_\tau \rangle = \mathbf{Br}_\tau \cdot \mathcal{L} \cdot \sigma_{LO}$.

$$P_\tau = \sum_{N_\tau = N_\tau^{\min}} P(N_\tau | \langle N_\tau \rangle) \quad , \quad P(N_\tau | \langle N_\tau \rangle) = \frac{\langle N_\tau \rangle^{N_\tau} \exp\left[- \langle N_\tau \rangle \right]}{N_\tau !} \, . \tag{2.2}$$

Leading order SUSY cross-section σ_{LO} in pp collisions at 8 TeV center-of-mass energy, luminosity of $21/fb$ and the fraction of events containing at least one τ, $\mathbf{Br}_\tau$, as found from `Pythia`, are used to calculate $\langle N_\tau \rangle$ above.

Experimental selection in search of specific signal has broadely speaking two steps.

The first step ensures that a specific experimental signature characterizing the signal is observed in the detector. In our case this signature consists of taus, jets and missing transverse energy. In order for this step to be fulfilled one needs to make sure that these experimental objects are within fiducial volume of the detector and have transverse momentum above a given threshold. The number of signal events passing this first step can be predicted with relatively good accuracy without using any sophisticated detector description.

In the second step of the selection, specific cuts in order to reject the backgrounds are performed, and some measure of sensitivity is used in order to optimize bakground rejection while keeping as much of the signal as possible. The number of expected signal events after such a selection can vary orders of magnitude depending on specific strategy chosen.

One example of this is the ATLAS τ search as presented in [34], where two different strategies are considered, one for events where exactly 1 τ is selected and another for events with 2 or more τ leptons. This difference in selection strategy gives large differences in signal selection efficiency. It is clear that precise choice of strategy needs to be done with precise tools using reliable detector simulation, background estimation and cutflow optimization, and this can be done only withing experimental collaborations.

JHEP08(2013)098

Parameter	Range
m_0	[60,3000] GeV
$m_{1/2}$	[60,3000] GeV
A_0	[-5000,5000] GeV
$\tan\beta$	[2,60]
sign(μ)	+1

Table 3. Search ranges used for the CMSSM MCMC scans.

The aim of the scan presented here however is to find interesting regions for τ searches in which this second step of the selection can be performed, because there is enough events passing the first step.

This is why the constructed measure P_τ is based on the number of τ events observable in the detector rather then a more precise estimate valid for a specific analysis strategy. The main uncertainty in P_τ comes from neglecting NLO corrections to the cross section and theoretical uncertainties in the LO cross section. The NLO corrections for CMSSM can be relatively large, with k-factors of the order of 3 [35].

The LO cross section uncertainty estimate is sensitive to variations in renormalisation/factorization scale, parton distribution function and the strong coupling α_s, and can lead to uncertainties of order 100%, compared to $\sim$ 20% at NLO [36]. In comparison Pythia MC uncertainties are negligible with relative errors of order $\sigma_{MC} \lesssim 0.1$ for reasonable branching fractions $\mathbf{Br}_\tau \gtrsim 0.1$. The combined uncertainty in P_τ is also much smaller than the uncertainty associated with experimental selection.

Including NLO calculations for each point increases computational time by a factor of five or more, and given the uncertainties related to experimental selection outlined above, the computational gain outweighs the loss in precision. As our ambition is merely to identify which regions of mSUGRA parameter space are more interesting than others, NLO corrections matter only if they vary a lot across the parameter space. The option for including Prospino NLO calculations [37] is implemented in the package, and is used to get more precise estimates for the proposed benchmark points. Indeed the corrections are quite comparable across proposed the benchmark points.

The search range in CMSSM parameter space follows the suggestion in [38]. The ranges for m_0, $m_{1/2}$, A_0 and $\tan\beta$ are presented in table 3. The anomalous muon magnetic moment, $\delta a_\mu = a_\mu^{\rm exp} - a_\mu^{\rm SM}$, is not taken into account in this scan, other than as a reason for choosing sign(μ) > 0, which is required to give positive SUSY contributions. This is because the value of δa_μ is generally incompatible with other constraints [15], leading to maximal likelihood regions in agreement with neither. In addition the actual value of δa_μ seems to be open for debate due to uncertainties in both LO and NLO hadronic contributions to $a_\mu^{\rm SM}$ [15, 39]

A fixed value for $m_{\rm top} = 173\,\text{GeV}$ was taken.

The lower bounds on the universal masses and on $\tan\beta$ in table 3 stem from LEP [27, 40] bounds, while the upper limits are chosen on the basis of naturalness for the masses m_0 and $m_{1/2}$ and perturbativity of the Yukawa couplings for $\tan\beta$. The range for the

JHEP08(2013)098

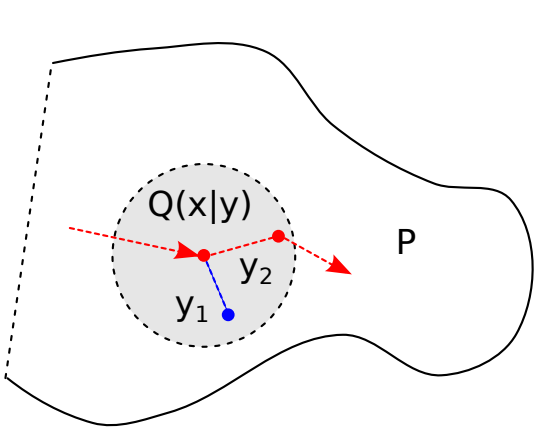

(a) a) A proposal distribution $Q(\mathbf{y}|\mathbf{x})$ used to sample new points $(\mathbf{y_1}, \mathbf{y_2})$ from a point $\mathbf{x}$. These points are either accepted $(\mathbf{y_2})$ or rejected $(\mathbf{y_1})$ depending on the ratio between the underlying likelihood P and Q as given by α (2.3)

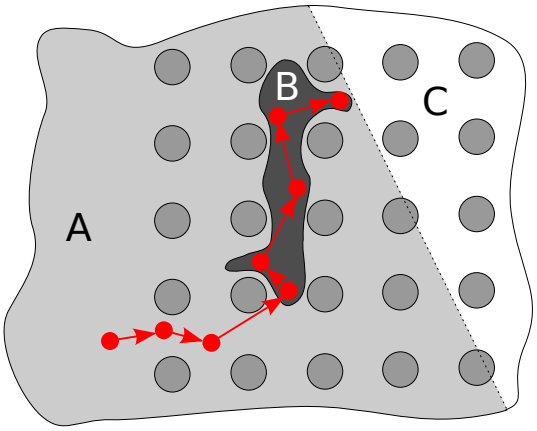

(b) b) Example MCMC random walk finding narrow high likelihood regions (B), when starting from a point in a low (A) or zero (C) likelihood region. The grid of dots is shown to illustrate how such regions can be missed by uniform grid-based scans.

Figure 1. Illustrations of the standard MCMC sampling method, 1(a), and a typical MCMC random walk, 1(b).

trilinear coupling A_0 is extended compared to [38], since the Higgs mass has a quadratic dependence on A_0 [41] allowing for higher m_{h0} at large values of $|A_0|$.

It is important to note that the more realistic the likelihood, the more computationally efficient is the search for interesting models. However, the set of models found does not depend on fine details of the likelihood function used, as we accept points in a range of likelihood. Our goal is to find a set of interesting models fulfilling latest experimental constraints, in order to guide further experimental searches. We do not intend to make any *statistically quantified decision* on which of the selected models are more likely than others.

2.3 MCMC algorithm

The MCMC method used here is a Metropolis-Hastings algorithm [42] where, given a point $\mathbf{x} = \{x_1, x_2 \dots x_D\}$ in a D-dimensional parameter space, a proposal distribution, $Q(\mathbf{y}|\mathbf{x})$, is used to sample a new point $\mathbf{y}$. The proposal distribution is related to the likelihood P of the new point $\mathbf{y}$ being "interesting" from the point of view of requirements described in section 2.2. The new point is accepted randomly with a probability given by

$$\alpha(\mathbf{y}|\mathbf{x}) = \min\left(1, \frac{P(\mathbf{y})Q(\mathbf{x}|\mathbf{y})}{P(\mathbf{x})Q(\mathbf{y}|\mathbf{x})}\right), \tag{2.3}$$

If $\mathbf{y}$ is accepted, it is added to the chain and the next point is sampled starting from $\mathbf{y}$. If it is not accepted, the chain remains at $\mathbf{x}$ and the process is repeated as illustrated in figure 1. The asymptotic distribution of likelihoods calculated for the resulting chain of points is the desired likelihood distribution P.

In order to efficiently map possible high likelihood regions of the parameter space which are separated by large regions of low likelihood a regional adaptive MCMC algorithm

JHEP08(2013)098

similar to [43] has been implemented. The algorithm approximates the target likelihood distribution P as a mixture of normalized multivariate Gaussian distributions and uses this approximation as a basis for a proposal $Q(y|x)$, as explained in the following section 2.3.1. This proposal is used to guide multiple MCMC search chains in parallel and it is iteratively updated according to the resulting selected sample of points.

2.3.1 Adaptive multi chain Monte Carlo

An initial estimate for the proposal was constructed by uniformly sampling the space such that all separated regions where the likelihood P is high are covered. The idea is similar to the bank sampling introduced in [44], where prior knowledge about the local maxima of the likelihood distribution is incorporated into the proposal to increase efficiency of sampling the distributions where these maxima are separated by large regions of low likelihood. The points of CMSSM parameter space chosen for the initial sample were required to pass all discrete cuts and to give experimentally measured physical variables within a reasonable range of the experimentally preferred values, see table 2 for details. Sampled points in CMSSM parameter space were weighted according to their likelihood and clustered using *k-means* algorithm, to be defined in 2.4. The "shape" of each cluster was estimated by calculating the weighted mean $\boldsymbol{\mu}$ vector and covariance matrix $\boldsymbol{\Sigma}$. The number of clusters corresponded to the number of normalized Gaussian distributions (normal mixture) that was to be used to approximate the likelihood distribution P, as explained below.

A small fraction of large jumps [38, 43, 45] was added to the standard small jumps illustrated in figure 1(a) in order to increase sampling efficiency. To achieve this a global proposal term $q_G(\mathbf{y})$, was added to the standard local one, $q_L(\mathbf{y}|\mathbf{x})$, giving the full proposal distribution:

$$Q(\mathbf{y}|\mathbf{x}) = \beta q_L(\mathbf{y}|\mathbf{x}) + (1-\beta) q_G(\mathbf{y})\,, \tag{2.4}$$

Here β is a mixing parameter relating the global and the local proposal terms, explained further.

The global proposal $q_G(\mathbf{y})$ was taken as a set of m multivariate normal distributions, $\mathcal{N}$, as in [46]. The set was large enough to describe the main features of the target likelihood. Each multivariate distribution was multiplied by a weight factor w_i, defined in the formula below.

$$\begin{aligned} q_G(\mathbf{y}) &= \sum_{i=1}^{m} w_i \mathcal{N}(\mathbf{y}|\boldsymbol{\mu}_i, \boldsymbol{\Sigma}_{G,i}) \\ ,\mathcal{N}(\mathbf{y}|\boldsymbol{\mu}, \boldsymbol{\Sigma}) &= \frac{\exp\left[-\frac{1}{2}(\mathbf{y}-\boldsymbol{\mu})^{\mathrm{T}}\boldsymbol{\Sigma}^{-1}(\mathbf{y}-\boldsymbol{\mu})\right]}{\sqrt{(2\pi)^D\,|\boldsymbol{\Sigma}|}}\,, \\ w_i &= \frac{\sum_{\mathbf{x}_i} P(\mathbf{x}_i)}{\sum_{\mathbf{x}} P(\mathbf{x})} \end{aligned} \tag{2.5}$$

Each weight factor was estimated by summing up the total likelihood over CMSSM parameter space points in a cluster i. Here $\boldsymbol{\mu}_i$ is the vector of the means of the i'th normal distribution, while $\boldsymbol{\Sigma}_{G,i}$ is the covariance matrix of the i'th component of the mixture. The local proposal $q_L(\mathbf{y}|\mathbf{x})$ was taken as a normal distribution with mean, $\mathbf{x}$,

JHEP08(2013)098

and the covariance, $\mathbf{\Sigma}_{L,i}$, characterizing the closest cluster in the parameter space. An euclidean distance measure was used and each parameter was scaled so that the search ranges defined in table 3 varied from 0 to 1. The local proposal covariance was chosen so that: $\mathbf{\Sigma}_{L,i} = \alpha_i \mathbf{\Sigma}_{G,i}\,,\ i \in \{1, 2, \ldots m\}$, where α_i was a parameter adapted such that the local acceptance rate for points in the parameter space region within the cluster i was between 0.05 and 0.15. The rather low acceptance rate was chosen because the hierarchical nature of the likelihood calculation yields higher computational speed for low acceptance rates. Thus our optimal acceptance rate is probably lower than that of 0.23 found in [47]. The acceptance probability for stepping from a given point x to a new point y was then given as:

$$\alpha(\mathbf{y}|\mathbf{x}) = \min\left(1, \frac{P(\mathbf{y})\left[\beta q_L(\mathbf{x}|\mathbf{y}) + (1-\beta) q_G(\mathbf{x})\right]}{P(\mathbf{x})\left[\beta q_L(\mathbf{y}|\mathbf{x}) + (1-\beta) q_G(\mathbf{y})\right]}\right). \tag{2.6}$$

The search chains were started from random CMSSM parameter space points in the weighted sample and followed independently. After a given number of steps data were re-clustered and the proposals were updated, taking into account the new sampled parameter space points, where the new points were weighted according to the estimated likelihood. A certain likelihood threshold $P_{\min}$ was required for the first relevant point in each chain, since we are interested in high likehood regions. The implementation details are described in the appendix A.

2.4 Clustering algorithm

A modified *k-means* [48] algorithm, to be defined below, has been devised in order to cluster likelihood-weighted points. The role of clustering is two-fold. Firstly clusters in CMSSM parameter space were needed to calculate the approximate Gaussian distributions used in the proposal described in section 2.3.1. Secondly, sets of high-likelihood model-points in CMSSM parameter space were clustered according to the different experimental signatures they were expected to exhibit in the detectors at the LHC.

The *k-means* algorithm defines clusters in the parameter space by assigning each point to the closest centroid, (C). The algorithm was initialized by choosing at random k points in the parameter space as cluster centers, C. Next, each C_i was refined as the average of the points near to it and points were reassigned to the new C, and the procedure was repeated until it converged to a set of stable Cs. To increase the speed of the algorithm, a maximum number of iterations and a minimum improvement between iterations was set for the centroids positions refinement.

In order to define a closest centroid, a distance measure is required. An euclidean distance measure in CMSSM space was employed, scaling each parameter such that the search ranges defined in table 3 varied from 0 to 1. Using another distance measure (for example a log scale) only alters the proposal distribution and thus only affects the efficiency of the algorithm, not the results. The *k-means* algorithm, described above, with predetermined number of clusters was used to cluster points in CMSSM space.

In order to define reference points in phenomenological space the arbitrary choice of the number of such points has to be avoided. To this end *k-means* formed the basis for a *g-means* algorithm, with which the number of clusters was determined automatically, as

JHEP08(2013)098

explained further. In both instances the random first guess of cluster centers (centroids) positions was improved as suggested in [49], (k-means++ algorithm). In this method probability of picking a new point as a cluster center was weighted by the square distance to the closest already picked point. This guess reduced as well the average number of iterations to achieve convergence.

To determine the number of clusters k in the space of phenomenological observables, a *g-means*-algorithm [50] was employed. It started with applying *k-means* for $k = 2$, thus dividing the parameter space into two sub-clusters. Then a statistical test to verify if the likelihood distributions of both clusters could be described by a single Gaussian was performed. For each phenomenological observable, x_i, the standard deviation, σ_i, and the mean, $\bar{x_i}$, were calculated and each observable transformed $x_i' = (x_i - \bar{x_i})/\sigma_i$ to facilitate defining the distance for clustering purposes. If the test rejected the single Gaussian distribution hypothesis, the procedure was repeated recursively for each of the new clusters, otherwise recursion was terminated. The statistical test was performed by means of the one dimensional Anderson-Darling normality measure [51]. The distances between the points and a plane that separated clusters and was perpendicular to the vector between the two centroids were subjected to the measure above. As the clustering could be sensitive both to outliers and to the random positioning of initial centroids, the whole splitting procedure was iterated n_{avg} times and the average number of clusters $\langle k \rangle$ was noted. Next, the clustering outcome with k closest to $\langle k \rangle$ was picked. If there were several clustering outcomes giving the same number of clusters k, one of these was picked at random. In the final step the obtained centroids were subjected to the *k-means* clustering one more time to ensure that a stable configuration has been found.

3 CMSSM with τ signatures

3.1 Results

All viable models found have large negative values of A_0 in common, but otherwise span a relatively large range of sparticle masses and values of $\tan\beta$. The ranges for the mean $\not{E}_T$ and p_T for leading jet and τ are shown in the CMSSM mass planes $m_0 - m_{1/2}$ and $A_0 - \tan\beta$ in figure 2 and two dimensional likelihood distributions are shown in figure 3. The distributions are constructed by binning the models into $N_{\text{bins}} = 50$ bins along each dimension, where the likelihood of each bin is approximated by the number of models contained. The effects of different constraints separately are discussed in the appendix A.

The *discoverability* likelihood constrains the SUSY τ production cross-section to not be too small. This sets upper bounds on how large the gaugino and scalar masses can be since the production cross-section falls sharply as the masses of colored sparticles grow. The cross-section has as well a slight A_0 dependence which allows for higher masses at higher negative values of A_0.

3.2 Phenomenology and reference points

The relatively wide range of values for SUSY masses and values of $\tan\beta$ found leads to a wide range of values of phenomenological properties such as average $\not{E}_T$,the average missing

JHEP08(2013)098

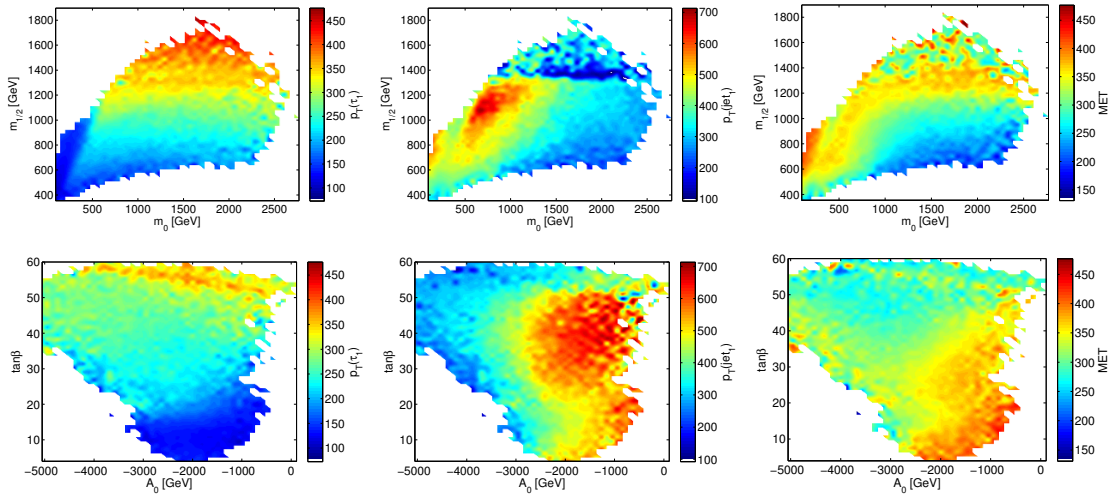

(a) $p_T(\tau_1)$ (b) $p_T(jet_1)$ (c) $\not{E}_T$

Figure 2. Average value per bin for mean $\not{E}_T$ and p_T for leading jet and τ shown in the CMSSM mass plane $m_0 - m_{1/2}$ (above) and $A_0 - \tan\beta$ plane (below).

min	**bf**	max	min	**bf**	max	min	**bf**	max	min	**bf**	max
$\mathbf{m_0}$ **[GeV]**			$\mathbf{m_{1/2}}$**[GeV]**			$\mathbf{A_0}$ **[GeV]**			$\tan\beta$		
123.7	**448.8**	2739	371.3	**961.1**	1881	−4998	**−2673**	52.75	4.598	**15.80**	59.44
$\mathbf{\Omega h^2}$			$\mathbf{m_{h0}}$**[GeV]**			$\langle \mathbf{N}_\tau \rangle$			$\mathbf{Br_{B_s\to\mu\mu}}$ $\mathbf{[10^{-9}]}$		
0.01	**0.1164**	0.1296	119.2	**125**	126.2	0.01	**10.64**	6784	3.840	**3.907**	8.494

Table 4. The range and best fit value for CMSSM parameters, relic density, m_{h0}, expected number of events with taus, $\langle N_\tau \rangle$ and $\mathbf{Br}_{B_s\to\mu\mu}$.

energy per SUSY event, $p_T(\tau_1)$, $p_T(\text{jet}_1)$, the average p_T of the leading τ and the leading jet see figure 2, and n_τ, n_{jet}, the average number of τ's/jets per SUSY event, see figure 4.

The p_T values for the leading jet and τ lepton obviously tend to be higher for high sparticle masses, since higher masses in CMSSM lead to higher mass splittings between the sfermions and the LSP. The p_Ts also become larger with A_0 closer to 0 and for high $\tan\beta$ values. The missing energy on the other hand tends to become larger at smaller scalar masses and increasing gaugino mass. The increase in $\not{E}_T$ with $m_{1/2}$ is likely due to increasing neutralino mass. These dependencies are illustrated in figure 2.

The average number of τs per SUSY events is mostly due to the branching fraction into τs as it can be seen comparing figure 4 and 5. One tau with high p_T per event is produced on average. The SUSY branching fraction to τs is largest at low values of $\tan\beta$ and m_0. At least one high p_t jet is expected in almost every event. The average numbers of jets increases with m_0, $\tan\beta$ and $|A_0|$.

In order to construct reference benchmark models that cover these different phenomenological properties the sample was clustered according to the phenomenological observables: $\not{E}_T$, n_{jet}, $p_T(\text{jet}_1)$, n_τ, $p_T(\tau_1)$, details are described in the appendix A.

JHEP08(2013)098

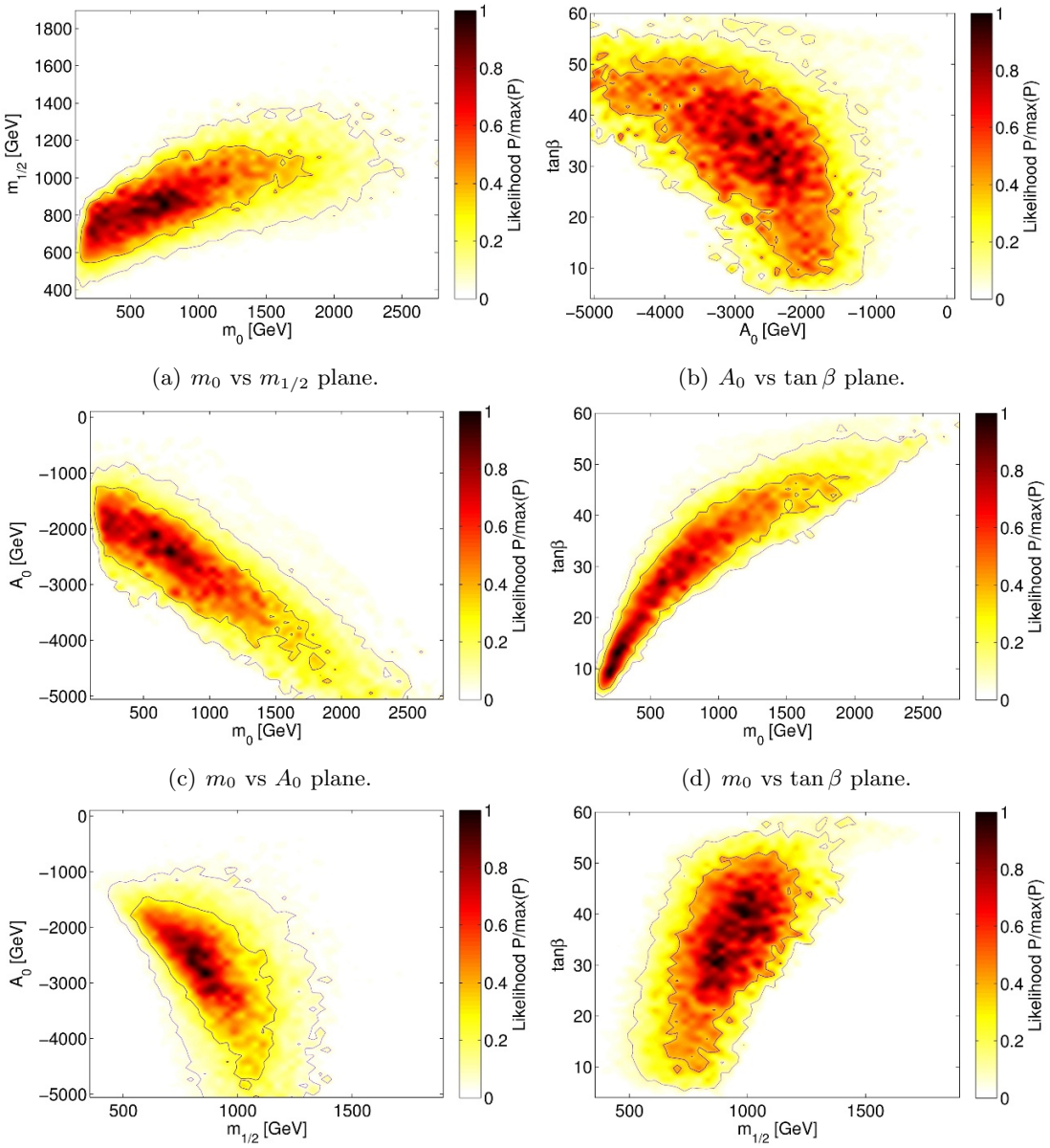

(a) m_0 vs $m_{1/2}$ plane.

(b) A_0 vs $\tan\beta$ plane.

(c) m_0 vs A_0 plane.

(d) m_0 vs $\tan\beta$ plane.

(e) m_0 vs A_0 plane.

(f) $m_{1/2}$ vs $\tan\beta$ plane.

Figure 3. Marginalized likelihood maps for different planes in CMSSM space.

With these, ten phenomenological clusters shown in table 5 were found. The SUSY and model related parameters for these clusters are shown in table 6 and 7. The centroids of the clusters can be regarded as reference (benchmark) points. additional k-factors were calculated for these benchmark points to give a more precise estimate for the expected number of τ's. As it can be seen in table 6, NLO corrections are small ranging from 1.1 to 1.7, and around 125 events with high energetic taus in the central part of the detector are expected for the highest cross-section reference points, which might be enough to detect the signal using the $21/fb$ of data gathered in 2012. Exploration of the other reference points might have to wait until the LHC 13 TeV operations.

JHEP08(2013)098

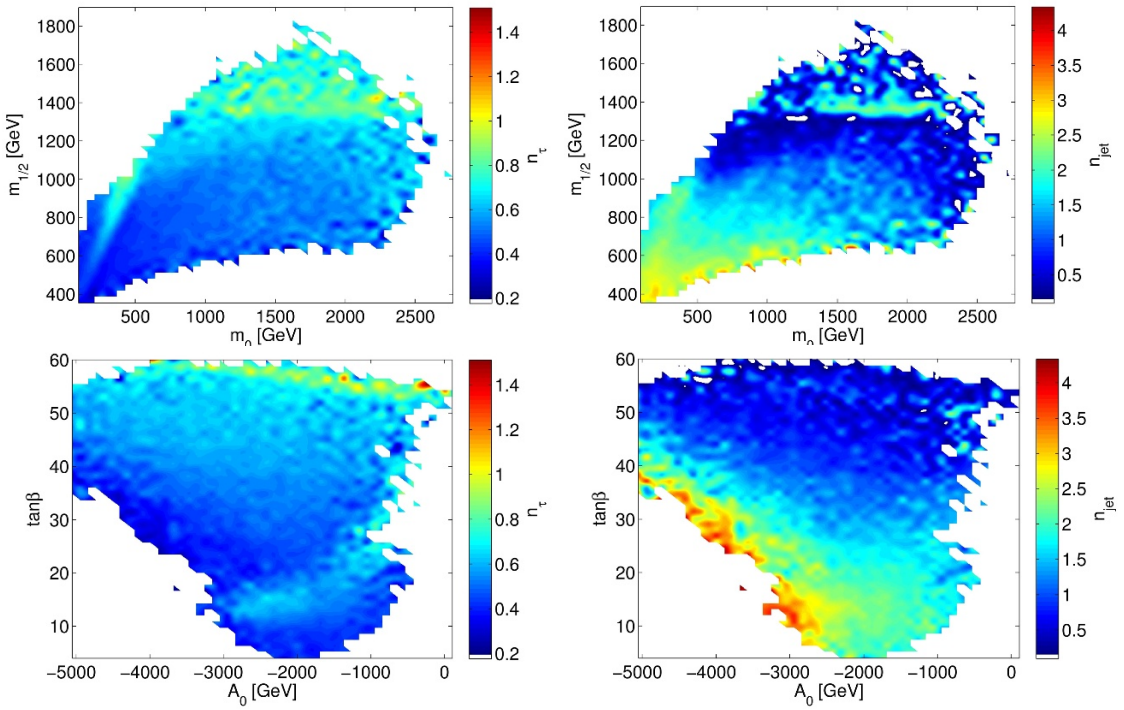

(a) Mean number of τs per SUSY event, n_τ

(b) Mean number of jets per SUSY event, n_{jet}

Figure 4. Average value per bin for the mean number of τs and jets per SUSY event shown in the $m_0 - m_{1/2}$ plane (above) and $A_0 - \tan\beta$ plane (below).

Various graphical projections of the clusters are shown in figures 6 and 7. It is clear from figures 7 that one finds viable models lying in the tails of clusters, far away from centroid positions. These models exhibit either low jet activity in the central part of the detector, but produce high p_t tau leptons, or have low number of high p_t jets (monojets) and low momentum taus. We have not investigated these models further yet, but it is clear that standard LHC SUSY searches assuming presence of high p_t jets for triggering purpose might fail for such models.

We have investigated decay branching fractions of the lightest Higgs boson to $\gamma\gamma$, ZZ, WW, $\tau\tau$ and $\mu\mu$ for the ten reference points, compared to these of the SM Higgs of the same mass. These branching fractions are typically somewhat higher, alas they do not differ by more than 5% from the SM values.

4 Conclusions

This work presents a new method for finding and classifying SUSY models that can be potentially discovered in an accelerator experiment, here LHC experiments. The method uses an adaptive MCMC algorithm to find interesting models and uses a clustering algorithm to classify the models according to phenomenology. The likelihood map is constructed using an extendible tool chain that incorporates recent limits from multiple sources through the SLHA interface. As the method employs the SLHA interface to communicate between

JHEP08(2013)098

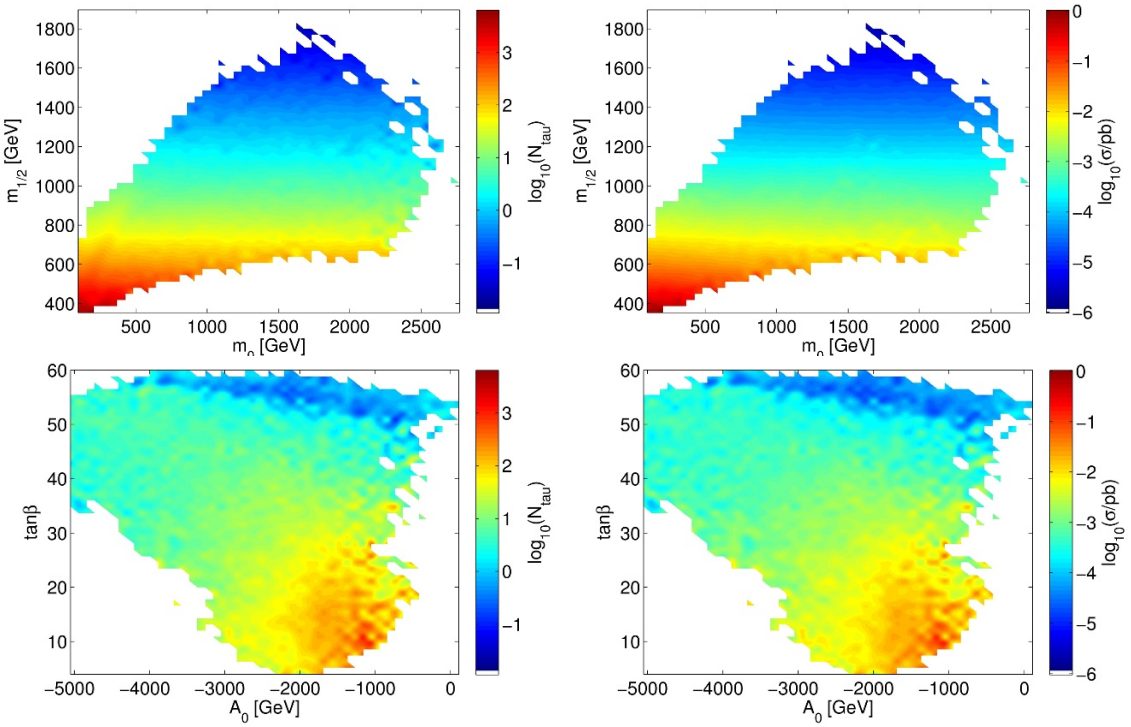

(a) Expected number of τ events with $\int \mathcal{L}dt = 21\, fb^{-1}$

(b) SUSY cross section

Figure 5. Average value per bin for expected number of τ events and SUSY cross-section in the mass plane $m_0 - m_{1/2}$ (above) and $A_0 - \tan\beta$ (below).

id	n	$\not{E}_T$ [GeV]			n_{jet}			$\text{jet}_1(p_T)$ [GeV]			n_τ			$\tau_1(p_T)$ [GeV]		
		min	cent	max	min	cent	max	min	cent	max	min	cent	max	min	cent	max
1	16811	266.7	**323.9**	439.9	1.5	**2.7**	3.8	206.4	**285.7**	487.4	0.1	**0.3**	0.5	48.3	**164.1**	274.2
2	6905	167.1	**273.9**	332.5	0.1	**1.7**	2.8	31.1	**317.8**	487.8	0.2	**0.5**	0.8	121.8	**225.9**	303.2
3	6830	67.3	**252.8**	316.0	1.1	**3.1**	4.4	56.9	**238.8**	344.1	0.1	**0.3**	0.6	55.2	**152.9**	239.8
4	11881	290.6	**383.1**	467.2	0.9	**2.1**	3.1	316.1	**493.1**	666.5	0.2	**0.6**	1.0	66.5	**132.5**	208.6
5	9786	285.7	**339.4**	451.8	0.8	**1.7**	3.0	243.9	**432.5**	556.4	0.2	**0.4**	0.7	146.2	**225.0**	316.5
6	10255	111.0	**267.4**	331.1	0.0	**0.5**	1.5	376.5	**561.4**	821.5	0.5	**0.6**	1.5	131.9	**266.1**	367.1
7	11653	279.1	**339.9**	389.1	0.0	**0.5**	1.2	473.8	**632.7**	1127.0	0.5	**0.6**	1.1	191.9	**280.9**	367.3
8	10744	300.9	**365.2**	456.6	0.7	**1.2**	2.0	446.2	**591.4**	728.2	0.2	**0.5**	0.8	121.1	**234.7**	298.5
9	8999	259.9	**338.0**	477.2	0.0	**0.5**	2.5	0.0	**361.4**	534.5	0.5	**0.6**	1.2	221.9	**307.7**	476.2
10	11345	0.4	**228.3**	302.6	0.0	**0.4**	2.7	151.3	**356.2**	577.5	0.5	**0.7**	2.0	56.4	**273.8**	385.6

Table 5. Phenomenological parameters of clusters found. The first two columns are the cluster index, id, (matches id in table 6) and number of model-points in the cluster, n. For each parameter the cluster centroid value, cent, is listed along with the minimum, min, and maximum, max, for the cluster. Centroid values can be regarded as reference values characterizing given experimental phenomenology.

JHEP08(2013)098

id	m_0 [GeV]	$m_{1/2}$ [GeV]	A_0 [GeV]	$\tan\beta$	$\langle N_\tau \rangle_{LO}$	$\langle N_\tau \rangle_{NLO}$	$\ln P$	Ωh^2	σ_{LO} [fb]	k_{NLO}
1	821.7	937.4	-2995.0	28.4	3.6	4.9	-1.0	0.1	0.8	1.33
2	1150.0	854.5	-3318.0	37.2	19.7	28.2	-1.5	0.1	2.0	1.43
3	678.4	747.7	-2807.0	25.7	76.5	125.5	-1.9	0.1	14.1	1.64
4	278.0	740.4	-1974.0	12.3	64.1	85.9	-1.3	0.1	7.1	1.34
5	669.4	814.6	-2685.0	25.8	29.9	43.1	-1.1	0.1	3.5	1.44
6	1045.0	961.4	-2774.0	37.9	7.5	8.7	-1.2	0.1	0.6	1.16
7	749.6	986.2	-2450.0	29.7	6.6	7.6	-1.1	0.1	0.5	1.15
8	481.5	824.0	-2149.0	21.5	26.4	33.5	-1.1	0.1	2.6	1.27
9	1483.0	1070.0	-3806.0	41.0	3.5	4.1	-1.1	0.1	0.3	1.17
10	1813.0	985.9	-4153.0	46.5	6.6	7.7	-1.5	0.1	0.5	1.17

Table 6. CMSSM parameters, relict density, 8 TeV CMS LHC production *LO* cross-section, total NLO k-factors and the number of expected events with τ leptons for the centroids of clusters. All models have sign$\mu > 0$ and $m_{\rm top} = 173$ GeV.

id	m_{h_0} [GeV]	$m_{\tilde{t}_1}$ [GeV]	$m_{\tilde{g}}$ [GeV]	$m_{\chi_1^0}$ [GeV]	$m_{\tilde{\tau}_1}$ [GeV]
1	125.3	997.4	2082	404.4	406.9
2	125.3	874.2	1932	369.7	375.8
3	124	628.5	1690	319.6	323.5
4	123.7	828.3	1658	313.5	314.6
5	125	824.3	1827	348.8	354
6	124.5	1201	2143	416	421.5
7	124.3	1229	2177	424.9	425.3
8	124.2	969.2	1837	351.6	353.1
9	125.6	1246	2384	467.9	469
10	125.6	1185	2233	432.8	437.8

Table 7. Higgs and sparticles masses for the centroids of clusters.

the different tools, it is easily be extendible to other parameter spaces and experimental signatures. For example one can look for interesting regions of GMSB for a two lepton analyses. This amounts to creating a steering file and specify the model, the parameter range of interest, the event topologies counted by `Pythia` and what constraints to take into account, f.ex count `Pythia` events containing $\ell = e, \mu$, and constrain on $\langle N_{2\ell} \rangle$. At the moment the actual code is only restricted by limitations to external software tools such as isasugra (allowed parameter spaces) and DarkSUSY (regions with neutralino LSP). In addition the code includes options for doing gridded or uniform random scans in addition to MCMC based methods. The plan is to make the code publicly available in the near future including more parameter spaces and different LSP.

As an example and test of the method the highly constrained CMSSM parameter space has been searched for models that could potentially be discovered using 2012 LHC with τ-lepton based signatures.

JHEP08(2013)098

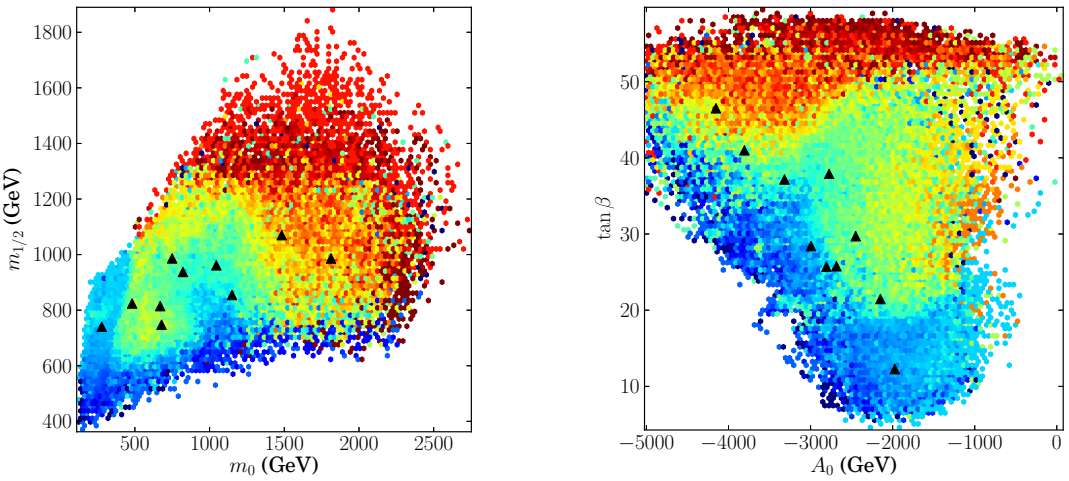

(a) m_0 vs $m_{1/2}$ projection.

(b) A_0 vs $\tan\beta$ projection.

Figure 6. Projections of clusters. Colors indicate to which cluster a given model belongs.

Although simplified models like CMSSM are severely constrained, we are still able to find regions fulfilling recent LHC bounds on Higgs mass and rare B-meson decays, and giving relic density in agreement with WMAP results. All models we found have Higgs BR very close to those of SM. Thus if two sigma excess of Higgs to gamma gamma BR appears to be real then CMSSM is clearly disfavored as observed by [52]. Ten reference (bench-mark) points exhibiting different phenomenologies were found with use of a *g-means* clustering algorithm. These reference points can be used to optimize searches. This makes the method very attractive from an experimental point of view, and applying the method to other models and different signatures would be a natural extension of this work. In fact the region found in this search is already part of an effort within the ATLAS astroparticle forum to provide additional model grids taking into account constraints from astro- and astroparticle physics.

The method has proven successful in finding and classifying SUSY models, but could still benefit from several extensions and improvements. More constraints could be added to the likelihoods and more advanced statistical analysis of the simulated data could be incorporated. Another interesting prospect would be to include detector simulations using PGS [17] or DELPHES [16] to get somewhat more realistic estimates for the expected signal, although we are skeptical about realism of such simulations. The MCMC algorithm constructed could still benefit from improvements to increase stability and efficiency, in addition to rigorous numerical testing. Finally a better distance measure for the clustering could allow for precise predictions of expected discovery potential.

On the more experimental side we find some viable models lying in the tails of clusters formed based of phenomenological observables. These models exhibit either low jet activity in the central part of the detector, but produce high p_t tau leptons, or have low number of high p_t jets (monojets) and low momentum taus. We have not investigated these models further yet, but it is clear that standard LHC SUSY searches assuming presence of high p_t jets for triggering purpose might fail for such models.

JHEP08(2013)098

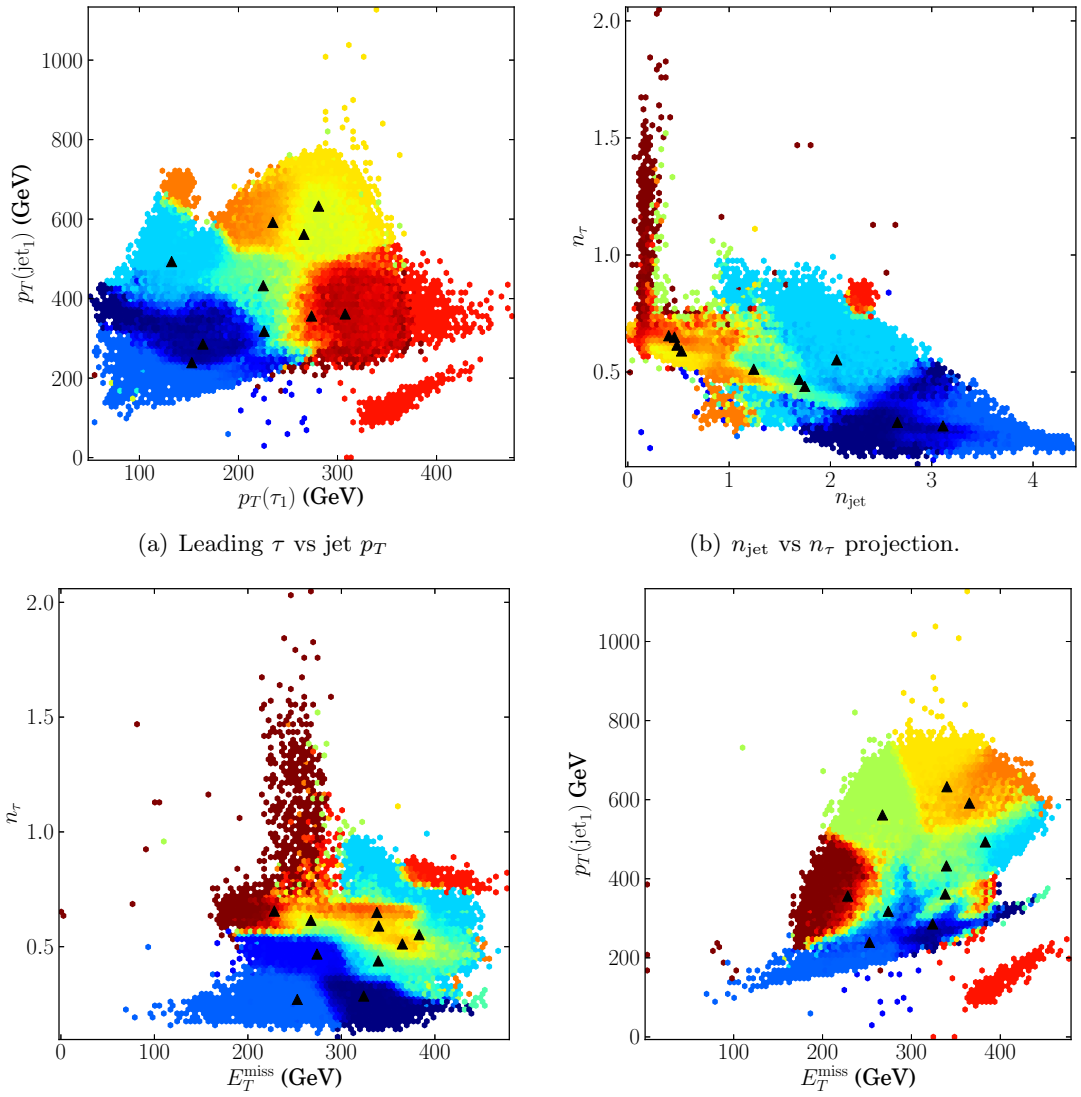

(a) Leading τ vs jet p_T

(b) n_{jet} vs n_τ projection.

(c) $\not{E}_T$ vs n_τ projection.

(d) $\not{E}_T$ vs leading jet p_T projection.

Figure 7. Projections of clusters. Colors indicate to which cluster a model belongs. Black triangles indicate locations clusters centroids.

Acknowledgments

This work has been performed in the scope of the Centre for Dark Matter Research (DAMARA) at the Department of Physics and Technology, University of Bergen, Norway. It was funded by the Bergen Research Foundation and the University of Bergen, as well as the Norwegian Research Council in the framework of High Energy Particle Physics project.

We would like to give special thanks Therese Sjursen for fruitful discussions leading to the start-up of this work and Per Osland for reading through the paper and providing useful comments. We would also like to thank members of the group for Subatomic Physics at University of Bergen for their support.

JHEP08(2013)098

Constraints	Range	Distribution
Ωh^2	$(0, 0.2]$	Flat
$\mathbf{Br}\,(b \to s + \gamma)$	$[2.71, 4.39] \cdot 10^{-4}$	Gaussian
$\mathbf{Br}\,(B_s \to \mu\mu)$	$[0.2, 6.2] \cdot 10^{-9}$	Gaussian
m_{h0}	$[122.3, 128.7]$ GeV	Gaussian
$\langle N_\tau \rangle$	$[1, \infty)$	Flat

Table 8. Experimental constraints used in the initial sampling.

A Scan implementation, clustering and cross-checks

The implementation of the scan was written in `Python`. It was capable of running multiple MCMC chains in parallel. The scan was initiated using a random sample containing roughly 100 points to find an estimate for the proposal distribution. The initial points were required to pass all discrete constraints, be within 2σ of the best fit values for $\mathbf{Br}(b \to s + \gamma)$, $\mathbf{Br}\,(B_s \to \mu\mu)$, m_{h0}, while having Ωh^2 of the right order of magnitude and an expected number of produced τ leptons, $\langle N_\tau \rangle > 1$. The values are summarized in table 8, together with the distributions used for initializing the proposal distribution.

Five clusters were established from the initial parameter space points with the *k-means* algorithm. This number was found to be sufficient to give a reasonable approximation of the likelihood distribution of the sample. From the initial sample, ten chains were initiated with two chains starting from each cluster. Before sampling started, each chain was required to reach a minimum likelihood to be included in the sample. This was chosen to be 2σ away from the central value for $\mathbf{Br}(b \to s + \gamma)$, $\mathbf{Br}\,(B_s \to \mu\mu)$, m_{h0}, Ωh^2, in addition to $\langle N_\tau \rangle \geq 1$, corresponding to the likelihood, $\ln P_{\min} \sim -4 \cdot \frac{4}{2} - 0.5 = -8.5$.

The proposal distribution was updated at intervals $\Delta N = 1000$ steps by adding the new sample points and recalculating cluster means and covariances. The new points were added without weights since they were already a product of weighted sampling. For practical purposes we end the optimization after 10 000 steps, which was found to be sufficient to give a good proposal estimate. By fixing the proposal after a certain number of steps the algorithm also satisy the neccessary conditions to ensure asymptotic convergence toward the true likelihood distribution, since the algorithm becomes equivalent to running a set of independent Metropolis-Hastings chains. The search chains were run in parallel on twenty cores for roughly 200 hours, resulting in a sample size of $N = 2\ 076\ 133$, corresponding to 105 209 unique models. From this sample 848 outliers (corresponding to 66 unique models) with log-likelihood $ln\ P < -8.5$ were removed.

In order to illustrate the effects of the different experimental and theoretical constraints, low energy properties were calculated for 300 000 models sampled uniformly within the search range. The computationally expensive `Pythia` simulations where not done for these models and a looser relic density constraint compared to the one used for MCMC initialization was used to get sufficient data to describe the qualitative features of the constraint.

JHEP08(2013)098

As a cross-check with the vast literature on the subject (see for example [38, 53, 54]) we briefly describe the effects of the most important constraints by visualizing how the initial selections affect the model density. The effects are illustrated in figure 8. We observe, in agreement with results of [15, 53] that:

- **Theoretical constraints**
  Theoretical constraints remove the low m_0 and $m_{1/2}$ regions primarily avoiding a $\tilde{\tau}_1$-LSP and tachyonic sparticles. The excluded regions becomes larger at large $\tan\beta$ and $|A_0|$, and for large values of A_0 a considerable part of the low mass regions, $m_0, m_{1/2} \lesssim 1000$ GeV gives tachyons.

- **Higgs mass $\mathbf{m_{h0} \in [122, 128]}$**
  Requiring a 125.5 GeV Higgs mass, with positive μ excludes all positive values of A_0 within the selected $m_0, m_{1/2}$-range. For large negative values of A_0 however, the $\tilde{t}$-loop corrections to the Higgs mass become large. This is the main reason for the asymmetry in A_0 seen in 3. At large values of $m_{1/2}$ and m_0 the `FeynHiggs` calculations of the Higgs mass corrections become inaccurate and thus we excluded these regions.

- **Relic density $\mathbf{\Omega h^2 < 1}$**
  As is well known, the relic density Dark Matter in CMSSM is generally orders of magnitude larger than allowed by WMAP and PLANCK results [54–56], apart from special regions where the relic density is suppressed by resonant neutralino annihilation or co-annihilation cross-sections. The low $m_{1/2}$ region where $m_{\tilde{\chi}_1^0} \lesssim 10$, the relic density is mainly suppressed through χ-annihilation to fermions through sfermion exchange (low m_0), and to W, Z pairs (high m_0). This region is excluded primarily by Higgs mass requirements. Along the $\tilde{\chi}_1^0$-LSP boundary the relic density is reduced by $\chi - \tilde{\tau}$-coannihilation, since the coannihilation cross-section is significantly enhanced due to mass degeneracy between the lightest stau and the lightest neutralino. The middle region in the mass plane, the well known Higgs funnel [57], corresponds to high $\tan\beta$ models with $m_{\tilde{\chi}_1^0} \sim 1/2 m_{H^0, A^0}$, giving an increase in $\chi - \chi$-annihilation through heavy neutral higgs bosons, (H^0,A^0). The preference for $A_0 \sim 0$ arises mainly from the fact that large parts of the low $m_{1/2}$ regions exhibit charged LSP or tachyonic particles for large values of $|A_0|$, as off-diagonal terms in the third generation sfermion mass matrices grow with $|A_0|$. The preference for high $\tan\beta$ is in part due to the additional relic density suppression through the Higgs channel χ-annihilation.

- **Rare decays $\mathbf{Br(B_s \to \mu\mu) < 4.5 \cdot 10^{-9}}$, $\mathbf{Br(b \to s + \gamma) \in [3, 4] \cdot 10^{-4}}$**
  Of the constraints on decays, $B_s \to \mu\mu$ poses the most stringent one, as the SUSY contribution grows like $\tan\beta^6$. This branching fraction tends to get too large at low values of $m0$ and $m_{1/2}$. The size of the excluded area in the mass plane increases with increasing $tan\beta$ and decreasing $|A_0|$. $\mathbf{Br}(b \to s + \gamma)$ is generally too low compared to the central experimental value of $3.55 \cdot 10^{-4}$ and excludes large parts of the low $m_{1/2} \lesssim 500$ range, stretching as far as $m_0 \sim 2000$ for high values of $\tan\beta$ and low $|A_0|$. Too high $\mathbf{Br}(B_s \to \mu\mu)$ and too low $\mathbf{Br}(b \to s + \gamma)$, together with the requirement of non-tachyonic sparticles constrains the lowest allowed values of $m_{1/2}$.

JHEP08(2013)098

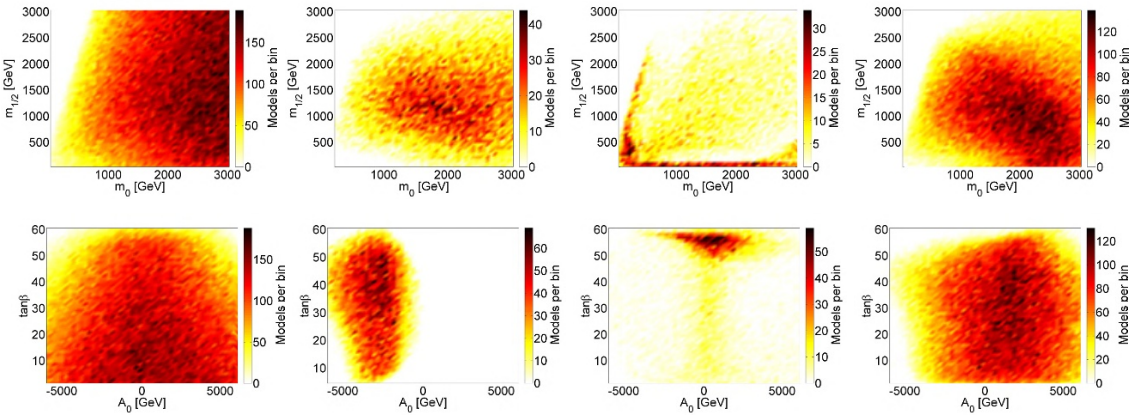

(a) Theoretical constraints (b) Th.C+m_{h0} (c) Th.C+Ωh^2 (d) Th.C+$\mathbf{Br}_{B_s\to\mu\mu,b\to s\gamma}$

Figure 8. 2D-histograms in $m_0, m_{1/2}$ and $A_0, \tan\beta$-planes showing the effects of different constraints. The constraints used corresponds to requirements chosen for the initial sample given in table 8.

The properties of selected high likelihood models are presented in the results section, 3.1. The relatively wide range of values for SUSY masses and values of $\tan\beta$ for the selected models lead to a wide range of values of phenomenological properties such as average $\not{E}_T$,the average missing energy per SUSY event, $p_T(\tau_1), p_T(\text{jet}_1)$, the average p_T of the leading τ and the leading jet, and n_τ, n_{jet}, the average number of τ's/jets per SUSY event, see figures 2 and 4. In order to construct reference models that cover these different phenomenological properties the sample was clustered according to the phenomenological observables listed above. In order to avoid bias from the scale of the different variables, each variable x is first transformed as $x' = (x_i - \bar{x})/\sigma_x$ so that the mean $\bar{x}' = 0$ and variance $\sigma^2_{x'} = 1$. Because the non-Gaussian nature of clusters the *g-means* algorithm often fail and split too often. To remedy this the constraining parameters mentioned in section 2.4 are used. By setting an approximate maximum number of possible clusters $n_{\max}$, one gets $\min_P = \lceil N_{\text{OK}}/n_{\max} \rceil$ for the minimum number of points in a cluster and $\min_s = \lceil \log_2 n_{\max} \rceil$ for the maximal splitting depth. The maximal number of iterations per split attempt was set to $\max_i = 20$. Here the number is chosen to be well above the final number of clusters but low enough, for this case $n_{\max} = 100$ was found to be appropriate. The minimal cluster distance parameter was set to $\min_d = 1.3$. The optimization was run $n_{\text{avg}} = 7$ times and an average of 9.8 clusters were found. Thus, one of the results with 10 clusters was picked at random. The properties of models at the centroids of these clusters, which can be seen as reference models for search optimization, are presented in the results section 3.1.

References

[1] H.P. Nilles, *Supersymmetry, supergravity and particle physics*, *Phys. Rept.* **110** (1984) 1 [INSPIRE].

[2] H.E. Haber and G.L. Kane, *The search for supersymmetry: probing physics beyond the standard model*, *Phys. Rept.* **117** (1985) 75 [INSPIRE].

JHEP08(2013)098

[3] S.P. Martin, *A supersymmetry primer*, hep-ph/9709356 [INSPIRE].

[4] Particle Data Group collaboration, K. Nakamura et al., *Review of particle physics*, *J. Phys.* **G 37** (2010) 075021 [INSPIRE].

[5] J.R. Ellis, T. Falk, G. Ganis, K.A. Olive and M. Srednicki, *The CMSSM parameter space at large* $\tan\beta$, *Phys. Lett.* **B 510** (2001) 236 [hep-ph/0102098] [INSPIRE].

[6] A.H. Chamseddine, R. Arnowitt, and P. Nath, *Locally supersymmetric grand unification*, *Phys. Rev. Lett.* **49** (1982) 970 [INSPIRE].

[7] M. Drees and M.M. Nojiri, *The Neutralino relic density in minimal* $N = 1$ *supergravity*, *Phys. Rev.* **D 47** (1993) 376 [hep-ph/9207234] [INSPIRE].

[8] J.R. Ellis, T. Falk, K.A. Olive and M. Schmitt, *Constraints on neutralino dark matter from LEP-2 and cosmology*, *Phys. Lett.* **B 413** (1997) 355 [hep-ph/9705444] [INSPIRE].

[9] A. Lipniacka, *Can SUSY be found at the Tevatron run II?*, hep-ph/0112280 [INSPIRE].

[10] H. Baer, A. Mustafayev, S. Profumo, A. Belyaev and X. Tata, *Direct, indirect and collider detection of neutralino dark matter in SUSY models with non-universal Higgs masses*, *JHEP* **07** (2005) 065 [hep-ph/0504001] [INSPIRE].

[11] H. Baer, A. Mustafayev, S. Profumo, A. Belyaev and X. Tata, *Neutralino cold dark matter in a one parameter extension of the minimal supergravity model*, *Phys. Rev.* **D 71** (2005) 095008 [hep-ph/0412059] [INSPIRE].

[12] M. Stoye, *SUSY results from CMS*, CMS-CR-2012-118 (2012).

[13] R. Bruneliere, *Search for supersymmetry at ATLAS*, ATL-PHYS-PROC-2012-073 (2012).

[14] O. Buchmueller et al., *The CMSSM and NUHM1 in light of* 7 *TeV LHC,* B_s *to* $\mu^+\mu^-$ *and XENON100 data*, *Eur. Phys. J.* **C 72** (2012) 2243 [arXiv:1207.7315] [INSPIRE].

[15] A. Fowlie et al., *The CMSSM favoring new territories: the impact of new LHC limits and a* 125 *GeV Higgs*, *Phys. Rev.* **D 86** (2012) 075010 [arXiv:1206.0264] [INSPIRE].

[16] S. Ovyn, X. Rouby and V. Lemaitre, *DELPHES, a framework for fast simulation of a generic collider experiment*, arXiv:0903.2225 [INSPIRE].

[17] J. Conway, *PGS: Pretty Good Simulator*, http://physics.ucdavis.edu/~conway/research/software/pgs/pgs4-general.htm.

[18] O. Buchmueller et al., *The MasterCode project*, http://mastercode.web.cern.ch/mastercode/index.php

[19] ATLAS collaboration, *Combined measurements of the mass and signal strength of the Higgs-like boson with the ATLAS detector using up to* $25\,fb^{-1}$ *of proton-proton collision data*, ATLAS-CONF-2013-014 (2013).

[20] A. Gelman, S. Brooks, G. Jones and X. Meng, *Handbook of Markov chain Monte Carlo*, Chapman & Hall/CRC Handbooks of Modern Statistical Methods, CRC Press, U.S.A. (2010).

[21] B. Allanach et al., *SUSY Les Houches Accord 2*, *Comput. Phys. Commun.* **180** (2009) 8 [arXiv:0801.0045] [INSPIRE].

[22] F.E. Paige, S.D. Protopopescu, H. Baer and X. Tata, *ISAJET 7.69: a Monte Carlo event generator for pp,* $\bar{p}p$ *and* e^+e^- *reactions*, hep-ph/0312045 [INSPIRE].

JHEP08(2013)098

[23] S. Heinemeyer, W. Hollik and G. Weiglein, *FeynHiggs: a program for the calculation of the masses of the neutral CP even Higgs bosons in the MSSM*, *Comput. Phys. Commun.* **124** (2000) 76 [hep-ph/9812320] [INSPIRE].

[24] P. Bechtle, O. Brein, S. Heinemeyer, G. Weiglein and K.E. Williams, *HiggsBounds: confronting arbitrary Higgs sectors with exclusion bounds from LEP and the Tevatron*, *Comput. Phys. Commun.* **181** (2010) 138 [arXiv:0811.4169] [INSPIRE].

[25] P. Gondolo et al., *DarkSUSY: computing supersymmetric dark matter properties numerically*, *JCAP* **07** (2004) 008 [astro-ph/0406204] [INSPIRE].

[26] K. Hagiwara et al., *Review of particle physics*, *Phys. Rev.* **D 66** (2002) 010001 [INSPIRE].

[27] DELPHI collaboration, J. Abdallah et al., *Searches for supersymmetric particles in e^+e^- collisions up to 208 GeV and interpretation of the results within the MSSM*, *Eur. Phys. J.* **C 31** (2003) 421 [hep-ex/0311019] [INSPIRE].

[28] T. Sjöstrand, S. Mrenna and P.Z. Skands, *A brief introduction to PYTHIA 8.1*, *Comput. Phys. Commun.* **178** (2008) 852 [arXiv:0710.3820] [INSPIRE].

[29] PLANCK collaboration, P. Ade et al., *Planck 2013 results. XVI. Cosmological parameters*, arXiv:1303.5076 [INSPIRE].

[30] HEAVY FLAVOR AVERAGING GROUP collaboration, D. Asner et al., *Averages of b-hadron, c-hadron and τ-lepton properties*, arXiv:1010.1589 [INSPIRE].

[31] P. Gondolo et al., *DarkSUSY darksusy-5.0.5*, manual and short description of routines (June 2009).

[32] R. Aaij et al., *First evidence for the decay $B_s^0 \to \mu^+\mu^-$*, CERN-PH-EP-2012-335 (2012).

[33] G. Degrassi, S. Heinemeyer, W. Hollik, P. Slavich and G. Weiglein, *Towards high precision predictions for the MSSM Higgs sector*, *Eur. Phys. J.* **C 28** (2003) 133 [hep-ph/0212020] [INSPIRE].

[34] ATLAS collaboration, *Search for supersymmetry in events with large missing transverse momentum, jets and at least one tau lepton in 21 fb^{-1} of $\sqrt{s} = 8$ TeV proton-proton collision data with the ATLAS detector*, ATLAS-CONF-2013-026 (2013).

[35] D. Goncalves-Netto, D. Lopez-Val, K. Mawatari, T. Plehn and I. Wigmore, *Automated squark and gluino production to next-to-leading order*, *Phys. Rev.* **D 87** (2013) 014002 [arXiv:1211.0286] [INSPIRE].

[36] W. Beenakker, R. Hopker, M. Spira and P. Zerwas, *Squark and gluino production at hadron colliders*, *Nucl. Phys.* **B 492** (1997) 51 [hep-ph/9610490] [INSPIRE].

[37] W. Beenakker, R. Hopker and M. Spira, *PROSPINO: a program for the production of supersymmetric particles in next-to-leading order QCD*, hep-ph/9611232 [INSPIRE].

[38] B. Allanach and C. Lester, *Multi-dimensional mSUGRA likelihood maps*, *Phys. Rev.* **D 73** (2006) 015013 [hep-ph/0507283] [INSPIRE].

[39] S. Bodenstein, C. Dominguez, K. Schilcher and H. Spiesberger, *Hadronic contribution to the muon $g-2$ factor*, arXiv:1302.1735 [INSPIRE].

[40] ALEPH, DELPHI, L3, OPAL, LEP WORKING GROUP FOR HIGGS BOSON SEARCHES collaboration, S. Schael et al., *Search for neutral MSSM Higgs bosons at LEP*, *Eur. Phys. J.* **C 47** (2006) 547 [hep-ex/0602042] [INSPIRE].

JHEP08(2013)098

[41] I. Niessen, *Supersymmetric phenomenology in the mSUGRA parameter space*, arXiv:0809.1748 [INSPIRE].

[42] W.K. Hastings, *Monte Carlo sampling methods using markov chains and their applications*, *Biometrika* **57** (1970) 97.

[43] R.V. Craiu and A. Fabio Di Narzo, *A mixture-based approach to regional adaptation for MCMC*, arXiv:0903.5292.

[44] B.C. Allanach and C.G. Lester, *Sampling using a 'bank' of clues*, *Comput. Phys. Commun.* **179** (2008) 256 [arXiv:0705.0486] [INSPIRE].

[45] Y. Guan, R. Fleißner, P. Joyce and S.M. Krone, *Markov chain Monte Carlo in small worlds*, *Stat. Comput.* **16** (2006) 193.

[46] M. West, *Approximating posterior distributions by mixtures*, *J. Roy. Stat. Soc.* **B 55** (1993) 409.

[47] G.O. Roberts, A. Gelman and W.R. Gilks, *Weak convergence and optimal scaling of random walk metropolis algorithms*, *Ann. Appl. Probab.* **7** (1997) 110.

[48] J. MacQueen, *Some methods for classification and analysis of multivariate observations*, in the proceedings of the 5^{th} *Berkeley Symposium on Mathematical Statistics and Probability*, December 27–January 7, University of California, U.S.A. (1967).

[49] D. Arthur and S. Vassilvitskii, *k-means++: the advantages of careful seeding*, Technical Report 2006-13, Stanford InfoLab (2006).

[50] G. Hamerly and C. Elkan, *Learning the k in k-means*, in *Advances in neural information processing systems*, S. Becker et al. eds., MIT Press, U.S.A. (2003).

[51] M.A. Stephens, *Edf statistics for goodness of fit and some comparisons*, *J. Amer. Stat. Assoc.* **69** (1974) 730.

[52] J. Cao, Z. Heng, J.M. Yang and J. Zhu, *Status of low energy SUSY models confronted with the LHC* 125 *GeV Higgs data*, *JHEP* **10** (2012) 079 [arXiv:1207.3698] [INSPIRE].

[53] S. Profumo, *The quest for supersymmetry: early LHC results versus direct and indirect neutralino dark matter searches*, *Phys. Rev.* **D 84** (2011) 015008 [arXiv:1105.5162] [INSPIRE].

[54] J.R. Ellis, T. Falk, K.A. Olive and M. Srednicki, *Calculations of neutralino-stau coannihilation channels and the cosmologically relevant region of MSSM parameter space*, *Astropart. Phys.* **13** (2000) 181 [*Erratum ibid.* **15** (2001) 413-414] [hep-ph/9905481] [INSPIRE].

[55] H. Baer, E.-K. Park and X. Tata, *Collider, direct and indirect detection of supersymmetric dark matter*, *New J. Phys.* **11** (2009) 105024 [arXiv:0903.0555] [INSPIRE].

[56] H. Baer et al., *Exploring the BWCA (bino-wino co-annihilation) scenario for neutralino dark matter*, *JHEP* **12** (2005) 011 [hep-ph/0511034] [INSPIRE].

[57] L. Roszkowski, R. Ruiz de Austri and T. Nihei, *New cosmological and experimental constraints on the CMSSM*, *JHEP* **08** (2001) 024 [hep-ph/0106334] [INSPIRE].

JHEP08(2013)098

Part II

Screened Modified Gravity

Chapter 5

General Relativity

This chapter is mainly based on [39], [59] and [90]

5.1 Einstein's Field Equations

The modern description of gravitational phenomena is based on Einstein's General theory of Relativity (GR), where the gravitational force is a manifestation of the curvature of spacetime. According to Einstein, matter tells spacetime how to curve, while the curvature determines how matter moves. The main underlying principle is *Einstein's Equivalence Principle*, which states that in any sufficiently small region of spacetime the laws of nature reduce to those of special relativity, or put differently freely falling observers are inertial. This implies that what we feel as a gravitational force is really due to non-gravitational forces preventing us from falling freely. Promoting freely falling observers to inertial ones, also suggest that the laws of nature should take the same form in any coordinate system, e.g they should be written in terms of tensors, $T^{\mu\cdots\nu}{}_{\alpha\cdots\beta}$, which transforms under general coordinate transformations as

$$x^{\mu} \to x^{\nu'}: \quad T^{\mu'\cdots\nu'}{}_{\alpha'\cdots\beta'} = \frac{\partial x^{\mu'}}{\partial x^{\mu}} \cdots \frac{\partial x^{\nu'}}{\partial x^{\nu}} \frac{\partial x^{\alpha}}{\partial x^{\alpha'}} \cdots \frac{\partial x^{\beta}}{\partial x^{\beta'}} T^{\mu\cdots\nu}{}_{\alpha\cdots\beta} \tag{5.1}$$

The geometry of spacetime is described by the metric tensor $g_{\mu\nu}$, which defines the relation between space and time in a given coordinate system in terms of the invariant line-element ds^2

$$ds^2 = g_{\mu\nu} dx^{\mu} dx^{\nu} \tag{5.2}$$

The line element generalizes the concept of the infinitesimal measure of length in ordinary space to spacetime and can be used to relate the motion of observers in different coordinate systems. In particular, for a given path through spacetime there exists a reference frame where the associated observer is at rest. In this frame the line element is given by the change in time only

$$ds^2 = -d\tau^2 \tag{5.3}$$

The time measured in this reference frame τ is called the proper time and corresponds to the time measured along the path. Paths where $ds^2 < 0$, are called timelike and spacetime points connected by such paths are causally connected. Paths with $ds^2 = 0$ are called lightlike, reflecting the fact that light follows such world lines, while paths with $ds^2 > 0$ are called spacelike and points connected by only such paths can never be in causal contact. For timelike paths it is usual to parametrize the path using the proper time $x^\mu(\tau)$ and freely falling observers follow spacetime paths $x^\mu(\tau)$ that maximizes proper time. These paths are called geodesics and are given by the geodesic equation

$$\frac{d^2x^\mu}{d\tau^2} + \Gamma^\mu{}_{\alpha\nu}\frac{dx^\nu}{d\tau}\frac{dx^\alpha}{d\tau} = 0 \tag{5.4}$$

The symbols $\Gamma^\mu{}_{\alpha\nu}$ are called connection coefficients, and measure how much the coordinate basis vectors $\vec{e}_\mu$ vary with spacetime

$$\frac{\partial \vec{e}_\alpha}{\partial x^\nu} = \Gamma^\mu{}_{\alpha\nu}\vec{e}_\mu \tag{5.5}$$

These can be related to the metric through the relation $g_{\mu\nu} = \vec{e}_\mu\vec{e}_\nu$ giving the explicit form

$$\Gamma^\alpha{}_{\mu\nu} = \frac{1}{2}g^{\sigma\alpha}\left(g_{\mu\sigma,\nu} + g_{\sigma\nu,\mu} - g_{\mu\nu,\sigma}\right) \tag{5.6}$$

The spacetime dependence of a general coordinate bases also means that the ordinary spacetime derivatives of a tensor, $\partial_\mu T^{\alpha,\ldots,\beta}$, is not itself a tensor, and in order to write laws involving derivatives in a coordinate independent way we need to generalize the concept of a spacetime derivative. This is done by introducing the spacetime covariant derivative ∇_ν which for a general tensor takes the form

$$\begin{aligned}\nabla_\sigma T^{\mu\cdots\nu}{}_{\alpha\cdots\beta} &= \partial_\sigma T^{\mu\cdots\nu}{}_{\alpha\cdots\beta} \\ &+ \Gamma^\mu{}_{\sigma\lambda}T^{\lambda\cdots\nu}{}_{\alpha\cdots\beta} + \cdots + \Gamma^\nu{}_{\sigma\lambda}T^{\mu\cdots\lambda}{}_{\alpha\cdots\beta} \\ &- \Gamma^\lambda{}_{\sigma\alpha}T^{\mu\cdots\nu}{}_{\lambda\cdots\beta} - \cdots - \Gamma^\lambda{}_{\sigma\beta}T^{\mu\cdots\nu}{}_{\alpha\cdots\lambda}\end{aligned} \tag{5.7}$$

This covariant derivative commutes with general coordinate transformations, which means that the covariant derivative of a tensor is itself a tensor as we wanted, and a general prescription for making laws valid in Minkowski spacetime covariant is to replace $\eta_{\mu\nu}$ with $g_{\mu\nu}$ and ∂_μ with ∇_μ. A nice feature of the covariant derivative is that in the case of scalar fields it reduces to ordinary derivatives $\nabla^\alpha\phi = \partial^\alpha\phi$ and this greatly simplifies the treatment of scalar fields in GR. It is important to note that the connection coefficients are not tensor quantities and can be non-zero also in flat spacetime, for instance in an accelerated reference frame where the connection term in 5.4 gives rise to a gravity like force term in accordance with the equivalence principle.

In order to separate true gravitational effects from fiducial ones which can be made to vanish by a suitable choice of coordinate system, one needs a proper definition of curvature. This can be achieved by introducing the concept of parallel transport of tensors along path $x^\mu(\lambda)$, which is the curved spacetime generalization of translating a vector along the path without changing it's direction

$$\nabla_\lambda \vec{A} = 0 \quad \rightarrow \quad \frac{dA^\mu}{d\lambda} + \Gamma^\mu{}_{\alpha\nu}\frac{dx^\nu}{d\lambda}A^\alpha = 0 \tag{5.8}$$

In the case of intrinsically curved spaces, the result of parallel transporting a tensor from one spacetime point to another depends on the path taken, and hence the notion of comparing tensors at different spacetime points is simply not well defined in General Relativity. However it is possible to use the notion of parallel transport to define the intrinsic curvature as the difference between the initial and final state of vectors under parallel transport along an infinitesimal loop as illustrated in figure 5.1.

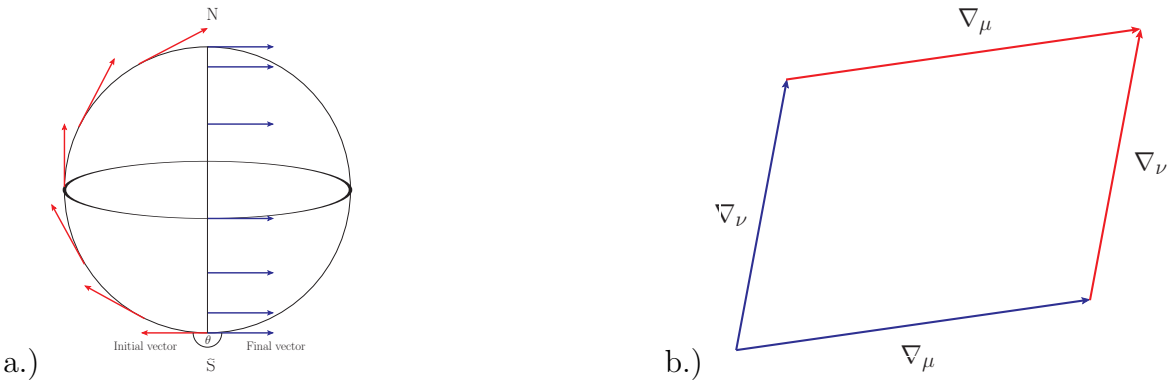

Figure 5.1: a.) Parallel transport of a vector on a sphere. Due to the intrinsic curvature the direction of the vector has change when arriving back at the original position. b.) The Commutator of two covariant derivatives

The result can be written in terms of the commutator of covariant derivatives along different paths, and yields a relation similar to the definition of the field-strength tensor in terms of gauge covariant derivatives in Yang-Mills theory eq. (2.13).

$$[\nabla_\mu, \nabla_\nu]\, A^\alpha = R^\alpha{}_{\beta\mu\nu}A^\beta \tag{5.9}$$

This is a proper tensor equation and as such valid in any reference frame. The resulting tensor $R^\alpha_{\beta\mu\nu}$ is called the Riemann curvature tensor and can also be expressed in terms of the connection coefficients

$$R^\alpha{}_{\beta\mu\nu} = \partial_\beta\Gamma^\alpha_{\mu\nu} - \partial_\nu\Gamma^\alpha_{\mu\beta} + \Gamma^\alpha_{\lambda\beta}\Gamma^\lambda_{\mu\nu} - \Gamma^\alpha_{\lambda\nu}\Gamma^\lambda_{\mu\beta} \tag{5.10}$$

Of the 256 components of the Riemann tensor only twenty are independent due to restrictions from several identities, stemming from the symmetries of the metric. By contracting indices, we can construct lower ranked curvature tensors called the Ricci tensor and the Ricci scalar

$$R_{\mu\nu} = R^{\lambda}{}_{\mu\lambda\nu} \quad , \quad R = R^{\lambda}{}_{\lambda} \tag{5.11}$$

Einstein himself used these quantities directly together with the identities mentioned earlier to construct a divergence free tensor which he could then relate to the stress-energy tensor. However, Einstein's field equations can also be stated in terms of an action principle, whereby the gravitational part of Einstein's equation corresponds to the simplest possible choice, namely the Ricci scalar R. By also including matter $\mathcal{L}_m(g_{\mu\nu}, \Psi_i)$, the full curved spacetime action can be written

$$S = \int \kappa R\sqrt{-g}d^4x + \int \mathcal{L}_m(g_{\mu\nu}, \Psi_i)d^4x \tag{5.12}$$

κ is a constant of proportionality determined by experiment, and $\sqrt{-g}d^4x$ is the invariant volume element needed to make the action integral invariant. It is conventional to absorb the metric determinant into the definition of $\mathcal{L}_m(g_{\mu\nu}, \Psi_i)$ represents the matter part of the Lagrangian, which should be modified compared to the Lagrangian given in chapter 3 so that it is invariant under general coordinate transformations. This can be done in a manner analogous to gauge theory, where the global Poincare invariance is gauged [32]. From the action given in eq. (5.12), Einstein's field equations follows from varying the action with respect to the metric $g_{\mu\nu}$[1]

$$R_{\mu\nu} - \frac{1}{2}Rg_{\mu\nu} = \frac{1}{2\kappa}T_{\mu\nu} \tag{5.13}$$

$$T_{\mu\nu} \equiv -\frac{2}{\sqrt{-g}}\frac{\partial\mathcal{L}_m}{\partial g^{\mu\nu}} \tag{5.14}$$

where $T_{\mu\nu}$ is taken to define the matter stress-energy tensor. This tensor is manifestly divergence free and symmetric as required by a proper stress-energy tensor, and is consistent with the definition from Noether's theorem. In the classical regime it is usually sufficient to consider the stress-energy tensor $T_{\mu\nu}$ directly without referring directly to the matter Lagrangian $\mathcal{L}_m$. Of particular importance is the perfect fluid approximation, where the fluid is assumed to conduct no heat and have zero viscosity. In this case the stress-energy tensor can be written in the form

$$T_{\mu\nu} = (\rho + p)U_\mu U_\nu + pg_{\mu\nu} \tag{5.15}$$

where ρ and p correspond to the comoving energy density and pressure of the fluid. The constant of proportionality κ in eq. (5.13) can be found by matching the equations with

[1] Up to boundary terms which can be dealt with if treated carefully

Newtons law of gravitation in the non-relativistic weak field limit

$$g_{\mu\nu} \approx \eta_{\mu\nu} - 2\Phi_N \delta_{ij} \quad , \quad \mathbf{v} << 1 \quad , \quad p_m << \rho_m \tag{5.16}$$

$$\Rightarrow \quad \nabla^2 \Phi_N \approx \frac{1}{4\kappa}\rho_m \quad \Rightarrow \quad \kappa = \frac{1}{16\pi G} = \frac{M_{Pl}^2}{2} \tag{5.17}$$

resulting in Einstein's famous equations

$$R_{\mu\nu} - \frac{1}{2}R g_{\mu\nu} = \frac{1}{M_{Pl}^2} T_{\mu\nu} \tag{5.18}$$

Of the 16 equations in eq. (5.18), 12 are pairwise related due to the symmetry in the indices $\mu\nu = \nu\mu$, leaving 10 independent equations. Furthermore the fact that the equations are divergence free gives four more constraints giving 6 independent field equations. This reflects the fact that although the metric $g_{\mu\nu}$ contains 10 degrees of freedom, four of these are related to the invariance under general coordinate transformations. This leaves a set of six, non-linear coupled second order differential equations which are very hard to solve in general and usually one has to resort to numerics to find interesting solutions.

5.2 The ΛCDM Model

One exception to this rule is the large scale evolution of the universe, where the universe can be approximated as spatially homogeneous and isotropic. In this case the line element ds^2 can be written in terms of only two parameters $a(t)$ and k

$$ds^2 = -dt^2 + a^2(t)\left[\frac{1}{1-kr^2}dr^2 + r^2 d\Omega^2\right] \quad , \quad d\Omega^2 = d\theta^2 + \sin^2\theta d\phi^2 \tag{5.19}$$

where $a(t)$ is called the scale factor and gives the spatial size of the universe at a time t (Usually normalized so that $a = 1$ today), while k describes the intrinsic spatial curvature of the universe. When $k > 0$ space is said to be positively curved and the spatial geometry is spherical. This is usually referred to as a *closed* universe because its spatial extension is finite. If $k < 0$ space is said to have negative curvature and the spatial geometry is hyperbolic. In this case the space is infinite and we refer to such universes as *open* . The limiting case where $k = 0$ corresponds to no spatial curvature, see figure 5.2.

Observations indicate that the universe is very close to flat today, a feature which is usually attributed to a period of inflation in the very early universe that flattened out any initial spatial curvature. The matter stress energy tensor can be approximated by a comoving perfect fluid with four velocity $U^\mu = (-1, 0)$, so that the

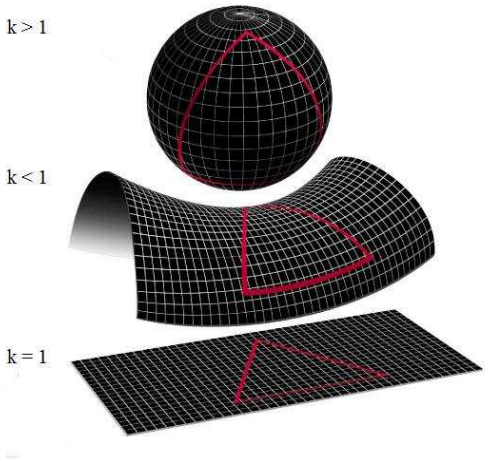

Figure 5.2: 2D analogies to the curvature of 3D space given by k. The image is taken from [87]

$$(T_{\mu\nu}) = \begin{pmatrix} \rho & 0 & 0 & 0 \\ 0 & a^2 p & 0 & 0 \\ 0 & 0 & a^2 r^2 p & 0 \\ 0 & 0 & 0 & a^2 r^2 \sin^2\theta p \end{pmatrix} \tag{5.20}$$

These simplifications allow us to reduce the number of free parameters to three parameters a, ρ and p, and Einstein's equations simplify to give the Friedmann equations.

$$\dot{a}^2 = \frac{1}{3M_{Pl}^2}\rho a^2 \tag{5.21}$$

$$\frac{\ddot{a}}{a} = -\frac{1}{6M_{Pl}^2}(\rho + 3p) \tag{5.22}$$

Another useful relation comes from conservation of energy and momentum, namely the adiabatic equation

$$\dot{\rho} = -\frac{3\dot{a}}{a}(\rho + p) \tag{5.23}$$

Usually one also assumes that the total matter fluid can be decomposed into separate components, each of which can be describe by a simple equation of state on the form $p = \omega\rho$, where ω is determined by the matter species under consideration. On cosmological scales non-relativistic matter is approximated by a pressureless fluid with $\omega_m = 0$, while radiation is described by a traceless stress energy tensor, $\omega_r = 1/3$. Under these assumptions, the

adiabatic equation immediately tells us how the density and pressure of given species i evolves as a function of the scale factor a

$$\rho = \rho_0 \left(\frac{a_0}{a}\right)^{3(1+\omega)} \tag{5.24}$$

where ρ_0 and a_0 are usually taken to be the values of the density and scale factor today. From eq. (5.24) we see that the density of pressureless matter is proportional to a^{-3}, reflecting the fact that the energy density of pressureless matter is proportional to the number of particles per volume, while for radiation the energy density goes as a^{-4}, which stems from an additional cosmological red shift z of photons given by

$$z = \frac{\Delta\lambda}{\lambda_e} = \frac{1}{a(t_e)} - 1 \quad \Rightarrow a = (z+1)^{-1} \tag{5.25}$$

where z denotes the red shift of light between the time of emmision t_e and today . This allows us to use the scale factor and redshift interchangeably as a measure of the size of the universe at a given time. Equation 5.21 is usually written in terms of the Hubble parameter $H(t)$ which gives the expansion rate relative to size, and a set of dimensionless density parameters Ω_i, defined relative to the critical density ρ_c , defined as the total energy density of a spatially flat universe

$$H(t) \equiv \frac{\dot{a}}{a} \quad , \quad \rho_c = \frac{3H^2}{8\pi G} \quad , \quad \Omega_i \equiv \frac{\rho_i}{\rho_c} = H_0^2 \Omega_{i0} a^{-3(1+\omega_i)} \tag{5.26}$$

With these conventions we can write the first Friedman equation in the form

$$H^2 = H_0^2 \sum_i \Omega_{i0} a^{-3(1+\omega_i)} \tag{5.27}$$

Given the estimates for the matter content and Hubble parameter today this equation can be easily integrated to give an approximate evolution of the universe on large scales. This remarkably simple approximation is the foundation of much of modern cosmology and has profound implications. First and foremost, equation 5.21 tells us that the universe cannot be static but has to evolve with time. In fact already in the late 1920's, Hubble found [66] that light sources are more and more red shifted the further away they are, indicating an expanding universe and ultimately giving rise to the now commonly accepted Big Bang model. At the end of the last century improved versions of essentially the same technique where used to deduce that not only is the universe expanding at present, but the expansion seems to be accelerating. The second Friedmann equation 5.22 tells us that the only way $\ddot{a} > 0$ is if the dominant source of energy in the universe has negative pressure $p < -1/3\rho$. One way to explain this behaviour is by introducing a cosmological constant Λ, given by the stress energy tensor

$$T^{\Lambda}_{\mu\nu} = -M_{Pl}^2 \Lambda g_{\mu\nu} \tag{5.28}$$

This gives an equation of state $\rho = -p$, and through equation 5.24, a constant energy density. Assuming the existence of such a cosmological constant gives a best fit model which

is spatially flat and with roughly 70% of the present energy in the form of a cosmological constant and 30% in the form of pressureless matter, see figure 5.3. Of the matter component, only 5% can be accounted for by regular baryonic matter, and hence the model is referred to as the ΛCDM model, where CDM stands for cold dark matter and alludes to the 25% not accounted for.

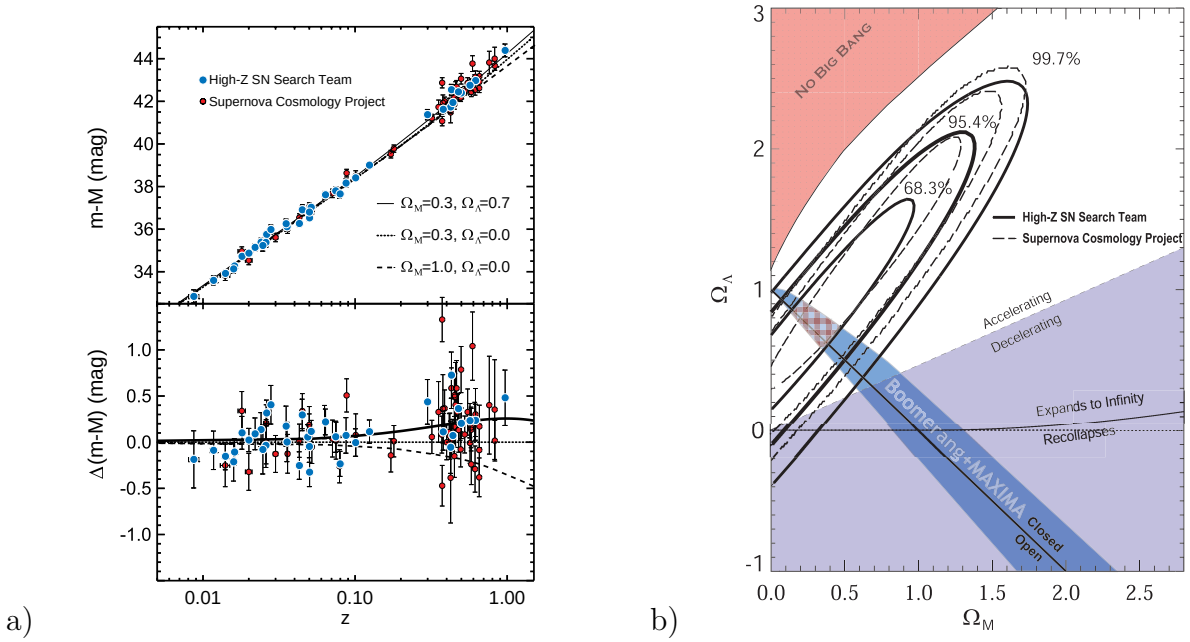

a) b)

Figure 5.3: a) The combined data of the Supernova Cosmology Project and the High-Z Supernova Team together with the theoretical predictions from three different models. The observations seem to prefer a universe with 30% matter and 70% dark energy. b) Constraints from the supernova search and from the CMB surveys BOOMERANG and MAXIMA1. Images taken from the [86]

In the subsequent years precision measurements of the Cosmic Microwave Background [70, 10] and Large Scale Structure Surveys [61] have found good agreement with predictions for both linear and non-linear density perturbations around the ΛCDM background, further solidifying its position as the reference model for all cosmological observations, see figure 5.4.

Like the standard model in particle physics, the ΛCDM model seems to describe the observed universe very well, but also faces some theoretical issues.

- **Origin of Dark Matter and Dark Energy** As of yet we have no satisfactory explanation for dark energy and although the vacuum energy as predicted by quantum field theory has the right properties, i.e negative pressure, the estimated magnitude should typically be 10^{100} times larger than that required by cosmological observations. It is conceivable that the sum of contributions to the vacuum energy approximately cancels yielding a small effective cosmological constant consistent with observations, but without any arguments for how or why the contributions should cancel to such a degree accuracy, it seems unlikely. This is known as the cosmological constant problem and is akin to the hierarchy problem in the Higgs sector discussed in chapter 3. When it comes to dark matter many proposed BSM theories of particle physics provide suitable dark matter candidates, however there is still no non-gravitational evidence for its existence.

- **The Coincidence Problem** The energy densities associated with the cosmological constant and cold dark matter are comparable today, which through the evolution equation 5.24 means the energy density of vacuum was negligible compared to matter in most of the past, while in the future the roles will be reversed. This begs the question why these two seemingly unrelated components are equal today.

In light of these considerations it seems reasonable to ask whether a more satisfying explanation can be found by modifying the gravitational part of the theory, rather than the matter sector. However for this to be viable the modified theory must give observable effects on cosmological and galactic scales while being in accord with the strict bounds on modifications to General Relativity coming from local tests of gravity. Models exhibiting such screening mechanisms will be discussed in the following, with emphasis on the chameleon model [69].

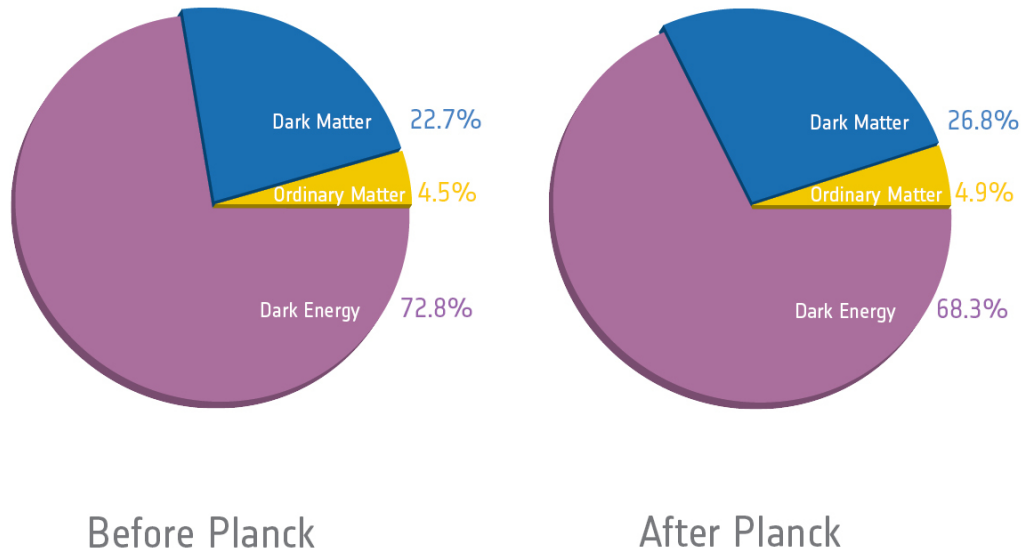

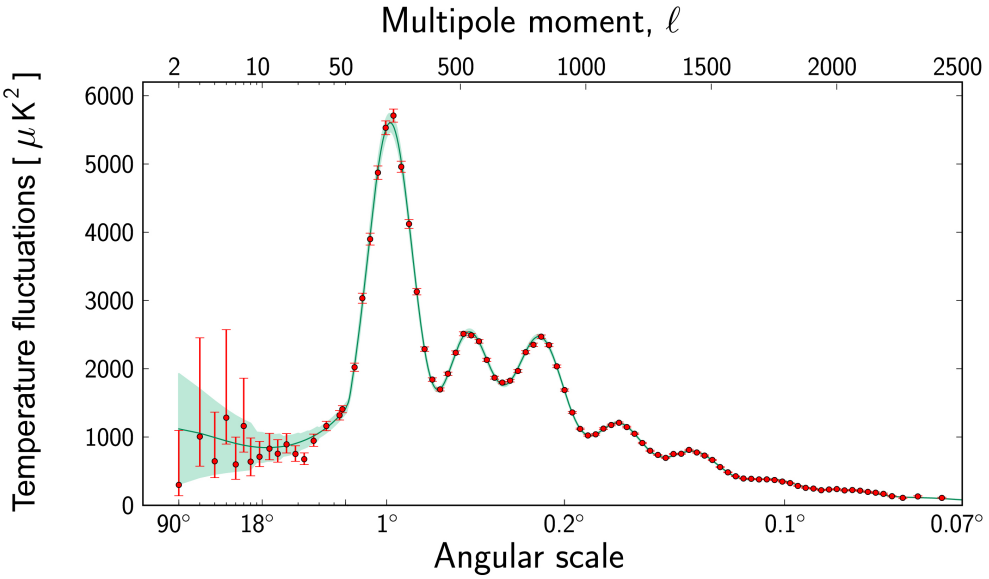

Figure 5.4: Top: Estimated ΛCDM based on results from the Planck survey of the Cosmic Microwave Background, taken from [60]. Bottom: CMB power spectrum as predicted by ΛCDM compared to Planck data, taken from [52]

Chapter 6

Screened Modified Gravity

This chapter is based mainly on [53], [20], [89], [33] and [68].

In general relativity, gravity is mediated by a single rank two tensor namely the metric $\tilde{g}_{\mu\nu}$, however there is little reason to assume that these are the only gravitational degrees of freedom. Many different modifications have been proposed ranging from simple scalar-tensor theories, involving a single new scalar field, to models involving both vector and tensor degrees freedom such as TeVeS and Bimetric Gravity [42]. In this thesis we only consider scalar-tensor modifications to Einstein's theory.

6.1 Scalar Tensor Theory

In scalar-tensor theory the gravitational part of the Lagrangian 5.12 is modified by introducing a new scalar field φ directly coupled to the curvature scalar $\tilde{R}$ through some function $f(\varphi)$[1]. For the models considered in this thesis a sufficiently general Lagrangian is [53]

$$\mathcal{S}_{ST} = \sqrt{-\tilde{g}}\frac{M_{Pl}^2}{2}f(\varphi)R + \mathcal{L}_\varphi(\varphi) + \mathcal{L}_m(\tilde{g}_{\mu\nu}, \psi_i) \tag{6.1}$$

$$\mathcal{L}_\varphi = -\sqrt{-\tilde{g}}\left(\frac{1}{2}\tilde{g}^{\mu\nu}\partial_\mu\varphi\partial_\nu\varphi + U(\varphi)\right) \tag{6.2}$$

Written this way the gravitational nature of the new scalar φ is clear, and leads to modifications to the gravitational side of Einstein's equations [39]

$$f(\varphi)\left(\tilde{R}_{\mu\nu} - \frac{1}{2}\tilde{R}g_{\mu\nu}\right) - \tilde{\nabla}_\mu\tilde{\nabla}_\nu f(\varphi) + \tilde{g}_{\mu\nu}\Box f(\varphi) = \frac{1}{M_{Pl}^2}\left(\tilde{T}_{\mu\nu}^{\varphi} + \tilde{T}_{\mu\nu}^{m}\right) \tag{6.3}$$

where the stress energy tensors $\tilde{T}_{\mu\nu}^{i}$ are given by 5.14, and $\Box \equiv \eta^{\mu\nu}\partial_\mu\partial_\nu$. These field equations are considerably more complicated than the original ones, eq. (5.18), and it is

[1]The use of twiddles ˜ to express geometric quantities is for later convenience, and are equivalent to the untwiddled ones in 5

therefore often convenient to write the Lagrangian in terms of the conformally related metric $g_{\mu\nu}$

$$\tilde{g}_{\mu\nu} = B(\varphi) g_{\mu\nu} \quad , \quad \tilde{g}^{\mu\nu} = B^{-1}(\varphi) g^{\mu\nu} \tag{6.4}$$

By relating the conformal factor $B(\varphi)$ to the scalar coupling $f(\varphi)$ and redefining the scalar field, we can rewrite the original Lagrangian in terms of an Einstein-Hilbert term for the new metric $g_{\mu\nu}$ and a canonical scalar field ϕ conformally coupled to matter through the metric

$$B(\varphi) = \frac{1}{f(\varphi)} \quad , \quad \partial_\varphi \phi \equiv \sqrt{\frac{3}{2}\left(\frac{\partial_\varphi f}{f}\right)^2 + \frac{1}{f}} \tag{6.5}$$

$$\mathcal{L}^E_{ST} = \sqrt{-g}\frac{M^2_{Pl}}{2} R + \mathcal{L}_\phi(\phi) + \mathcal{L}_m(\tilde{g}_{\mu\nu}, \psi_i) \tag{6.6}$$

$$\mathcal{L}_\phi = -\sqrt{-g}\left(\frac{1}{2} g^{\mu\nu}\partial_\mu\phi\partial_\nu\Phi + V(\phi)\right) \quad , \quad V(\phi) = \frac{U(\varphi)}{f^2} \tag{6.7}$$

The two different Lagrangians given in equations 6.6 and 6.1 corresponds to different conformal frames, where the original one is called the Jordan frame, and the new frame is called the Einstein frame. The two frames are mathematically equivalent, but give different physical interpretations of the solutions. In the Jordan frame, the non-minimal coupling can be interpreted as a spacetime dependent gravitational constant $\kappa(x^\mu)$, while in the Einstein frame the scalar coupling is moved to the matter sector and gives rise to spacetime dependent non-gravitational couplings instead. In this thesis we will focus on the Einstein frame description, but sometimes use Jordan frame arguments to simplify calculations.

6.2 Explicit Coupling in The Einstein Frame

In the Einstein frame the exact form of the matter stress-energy tensor depends on the specific field content of the matter sector. However in most scenarios it is sufficient to study the linearised coupling , $B(\phi) \approx 1 + \delta B(\phi)$, which allows us to write out the matter-scalar coupling explicitly

$$\mathcal{L}_m(g_{\mu\nu} + \delta g_{\mu\nu}, \psi_i) = \mathcal{L}_m(g_{\mu\nu}, \psi_i) + \frac{\sqrt{-g}}{2}\delta B(\phi) T^m \tag{6.8}$$

Here $T^m = T^m_{\mu\nu} g^{\mu\nu}$ denotes the trace of the stress-energy tensor of free matter in the Einstein frame, described by the Lagrangian $\mathcal{L}_m(g_{\mu\nu}, \psi_i)$. The coupling directly to the trace means radiation decouples from the scaler since it is described by a traceless stress-energy tensor. With the linearised coupling the modified Einstein equations take the form

$$R_{\mu\nu} - \frac{1}{2} R g_{\mu\nu} = \frac{1}{M^2_{Pl}}\left(T^m_{\mu\nu} + T^\phi_{\mu\nu} + \delta B\left[\frac{1}{2} T^m g_{\mu\nu} - \frac{\partial T^m}{\partial g^{\mu\nu}}\right]\right) \tag{6.9}$$

where the stress-energy tensor of the scalar field, $T^{\phi}_{\mu\nu}$ is given by

$$T^{\phi}_{\mu\nu} = \partial_\mu\phi\partial_\nu\phi - g_{\mu\nu}\left(\frac{1}{2}g^{\alpha\beta}\partial_\alpha\phi\partial_\beta\phi + V(\phi)\right) \tag{6.10}$$

If we also assume that matter is described by a perfect fluid with equation of state $p = \omega\rho$, the right hand side simplifies to

$$R_{\mu\nu} - \frac{1}{2}Rg_{\mu\nu} = \frac{1}{M^2_{Pl}}\left(T^m_{\mu\nu} + T^{\phi}_{\mu\nu} + \frac{(1-3\omega)}{2}\delta B T^m_{\mu\nu}\right) \tag{6.11}$$

As advertised the gravitational part of the field equations for the metric $g_{\mu\nu}$ is the same as in general relativity, but at the cost of introducing a coupling between the scalar field and matter. If the coupling δB is of gravitational strength the interaction term will be suppressed by additional factors of $M_P l$, making the direct effects on the curvature from this term negligible. The stress-energy tensor of the free scalar field $T^{\phi}_{\mu\nu}$ on the other hand has no such suppression and acts as a new energy component influencing the curvature of the metric $g_{\mu\nu}$. In particular, if we consider the cosmological evolution, the scalar field acts as a new energy component with energy density ρ_ϕ and pressure p_ϕ given by

$$\rho_\phi = \frac{1}{2}\dot{\phi}^2 + V(\phi) \quad , \quad p_\phi = \frac{1}{2}\dot{\phi}^2 - V(\phi) \quad , \quad \omega_\phi = \frac{\frac{1}{2}\dot{\phi}^2 - V(\phi)}{\frac{1}{2}\dot{\phi}^2 + V(\phi)} \tag{6.12}$$

which sources the modified Friedmann equations

$$\dot{a}^2 = \frac{a^2}{3M_{Pl}}\Big[\rho_\phi + \sum_i \kappa_i\rho_i\Big] \quad , \quad \kappa_i(\phi) = 1 + \frac{(1-3\omega_i)}{2}\delta B \tag{6.13}$$

$$\frac{\ddot{a}}{a} = -\frac{1}{6M^2_{Pl}}\Big[\rho_\phi + 3p_\phi + \sum_i \kappa_i(\rho_i + 3p_i)\Big] \tag{6.14}$$

If the field is slowly evolving $\dot{\phi}^2 << V(\phi)$, this gives an equation of state $\omega_\phi = -1$ and the field acts like a cosmological constant. This slow roll effect is one of the main reasons for considering cosmological scalar fields, and is also the driving mechanism for cosmic inflation. Though direct effects of the energy density associated with the coupling term are negligible the presence of the coupling means the matter stress-energy tensor $T^m_{\mu\nu}$ is no longer conserved and alters how the different components evolve with the scale factor $a(t)$ through a modified adiabatic equation 5.23. This leads to subtle effects not present in the uncoupled case, in particular when considering cosmological perturbation theory. However, as the work presented here focuses on astrophysical implications, we simply refer to the literature for a detailed account, see for example [20].

Another consequence of the non-conservation of energy and momentum in the matter sector, is that it allows for the creation of monopole and dipole scalar waves, unlike the metric waves in GR which requires sources with a quadrupole moment, such as binary black holes [9]. This is true also in the modified theory because conservation of the full stress-energy tensor sourcing metric perturbations, still hold

$$\nabla^\mu T^M_{\mu\nu} = \nabla^\mu \left(T^m_{\mu\nu} + T^\phi_{\mu\nu} + \frac{(1-3\omega)}{2} \delta B T^m_{\mu\nu} \right) = 0 \tag{6.15}$$

6.3 Fifth Forces

In the absence of non-gravitational interactions, particles are free in the Jordan frame, and follow geodesics of the Jordan frame metric $\tilde{g}_{\mu\nu}$. In the Einstein frame this is no longer true due to the scalar coupling in $\mathcal{L}_m$, which gives rise to an additional interaction term in the associated equations of motion

$$\frac{d^2x^\mu}{d\tau^2} + \Gamma^\mu_{\alpha\beta} \frac{dx^\alpha}{d\tau} \frac{dx^\beta}{d\tau} = -\frac{1}{2} \frac{B_{,\phi}}{B} \partial_\nu \phi \left(g^{\mu\nu} + 2 \frac{dx^\mu}{d\tau} \frac{dx^\nu}{d\tau} \right) \tag{6.16}$$

In the Newtonian limit this leads to an additional gravitational force, called the fifth force, which is proportional to the gradient of the scalar field

$$\frac{d^2\mathbf{x}}{dt^2} \approx -\boldsymbol{\nabla} \left(\Phi_N + \frac{1}{2} \ln B(\phi) \right) \tag{6.17}$$

How this new force term relates to current constraints on modifications to Newtons law, depends on the scalar field profile which is determined by the scalar field equation of motion. In this case the matter coupling leads to an effective potential for the scalar $V_{eff}(\phi, T_m)$, which depends on the local matter density

$$\nabla_\mu \nabla^\mu \phi = V(\phi)_{,\phi} - \frac{1}{2} \delta B_{,\phi}(\phi) T^m = V_{eff,\phi} \quad , \quad V_{eff} = V - \frac{1}{2} \delta B T^m \tag{6.18}$$

If the effective potential has a minima, this again leads to a matter dependent scalar mass which is given by $m^2 = V_{eff,\phi\phi}$. This mass is directly related to the range of the associated force which means that in regions where the mass is large the range of the associated force is suppressed. This can be illustrated by looking at linear perturbations around a fixed background for a non-relativistic matter source $T^m = -\rho$, where we let ρ_0 denote the background matter density and ϕ_0 be the minima of the potential in the background

$$\phi = \phi_0 + \varphi(x^\mu) \quad , \quad \rho = \rho_0 + \delta\rho(x^\mu) \tag{6.19}$$

If the scalar perturbations $\varphi(x^\mu)$ are small, the source term can be expanded around the minima

$$V_{eff,\phi}(\phi, \rho) \approx m^2 \delta\phi + \mu \delta\rho \tag{6.20}$$

$$m^2 = V^0_{eff,\phi\phi} = V^0_{,\phi\phi} + \frac{1}{2} \delta B_{,\phi\phi} \rho_0 \tag{6.21}$$

$$\mu = V^0_{eff,\phi\rho} = \frac{1}{2} \delta B_{,\phi} \tag{6.22}$$

and leads to linearised equations of motion given by

$$\left(\nabla_\mu \nabla^\mu - m^2\right)\varphi = \mu\delta\rho \tag{6.23}$$

This is simply the Klein-Gordon equation in the presence of a source, generalized to curved backgrounds. To illustrate the corrections to Newtons force law we consider the case of a static delta source with mass M in a fixed background.

$$\left(\partial_r^2 + \frac{2}{r}\partial_r - m^2\right)\varphi = \mu M\delta(r) \tag{6.24}$$

which has the solution

$$\varphi = -\frac{\mu M e^{-mr}}{4\pi r} \quad , \quad \nabla\varphi = \frac{\mu M e^{-mr}}{4\pi r^2}\left(1+mr\right) \tag{6.25}$$

As we see from eq. (6.25), the gradient $\nabla\varphi$ is exponentially suppressed compared to the Newtonian potential $\Phi_N = -GM/(4\pi r)$, on scales larger than the Compton wavelength of the field $\lambda = 1/m$. Using equation 6.17, this solution yields a correction to the Newtonian force law of the form

$$\frac{d^2\mathbf{r}}{dt^2} \approx -\frac{GM}{4\pi r^2}\left(1 + \frac{\mu B_{,\phi}}{2GB}\left(1+mr\right)e^{-mr}\right) \tag{6.26}$$

The mass suppression is quite general and only requires the effective potential to have a minima and that the scalar mass increases with matter density so the suppression becomes more pronounced in dense regions. However to pass local constraint on modified gravity while still being able to produce interesting effects on larger scales, this general suppression is not sufficient. Luckily there are a few specific choices of the conformal factor $B(\phi)$ and the scalar potential $V(\phi)$ which gives additional suppression through the non-linear features of the potential.

6.4 Screening Mechanisms

We will consider two screening mechanisms which both fit into the class of theories discussed so far: The symmetron [65] and the chameleon [68].

Symmetron

The symmetron relies on a Higgs like mechanism, where the potential and conformal factor are given by

$$B(\phi) = (1 + \frac{\phi^2}{2M^2})^2 \approx \frac{\phi^2}{M^2} \quad , \quad V(\phi) = V_0 - \frac{1}{2}\mu^2\phi^2 + \frac{1}{4}\lambda\phi^4 \tag{6.27}$$

where V_0 is a constant which could play the role of Λ. For this specific model choice equation 6.18 gives the following equation of motion and effective potential

$$\nabla_\mu \nabla^\mu \phi = \left(\frac{\rho}{M^2} - \mu^2 \right) \phi + \lambda \phi^3 \quad , \quad V_{eff} = V_0 + \frac{1}{2} \left(\frac{\rho}{M^2} - \mu^2 \right) \phi^2 + \frac{1}{4} \lambda \phi^4 \phi^2 \tag{6.28}$$

The effective potential takes the form of a 1-dimensional Higgs potential, where the quadratic parameter runs with energy density, see fig. 6.1.

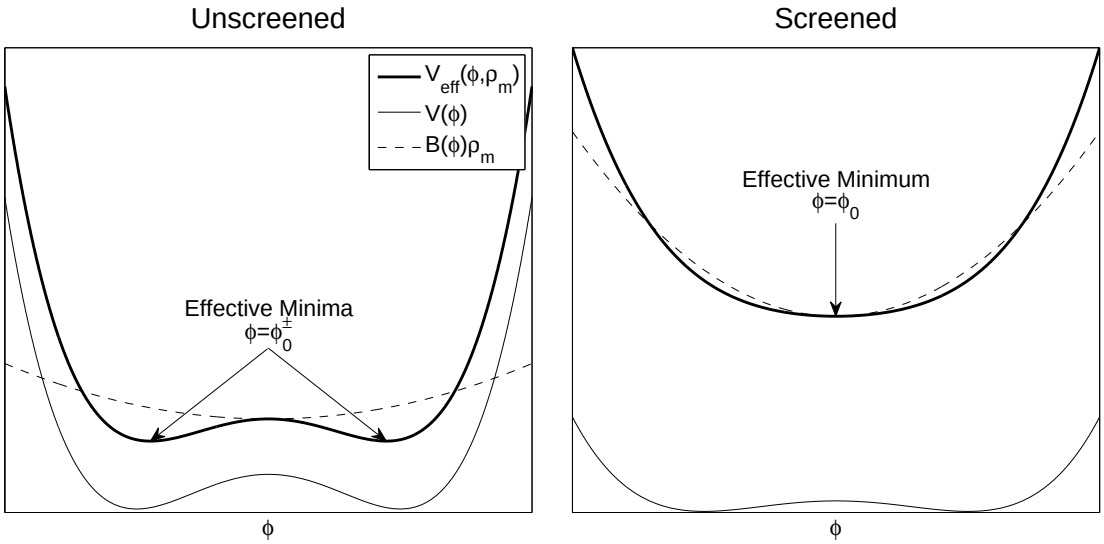

Figure 6.1: Effective symmetron potential in low (left) and high (right) density backgrounds

When $\rho_m > \mu^2$ the quadratic parameter is positive and the minima of the potential is situated at the origin so the conformal coupling vanishes $\delta B = 0$. When $\rho_m < \mu^2$ the quadratic term changes sign and gives rise to two degenerate minima, one of which the field decays into, effectively activating the coupling. Thus with a suitable choice of μ^2 one can turn off the coupling both in the early universe and on small scales. The sudden appearance of two minima also leads to the creation of domain walls [72], which subsequently break down leading to the production of scalar waves.

Chameleon

The chameleon model relies on an entirely different mechanism for screening based on non-linear features in the field profiles associated with extended objects. If the source is sufficiently dense to produce non-linear perturbations in the field, the object develops a thin shell where the field is flat apart from a thin region close to the surface where the field changes rapidly. This leads to a suppression of the chameleon force outside the object

compared to the linear case. A common choice for the conformal coupling and scalar potential are

$$B(\phi) = \exp(2\beta\phi) \approx 2\beta\phi \quad , \quad V(\phi) = M^4 \left(\frac{M}{\phi}\right)^n \tag{6.29}$$

The form of the scalar potential and conformal coupling is not completely fixed in the chameleon model, but the scalar potential should be monotonically decreasing and bounded from below and the conformal coupling should be increasing with ϕ so the effective potential acquires a minimum. The potential chosen here and in the paper is called the Ratra-Peebles potential and originates from models of dynamical dark energy [79]. The resulting equation of motion and effective potential in this case are

$$\nabla_\mu \nabla^\mu \phi = -nM^3 \left(\frac{M}{\phi}\right)^{n+1} + \beta\rho \quad , \quad V_{eff} = M^4 \left(\frac{M}{\phi}\right)^n + \beta\rho\phi \tag{6.30}$$

The first thing we to note is that the density appears as the slope of the potential which ensures that the scalar mass increases with matter density leading to enhanced Yukawa screening in dense regions, see figure 6.2.

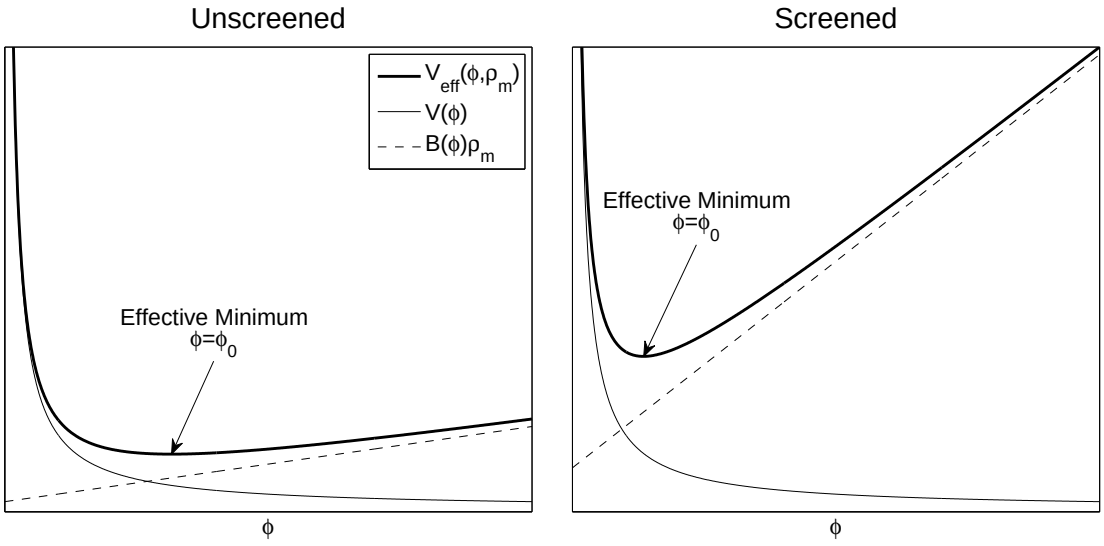

Figure 6.2: Effective chameleon potential in low (left) and high (right) density backgrounds

In addition to the Yukawa screening, there is also a screening mechanism due to non-linear effects when considering extended sources, called the thin shell mechanism [69]. For a source with radius R_s, mass M_s , and a difference between the external and internal minima of the scalar potential $\Delta\phi = \phi_b - \phi_s$, the relative size of the region inside the

source where the scalar field changes rapidly, ΔR, can be approximated by [91][2]

$$\Delta R = \frac{R_s - R_{roll}}{R_s} = \frac{4\pi R_s}{3\beta M_s}\Delta\phi \tag{6.31}$$

where R_roll marks the radial value where the field starts changing. In the case when there is no shell, $\Delta R \gtrsim 1$, the exterior solution for ϕ can be approximated by

$$\phi \approx -\frac{\beta M_s e^{-m_b(r-R_s)}}{4\pi r} + \phi_b \quad , \quad r > R_s \tag{6.32}$$

which is similar to the point source solution 6.25 discussed earlier, with no additional non-linear screening. However when the shell is thin $\Delta R << 1$, the solutions get an additional suppression proportional to ΔR

$$\phi \approx -3\Delta R\frac{\beta M_s e^{-m_b(r-R_s)}}{4\pi r} + \phi_b \quad , \quad r > R_s \tag{6.33}$$

This suppression of the external solution is what is known as the thin shell mechanism, and helps regions of the parameter space evade experimental limits on Yukawa like corrections to Newtons laws from objects with thin shells. Figure 6.3 illustrates the difference between the thick shell and thin shell solutions.

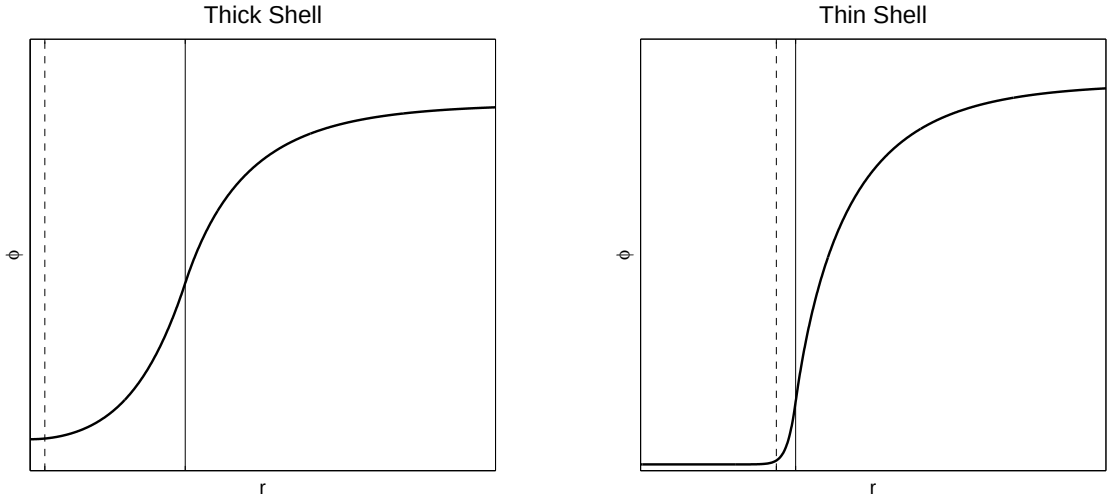

Figure 6.3: Radial profiles for the scalar corresponding to thick (left) and thin (right) shell solutions, where the solid vertical line marks the surface and the dashed vertical line indicates the start of the shell.

[2]We have implicitly assumed that the Compton wavelength of the field outside the source is much larger than the source in order to simplify expressions.

6.5 Dynamical Effects

As we have seen corrections to Newtonian gravity is suppressed in screened modified gravity through the mass term in the linear regime and additional model dependent screening in the non-linear regime. This was based on static approximations, however the real world is dynamic where matter sources move and accelerate relative to each other and evolve with time. In General relativity the effects of such motion on the gravitational degrees of freedom are mostly quasi-static as wave production is highly suppressed due to the conservation of the stress-energy tensor sourcing the Einstein equations. This suppression no longer holds for the additional scalar degree of freedom and one would therefore expect potentially large corrections to the predictions of general relativity in the dynamical regime.

In paper II, "Wave Propagation in Modified Gravity", we extend upon the static analysis presented in this section to include time varying source terms and consider the effects of both mass terms and non-linearities on the resulting perturbations in the scalar field. In particular we find that due to the mass term, the resulting scalar waves will not travel at the speed of light but with a velocity that depends both on the mass of the scalar and and the wavelength. For the non-linear effects we focus on the chameleon model and find that the same mechanism responsible for the thin shell effect also suppresses the amplitude of the scalar waves.

Paper II

Wave Propagation in Modified Gravity

PHYSICAL REVIEW D **93,** 044050 (2016)

Wave propagation in modified gravity

Jan Ø. Lindroos,[1,2,*] Claudio Llinares,[2,3] and David F. Mota[2]

[1]*Institute for Physics and Technology, University of Bergen, N-5020 Bergen, Norway*
[2]*Institute of Theoretical Astrophysics, University of Oslo, N-0315 Oslo, Norway*
[3]*Institute for Computational Cosmology, Department of Physics, Durham University, Durham DH1 3LE, United Kingdom*

(Received 2 December 2015; published 17 February 2016)

We investigate the propagation of scalar waves induced by matter sources in the context of scalar-tensor theories of gravity which include screening mechanisms for the scalar degree of freedom. The usual approach when studying these theories in the nonlinear regime of cosmological perturbations is based on the assumption that scalar waves travel at the speed of light. Within general relativity this approximation is valid and leads to no loss of accuracy in the estimation of observables. We find, however, that mass terms and nonlinearities in the equations of motion lead to propagation and dispersion velocities significantly different from the speed of light. As the group velocity is the one associated with the propagation of signals, a reduction of its value has direct impact on the behavior and dynamics of nonlinear structures within modified gravity theories with screening. For instance, the internal dynamics of galaxies and satellites submerged in large dark matter halos could be affected by the fact that the group velocity is smaller than the speed of light. It is therefore important, within such a framework, to take into account the fact that different parts of a galaxy will see changes in the environment at different times. A full nonstatic analysis may be necessary under those conditions.

DOI: 10.1103/PhysRevD.93.044050

I. INTRODUCTION

Einstein's general theory of relativity is the foundation of our modern description of gravitational phenomena, ranging from stellar evolution and planetary dynamics to the evolution of the Universe itself. However, over the years it has become clear that in order for this theory to explain observations on galactic and cosmological scales, it seems necessary to assume a Universe dominated by dark energy and dark matter, neither of which can be explained within the standard model of particle physics. This has led to a resurgence of interest in modified theories of gravity, in the hope that they might help explain the observed Universe [1]. In this paper we look at one class of such models where an additional scalar degree of freedom is included in the gravitational sector, and the dynamics is governed by the action (1), where the metric signature is chosen to be mostly positive:

$$S = \int \sqrt{-g}\left[\frac{M_{Pl}^2}{2}R - \frac{1}{2}\partial_\mu\phi\partial^\mu\phi - V(\phi)\right]d^4x + \int \mathcal{L}_m[\tilde{g}_{\mu\nu}, \psi]d^4x, \qquad \tilde{g}_{\mu\nu} = B(\phi)g_{\mu\nu}. \tag{1}$$

These models differ from quintessence models by the presence of the conformal coupling to matter $B(\phi)$, which gives rise to an effective potential dependent on the matter distribution. The conformal coupling, which is expected to be of gravitational strength, gives rise to an additional "fifth force," whose existence has been heavily constrained by local tests on deviations from the inverse square law, Casimir forces and violations of the weak equivalence principle [2]. These constraints rule out most such models for natural values of the couplings, unless the fifth forces can be screened in high-density regions where the constraints are most stringent. Models exhibiting such screening are often called screened modified gravity, where the chameleon [3], symmetron [4] and Galileon models [5] are examples. In the chameleon model, the mass of the field depends on the local matter density in such a way that in high-density regions, like on Earth or in the Solar System, it becomes large, leading to a Yukawa-like suppression of the fifth-force range. In low-density regions, on the other hand, the mass of the chameleon is small, allowing long-range fifth forces which can modify the predictions of GR on cosmological scales. In addition to the Yukawa screening, the chameleon model gives rise to additional screening through the so-called thin-shell mechanism, which restricts the fifth forces of objects like the Sun and Earth to thin shells close to the surface [6,7].

Usually the effects of the new scalar degree of freedom are studied in the static or quasistatic limit. However, there is increasing interest in the possibility that scalar waves may yield non-negligible corrections to GR and have to be taken into account when making predictions for some of these theories. Recently N-body simulations taking into account the full dynamical equations of motion for the symmetron model were performed [8,9], showing novel

*jan.lindroos@ift.uib.no

phenomena such as the creation of domain walls and their subsequent breakdown leading to energy release in the form of scalar waves. Nonstatic effects were also studied in the linear and nonlinear regimes in different models in Refs. [10–13]. The waves appearing in the symmetron model were shown to travel at the speed of light in accordance with the notion that the speed of sound equals the speed of light, $c_s = 1$, for scalar fields with canonical kinetic terms [14–16]. However, from the field-theoretic point of view, at least in the linear regime, waves in a massive scalar field originating from a localized source travel with the group velocity $c_g < 1$ [17], contrary to the phase velocity of plane waves in the Fourier expansion, which travel at phase velocities larger than that of light, $c_p > 1$. A similar thing happens when light travels through dispersive media, where the phase velocity can be larger than the speed of light in vacuum, but where the group velocity and the measured speed of light are smaller than the vacuum value. This stems from the fact that waves having a local origin are not described by a single plane-wave mode, but rather by a distribution of modes or a wave packet, which collectively travel at the group velocity. These differences between the speed of propagation of light and the gravitational degrees of freedom may lead to observational consequences. See, for instance, Ref. [18] for some of the consequences of having different horizons for light and gravity.

The concept of group velocity is seldom mentioned in the literature on scalar field cosmology, and there seems to be some confusion as to the meaning of the different concepts of velocity (sound speed c_s, group velocity c_g and phase velocity c_p). In this paper we review the relation between these concepts in the context of linear scalar waves, and investigate how these results carry over into the nonlinear regime and curved spacetime using numerics. As an explicit example we look at the chameleon model, where we throughout assume that the nonminimal coupling in equation (1) can be linearized, $\tilde{g}_{\mu\nu} \approx g_{\mu\nu} + \delta g_{\mu\nu}$ with $\delta g_{\mu\nu} \ll 1$. This allows us to linearize the matter coupling

$$\mathcal{L}_m(\tilde{g}_{\mu\nu}, \psi) \approx \mathcal{L}_m(g_{\mu\nu}, \psi) + \frac{\sqrt{-g}}{2}\delta B(\phi) T^m, \qquad (2)$$

where T^m is the trace of the Einstein frame stress-energy tensor $T^{\mu\nu}_m$ in the absence of scalar couplings:

$$T^m = T^{\mu\nu}_m g_{\mu\nu}, \qquad T^{\mu\nu}_m = \frac{2}{\sqrt{-g}}\frac{\partial \mathcal{L}_m(g_{\mu\nu}, \psi)}{\partial g_{\mu\nu}}. \qquad (3)$$

For the conformal coupling $B(\phi)$ and potential $V(\phi)$ we follow [3]

$$V(\phi) = M^4\left(\frac{M}{\phi}\right)^n, \qquad B(\phi) = e^{2\beta\phi} \approx 1 + 2\beta\phi, \qquad (4)$$

which gives the equation of motion for the scalar field

$$\nabla_\mu \nabla^\mu \phi = S(\phi, T^m) = V(\phi)_{,\phi} - \frac{1}{2}\delta B(\phi)_{,\phi} T^m. \qquad (5)$$

Throughout this paper we focus on perturbations in the scalar field induced by a matter source rather than how matter perturbations are affected by the presence of additional gravitational degrees of freedom. For modifications to the evolution and dynamics of ordinary matter perturbations in modified theories of gravity, see for instance Refs. [19–23].

The paper is structured as follows: In Sec. II we look at the propagation of scalar waves in the linear regime and Minkowski spacetime. We then continue in Sec. III by looking at how this behavior is modified when the nonlinearities are taken into account. This is followed by a brief discussion in Sec. IV on the apparent inconsistency between the group velocity, $c_g \leq 1$, determining the propagation speed of the scalar waves, and the effective speed of sound $c_s = 1$ found in the fluid approach used in perturbation theory. Finally, we summarize and conclude in Sec. V.

II. SCALAR WAVES: LINEAR REGIME

We start by considering the simplest possible scenario, where we assume a Minkowski background, with nonrelativistic matter $T^m \approx -\rho_m$. The matter distribution can then be split into a background and source part, $\rho_m = \rho_0(x^\mu) + \delta\rho(x^\mu)$, where we allow the background to potentially vary in both space and time (e.g. as a time-varying cosmological background, or the static background solution for a spherical source). This can be used to consider linear perturbations over potentially nonlinear backgrounds, although this is beyond the scope of this paper. We can then write the field in terms of a background solution ϕ_0 and a perturbation φ, $\phi = \phi_0(x^\mu) + \varphi(x^\mu)$ which allows us to Taylor-expand the source term $S(\phi, \rho_m)$ in equation (5):

$$S \approx \underbrace{\beta\rho_0 - \frac{nM^{n+4}}{\phi_0^{n+1}}}_{S(\phi_0, -\rho_0)} + \frac{n(n+1)M^{n+4}}{\phi_0^{n+2}}\varphi + \beta\delta\rho. \qquad (6)$$

Using this approximation, the equations of motion for the perturbations φ become

$$(\partial_\mu\partial^\mu - m^2)\varphi = \beta\delta\rho, \qquad m^2 = \frac{n(n+1)M^{n+4}}{\phi_0(x_\mu)^{n+2}}, \qquad (7)$$

where $\phi_0(x^\mu)$ is the solution to the full equations for the background density $\rho_0(x^\mu)$, and the approximation is valid as long as $|\varphi(x^\mu)| \ll \phi_0(x^\mu)$. In this paper we restrict ourselves to a fixed matter background with the background field ϕ_0 situated at the minima of the background

potential. This yields the standard massive Klein-Gordon equation with the background field ϕ_0 given by

$$\phi_0 = \left(\frac{nM^{n+4}}{\beta\rho_0}\right)^{1/(n+1)}, \tag{8}$$

$$m^2 = (n+1)\frac{\beta\rho_0}{\phi_0} \tag{9}$$

From the expression for ϕ_0 we can now estimate what densities justify the linearization of the conformal coupling

$$\phi_0 \ll \frac{1}{2\beta}, \qquad \rho_0 \gg 2nM^4(n\beta M)^n. \tag{10}$$

If we assume natural values for the coupling parameters $\beta \sim 1/M_{Pl}$, $M \sim \rho_\Lambda^{1/4}$ [7], with ρ_Λ being the vacuum energy density, then the ratio $M/M_{Pl} \sim 10^{-30}$, and the approximation is valid for matter densities $\rho_m \gg 10^{-30n}\rho_\Lambda$, which covers most conceivable situations, for $n > 0$.

A. Causality

First, we note that even though the plane-wave solutions of equation (7) can travel at speeds exceeding that of light, the propagation of a signal originating from a localized source is always causal. This can be seen by considering the effect of a source on the future field, where we can write the solution in terms of the retarded Green's function $G_{\rm ret}$ [24], defined in terms of the fundamental equation for the future field:

$$(\partial_\mu\partial^\mu - m^2)G_{\rm ret}(x^\mu, x'^\mu) = \delta^4(x^\mu - x'^\mu),$$
$$\tau = t - t', \qquad \lambda = \tau^2 - |\mathbf{x} - \mathbf{x}'|^2,$$
$$G_{\rm ret}(x^\mu, x'^\mu) = -\frac{\theta(\tau)}{2\pi}\left(\delta(\lambda) - \frac{m\theta(\lambda)J_1(m\sqrt{\lambda})}{2\sqrt{\lambda}}\right). \tag{11}$$

Here $J_\nu(x)$ are the Bessel functions of the first kind, and $\theta(x)$ is the Heaviside step function $\lambda = 0$ that defines the boundary of the future light cone of the source, and we see that outside the light cone, $\lambda < 0$, the Green's function vanishes. The particular solution φ for an arbitrary source $\delta\rho$ can now be constructed by exploiting the linearity of the equation, which allows us to write φ as a weighted superposition of Green's solutions for different δ sources:

$$\varphi = \beta\int \delta\rho(x'^\mu)G_{ret}(x^\mu, x'^\mu)d^4x'. \tag{12}$$

It follows from this form of the solution that the field at a spacetime point (t, x) is only affected by the part of the source inside the past light cone of the spacetime point. This ensures that the propagation of perturbations caused by a localized source is causal and the upper limit for the propagation velocity is the speed of light $c = 1$. As an example, we consider the case of a point particle of unit mass created at the origin at $t = 0$, which we model as a delta source $\delta\rho = \theta(t)\delta^3(\mathbf{x})$, where we assume that the scalar field is initially unperturbed, $\varphi(t = 0, \mathbf{x}) = 0$. The integral form of the solution in terms of the distance from the source r then simplifies to

$$\varphi(t, r) = -\frac{\beta}{4\pi r}\left(1 - mr\int_0^{u_f}\frac{J_1(u)du}{\sqrt{u^2 + m^2r^2}}\right), \tag{13}$$

where $u_f = m\sqrt{t^2 - r^2}$. In the infinite future, the integral simplifies for finite values of r to the standard Yukawa solution for a static δ source, where the negative sign of the solution is a manifestation of the force between equal charges, given by the gradient of the field $F_\varphi \propto -\nabla_r\phi$:

$$\int_0^\infty \frac{J_1(u)}{\sqrt{u^2 + m^2r^2}} = \frac{1 - e^{-mr}}{mr} \Rightarrow \lim_{t\to\infty}\varphi(t, r) = -\beta\frac{e^{-mr}}{4\pi r}. \tag{14}$$

This is as expected, since as $t \to \infty$, the motion created in the field due to the sudden appearance of the particle at $t = 0$ has radiated away to infinity. In the finite case, finding a closed-form solution is difficult, but numerical solutions can be found by solving either the integral equation (12) or the differential equation (5). Figure 1 shows the solutions at time $t = 25$ for a scalar field with mass $m = 1$, obtained using a fourth-order Runge-Kutta solver for Eq. (5) and an adaptive Gauss-Konrod quadrature integral solver [25] for Eq. (12). The light horizon is

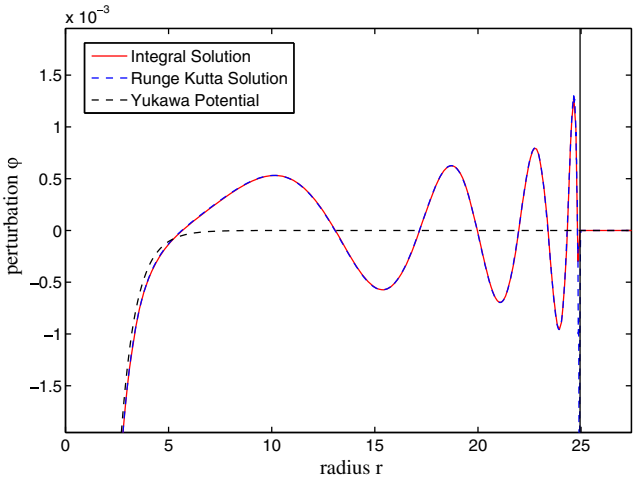

FIG. 1. Perturbations φ in the scalar field at $t = 25$ induced by a static delta source created at the origin at $t = 0$. The dashed blue and red lines correspond to the solutions found by solving the differential (5) and integral (11) equations, respectively. The black vertical line indicates the light horizon, while the dashed black line corresponds to the static Yukawa solution. The length scale is arbitrary and related to the time scale by the speed of light $c = 1$.

indicated by the vertical black line at $r = 25$, after which no perturbations occur in accordance with the vanishing of the Green's function (11) beyond this point.

The sudden introduction of a particle at $t = 0$ creates oscillations in the scalar field, which gradually subsides as the associated energy is radiated away. This leads to a wave pattern outside the source where the perturbations are large and narrow at the wave front and gradually decay and widen in its wake as the central oscillations decay. As the oscillations decay, the solution converges towards the Yukawa solutions (14) as predicted by the analytic solution. In the linear regime, the perturbations in the field are proportional to the size of the matter perturbations and grow without bound, as illustrated by the Yukawa solution. This is not necessarily true in the nonlinear regime, and for chameleon models studied here, the self-coupling diverges as ϕ goes to zero, leading to a positive definite magnitude of the field. This results in a suppression of the scalar wave amplitude in the nonlinear regime, due to smaller gradients in the field. The solutions found using the Runge-Kutta solver agree well with the integral solutions, and serve as a sanity check for the differential solver that will be used for the remainder of the paper.

B. Propagation of a wave packet

The concepts of phase and group velocity relate to the propagation of plane waves and wave packets, respectively. To illustrate the concepts, we consider the background equation ($\delta\rho = 0$) for the perturbations φ in Fourier space

$$\varphi(x^\mu) = \frac{1}{(2\pi)^4}\int \varphi(k^\mu) e^{ik_\mu x^\mu} d^4k, \tag{15}$$

$$\varphi(k^\mu) = \int \varphi(x^\mu) e^{-ik_\mu x^\mu} d^4x, \tag{16}$$

$$k^\mu = (\omega, \mathbf{k}), \tag{17}$$

which gives the Fourier-space algebraic equation for any nonvanishing Fourier component $\varphi_k = \varphi(k^\mu)$:

$$[\omega^2 - (\mathbf{k}^2 + m^2)]\varphi_k = 0 \tag{18}$$

$$\Rightarrow \omega = \sqrt{\mathbf{k}^2 + m^2}. \tag{19}$$

The resulting relation between the frequency ω and the wave vector $\mathbf{k}$ is called the dispersion relation and tells us how the solutions to the equation propagate and disperse. The dispersion relation allows us to write the spacetime Fourier modes in terms of spatial ones:

$$\varphi_k = 2\pi\varphi_{\mathbf{k}}\delta(\omega - \sqrt{\mathbf{k}^2 + m^2}),$$

and to write equation (15) as

$$\varphi(t, \mathbf{x}) = \frac{1}{(2\pi)^3}\int \varphi_{\mathbf{k}} e^{-ik(c_p t - \hat{\mathbf{k}}\cdot\mathbf{x})} d^3\mathbf{k}, \tag{20}$$

where the wave vector is written in terms of its magnitude and directional unit vector $\mathbf{k} = k\hat{\mathbf{k}}$. Equation (20) tells us that the plane wave modes in the Fourier expansion travel with a velocity c_p, called the phase velocity:

$$c_p = \frac{\omega}{k} = \sqrt{1 + m^2/\mathbf{k}^2} > 1. \tag{21}$$

However, the phase velocity describes the propagation of plane waves which are not localized, and hence are different from the waves originating from a source. This is why the phase velocity can be greater than the speed of light without breaking causality. A wave produced by a local source consists of a collection of plane waves, usually referred to as a wave packet, which never exceed the speed of light, as discussed in Sec. II A. If the wave has a well-defined wavelength λ, the propagation velocity can be estimated by considering solutions with $\varphi_{\mathbf{k}}$ sharply peaked around a wave number $k_0 = 1/\lambda$. For simplicity, we consider propagation along one direction, in which case the frequency ω can then be Taylor-expanded around k_0, allowing us to further simplify $\varphi(t, x)$ [26]:

$$\omega(k) \approx \omega(k_0) + \frac{d\omega(k_0)}{dk}\delta k = \omega_0 + c_g(k - k_0), \tag{22}$$

$$\begin{aligned}\varphi(t, x) &= \frac{e^{i[c_g k_0 - \omega_0]t}}{2\pi}\int \varphi_{\mathbf{k}} e^{-ik(c_g t - x)} dk \\ &= \varphi_0(x - c_g t) e^{i\theta_0 t}, \quad \theta_0 = c_g k_0 - \omega_0.\end{aligned} \tag{23}$$

As can be seen from equation (23), the wave packet travels undistorted up to a global phase factor θ_0 with a velocity c_g as long as higher-order terms in the frequency expansion are neglected. The velocity c_g is what is called the group velocity and is given by

$$c_g = \frac{d\omega}{dk} = \frac{1}{\sqrt{1 + \frac{m^2}{k^2}}} < 1. \tag{24}$$

Contrary to the phase velocity, this is always smaller than the speed of light. To illustrate we consider a one-dimensional oscillating Gaussian matter perturbation $\delta\rho$ oscillating with a frequency ω_m:

$$\delta\rho = \frac{1}{2}\delta\rho_0(x)(1 - \cos(\omega_m t)), \tag{25}$$

$$\delta\rho_0(x) = Me^{-\frac{x^2}{2\sigma^2}}, \quad \sigma = 0.1. \tag{26}$$

The particular solution to the one-dimensional equation in Fourier space is then given by

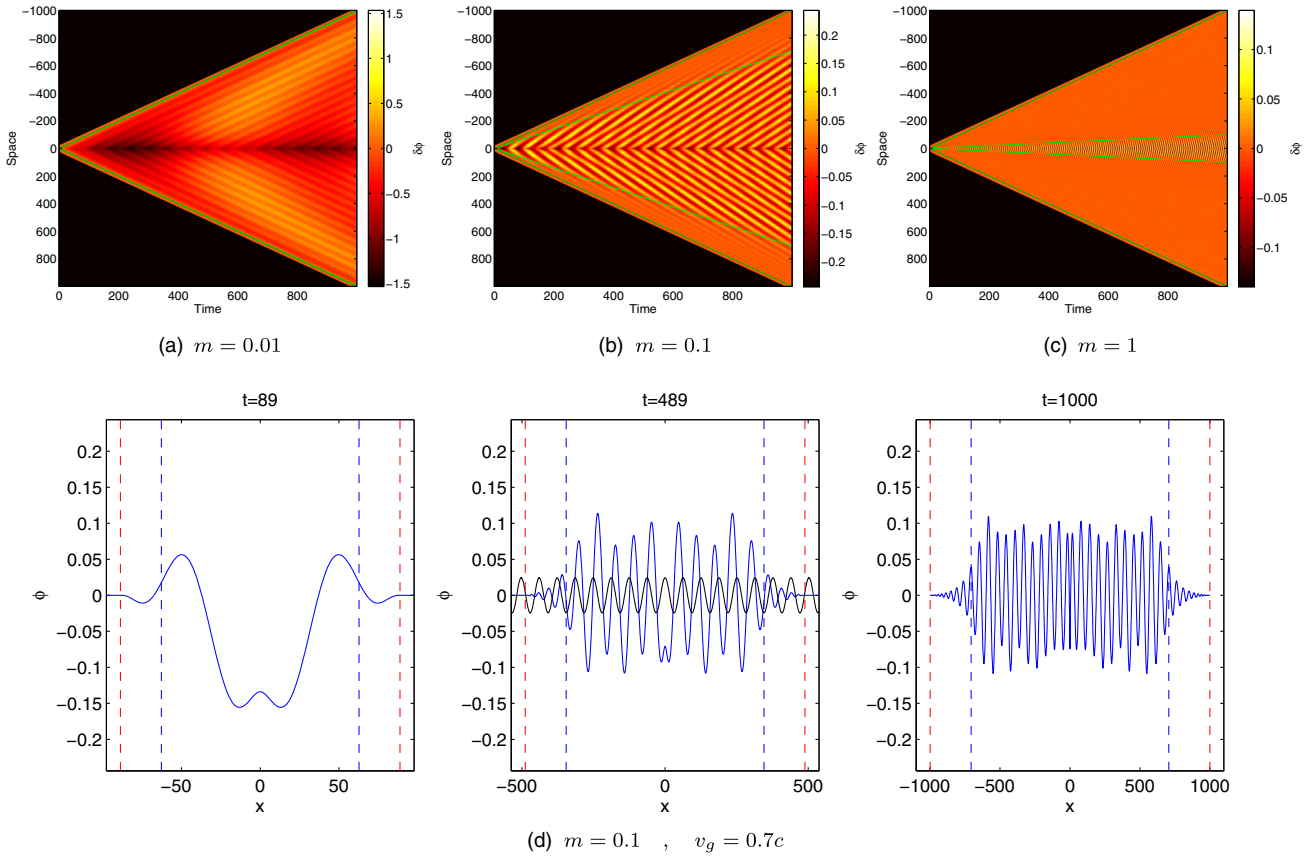

FIG. 2. Plots (a), (b) and (c) show the propagation of waves from a source for three different scalar masses, represented in terms of light-cone plots. The lines indicate the light cone (dark green, wide angle) and the "sound" cone (light green, small angle) indicating the front of the main signal as determined by the group velocity. The unperturbed regions are colored in black for clarity. Plot (d) shows the corresponding scalar field profile for $m = 0.1$ at three different times, where the plane wave $\sin(k_0 x)$ is included for comparison in the middle plot. The blue and red vertical dashed lines show the light horizon and the horizon given by the group velocity.

$$\varphi_{\mathbf{k}} = -\frac{\beta}{2}\delta\rho_{k0}\left[\frac{\cos(\omega_m t)}{\omega_m^2 - \omega_k^2} + \omega_m^{-1}\right], \tag{27}$$

where ω_k is the frequency associated with $\mathbf{k}$ through the dispersion relation (19). By choosing an oscillation frequency $\omega_m = \sqrt{k_0^2 + m^2}$, the source induces perturbations in φ dominated by k_0. Figure 2 shows the evolution of the scalar field in a similar fashion as in Ref. [8], for three different scalar masses $m = [0.01, 0.1, 1]$, $\beta = 1$ and $k_0 = M = 0.1$, in addition to the profile for $m = 0.1$ at three different times. The unperturbed regions in the light-cone plots are colored in black for clarity.

The solutions show the main component of the wave traveling at the group velocity, and a rapid decay of the solution in front. The small high-frequency oscillations in front of the main signal are called precursors and are a well-known phenomena from light propagation in dispersive media [27,28]. These precursors are generally much smaller than the main signal. The same behavior is also observed for a spherically symmetric source, except for an additional $1/r$ decay of the amplitude, as we will see when we solve the full equations in Sec. III.

Including higher-order terms in the frequency expansion in equation (22) leads to dispersion and amplitude evolution. In particular, we can get an approximate expression for the dispersion rate (i.e. how fast the wave packet spreads) by including the second-order term in the expansion. Let us consider, for example, a spherically symmetric perturbation at rest with an initial width $\sigma(t = 0) = \sigma_0$:

$$\varphi(0, r) = (2\pi\sigma_0^2)^{-3/2} e^{-\frac{r^2}{2\sigma_0^2}}. \tag{28}$$

The Fourier transform of the initial distribution is then given by

$$\varphi_{\mathbf{k}} = e^{-\frac{k^2\sigma_0^2}{2}}, \tag{29}$$

and the spacetime solution $\varphi(t, r)$ written in terms of the Fourier modes in spherical coordinates becomes

$$\varphi(t, r) = \frac{1}{2\pi^2 r}\int_0^\infty k \sin(kr) e^{-(\frac{1}{2}k^2\sigma_0^2 + i\omega(k)t)} dk. \tag{30}$$

Continuing the Taylor expansion of the frequency to second order around $k_0 = 0$, using $\omega_0 = \omega(k_0) = m$ and $c_g(0) = 0$ gives

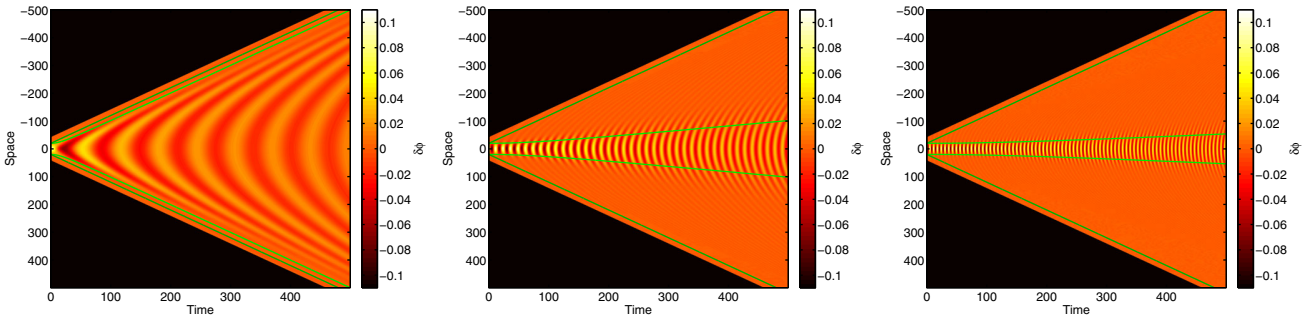

FIG. 3. The spread of a Gaussian perturbation with initial spread $\sigma_0 = 10$ for masses $m = 0.1$ (a), 0.5 (b), and 1 (c). The lines indicate the paths of light rays originating from $x_c(t) = \pm(2\sigma_0 + ct)$ (dark green, wide angle) and the spread $\pm 2\sigma(t)$ (light green, small angle).

$$\omega(k) \approx \omega_0 + \frac{d\omega_0}{dk}k + \frac{1}{2}\frac{d^2\omega_0}{dk^2}k^2 = m + \frac{k^2}{2m}, \quad (31)$$

$$\varphi(t,r) \approx \frac{e^{-imt}}{2\pi^2 r}\int_0^\infty k\sin(kr)e^{-\frac{1}{2}(\sigma_0^2+\frac{it}{m})k^2}dk = \alpha(t)e^{-i\theta(r,t)}(2\pi\sigma_0)^{-3/2}e^{-\frac{r^2}{2\sigma(t)^2}}, \quad (32)$$

where the spread $\sigma(t)$, amplitude $\alpha(t)$, and phase factor $\theta(r,t)$ are given by

$$\sigma(t) = \sqrt{\sigma_0^2 + \frac{t^2}{m^2\sigma_0^2}}, \qquad \alpha(t) = \left(1 + \frac{t^2}{m^2\sigma^4}\right)^{-3/4}, \quad (33)$$

$$\theta(r,t) = \frac{mt}{2}\left[2 - \frac{r^2}{(t^2 + m^2\sigma_0^4)}\right] + \frac{3}{2}\arg\left[\sigma_0^2 + \frac{it}{m}\right]. \quad (34)$$

For the series expansion to be valid, the wave number must be much smaller than the mass of the field, $k \ll m$, so the approximation is only valid for perturbations much larger than the Compton wavelength of the field, $\sigma_0 \gg m^{-1}$. The rate of change in the spread is given by

$$c_\sigma = \frac{d\sigma}{dt} = \frac{1}{m\sigma_0\sqrt{1 + m^2\sigma_0^4/t^2}}, \quad (35)$$

which converges towards $c_\sigma = (m\sigma_0)^{-1} = \sigma_k/m$ as $t \to \infty$. We note that for the region of validity of the approximation, the spread velocity is always smaller than the speed of light, $v_\sigma < 1$, and is proportional to the mass of the scalar field and the width of the original perturbation.

Figure 3 shows light-cone plots for the evolution of a Gaussian perturbation with initial spread $\sigma_0 = 10$ for three different scalar masses $m \in 0.1, 0.5, 1$ as given by (7) with $\delta\rho = 0$. Though we have shown it here only for a Gaussian initial distribution, a similar behavior applies to more general distributions.

III. NONLINEAR REGIME

A. Nonlinear: One-dimensional

We now continue by solving the full nonlinear equations numerically to see how the nonlinearities affect the propagation of waves that originate from a harmonically oscillating source. Again we consider a Gaussian source $\delta\rho$ embedded in a homogeneous background ρ_0, where we denote the associated background value for the field by ϕ_0. We can then write the full equations of motion in terms of the dimensionless quantities $\chi = \phi/\phi_0 = 1 + \delta\chi$ and $\eta = \rho/\rho_0 = 1 + \delta\eta$ as

$$\nabla_\mu\nabla^\mu\chi = \frac{m^2}{n+1}(\eta - \chi^{-(n+1)}), \quad (36)$$

$$(\nabla_\mu\nabla^\mu - m^2)\delta\chi = \frac{m^2}{n+1}\delta\eta, \quad \delta\chi \ll 1. \quad (37)$$

The linear approximation is valid for $|\varphi| \ll \phi_0$, which is equivalent to $|\delta\chi| \ll 1$. We can use the scaling property of the linear solution, namely that scaling the magnitude of the source corresponds to an equal scaling in the amplitude of the solution, to estimate where the linear approximation breaks down. The amplitude of the solution to equation (7) for $m = M = k_0 = 0.1$ and $\beta = 1$ is roughly $\varphi \sim 0.1$, so in order to generate amplitudes $\varphi \sim 1$, we would need $\beta M \sim 1$. In terms of the new parametrization (37) using $m = 0.1$, $n = 1$ and a source $\delta\eta$ given by

$$\delta\eta = \frac{1}{2}\delta\eta_0(x)(1 - \cos(\omega_m t)), \quad (38)$$

$$\delta\eta_0(x) = Me^{-\frac{x^2}{2\sigma^2}}, \quad \sigma = 0.1, \quad (39)$$

this translates into a source amplitude of order $M \sim 200$. Figure 4 shows the solutions for three different density contrasts $M = 100, 250, 500$.

We clearly see that as the linear approximation breaks down, the simple oscillations in the source term no longer

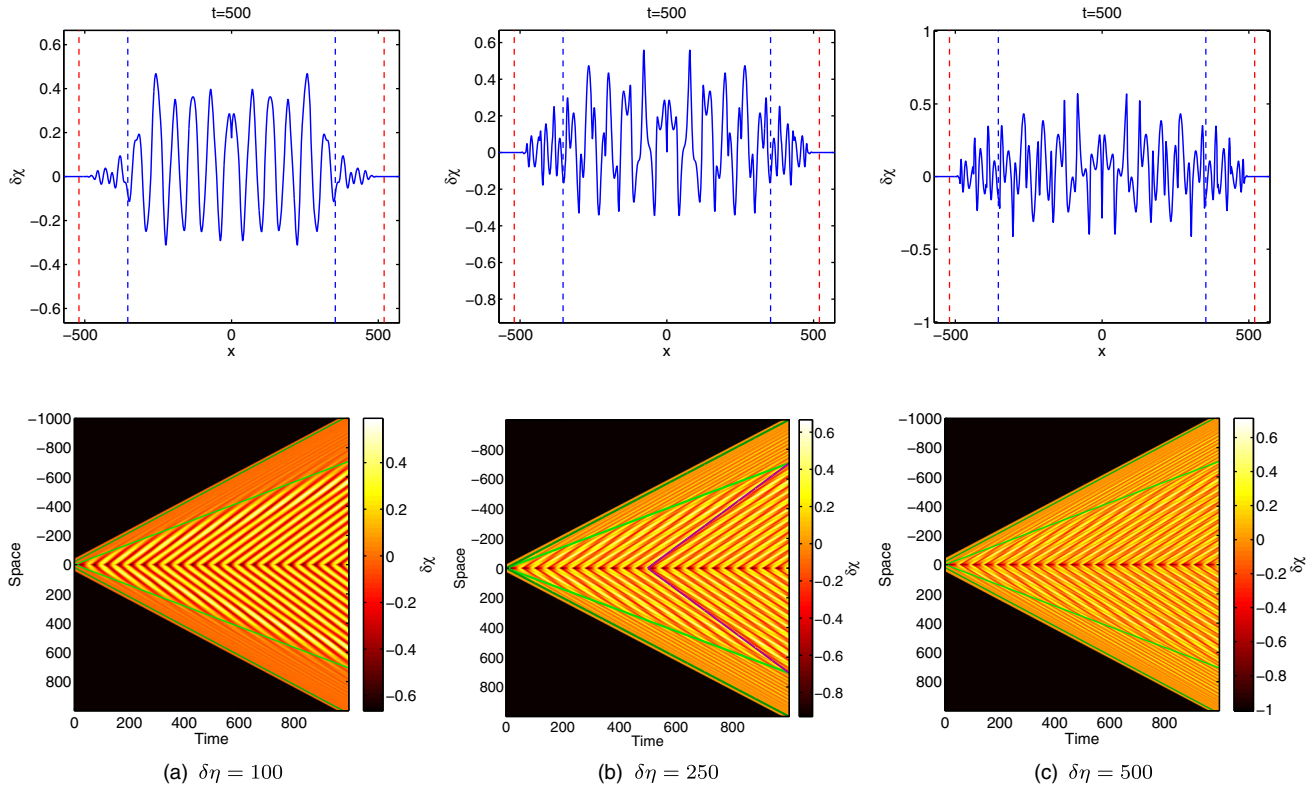

FIG. 4. Nonlinear effects on the waves induced by a one-dimensional oscillating source for three different density contrasts $\delta\eta = 100$ (a), 250 (b), and 500 (c). The upper plots show a snapshot of the profile at $t = 500$, while the lower plots show the corresponding light-cone plots with the light and group velocity horizons marked in light and dark green, respectively. The middle plot also shows the phase velocity associated with the dominant plane-wave mode of the matter source, marked in purple.

give a simple signal, but give rise to complicated waveforms. We also see that the growth of the amplitudes associated with an increased density contrast is highly suppressed due to the bounds on the central oscillations discussed at the end of Sec. II A. Furthermore, as the nonlinearities grow, the decay of the solutions in front of the horizon associated with the group velocity becomes less evident, and the collective propagation becomes more lightlike. However, from the light-cone plots, we still see a rather distinct change in the waveform at the horizon where the main line feature, corresponding to the peaks and troughs of the perturbations, decays rapidly. The motion of these peaks and troughs corresponds to the dominant plane-wave mode of the signal, directly related to the main Fourier mode of the source given by equation (27). As can be seen from the lower middle plot in Fig. 4, the slopes of these peaks and troughs are given by the phase velocity

$$c_p^m = \frac{\omega_m}{k_0} = \sqrt{2}. \tag{40}$$

While the amplitude of the waves is greatly suppressed by the nonlinearities, the main wave mode associated with the oscillation frequency of the source still travels at the group velocity.

B. Nonlinear: Spherically symmetric oscillator

We now go on to consider a slightly more realistic scenario by looking at oscillations in a spherically symmetric object, where we continue to use (37) to model the matter perturbation, but with x replaced by a radial coordinate r. For a similar scenario, but with a radially pulsating source, see Ref. [29]. In the case of three spatial dimensions, the perturbations in the field are similar to the one-dimensional case except for a decay outside the source inversely proportional to the radius. This is expected, as the quantity $u = r\delta\chi$ obeys exactly the same background equations as the one-dimensional field. We also find that much larger matter perturbations are needed in order to produce sufficiently large fluctuations in the scalar field for the nonlinearities to become apparent. Figure 5 shows the scalar perturbations for three different source amplitudes, $M = [1, 5, 10] \times 10^4$, and only the latter two cases show signs of nonlinearities in the waveforms. In all three cases, the propagation of the waves is in good agreement with that predicted by the group velocity, given by equation (24).

C. Realistic wave sources

The sources considered in this paper are highly contrived, as our main focus for this paper is on the propagation

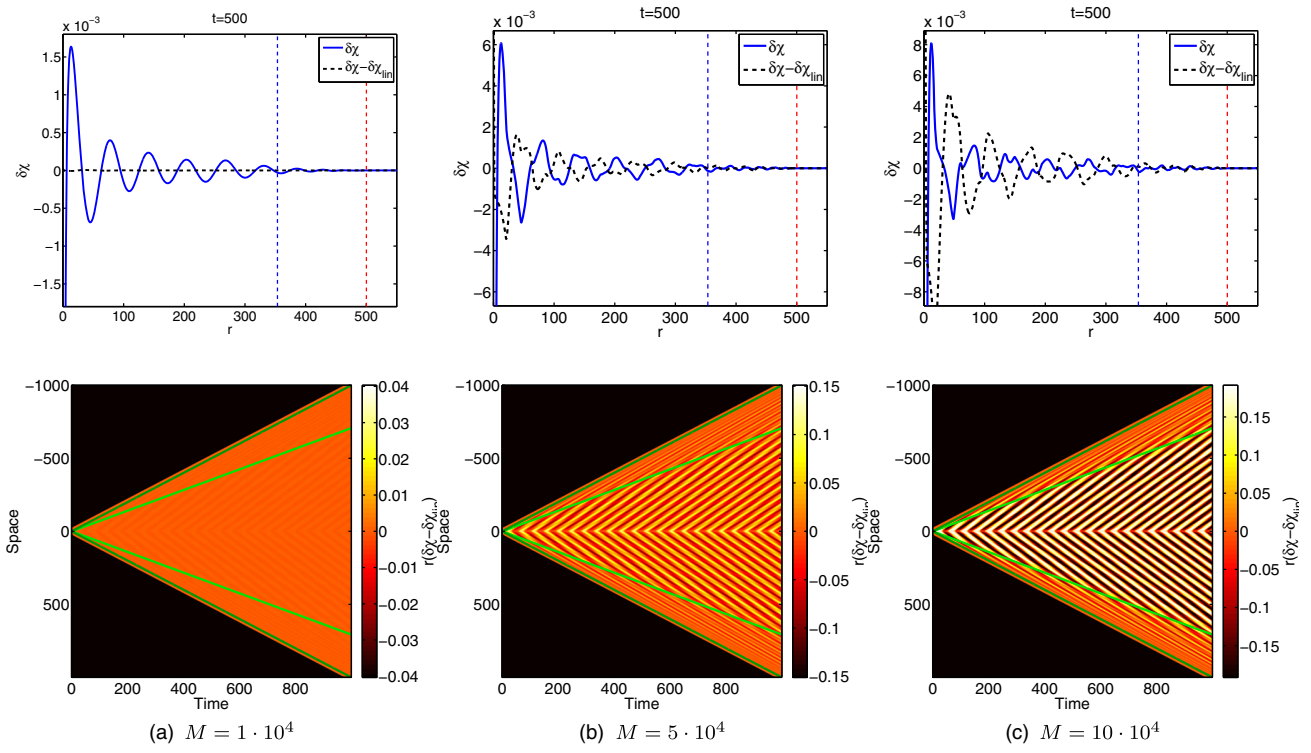

FIG. 5. Nonlinear effects on the waves induced by a spherically symmetric oscillating source for three different density contrasts $M = 1 \times 10^4$ (a), 5×10^4 (b), and 10×10^4 (c). The upper plots show a snapshot of the nonlinear solution at $t = 500$, together with the deviation from the linear solution. The lower plots show the corresponding light-cone plots for the nonlinear deviations, $r(\delta\chi - \delta\chi_{\rm lin})$, scaled by the radius in order to properly see the horizon. The light and group velocity horizons marked in light and dark green, respectively.

of scalar waves and not their generation. There are, however, a few realistic scenarios that can lead to the production of such scalar waves. For one, they can be produced through the motion of matter sources, which induces changes in the associated scalar field profile. This motion would have to be accelerated, since we are dealing with a scalar field which is invariant under Lorentz transformation [30]. An observer seeing a source moving uniformly relative to him would see the associated field profile move with the source without the production of any waves as long as the field is static in the rest frame of the source. However, the orbital motion of planets and stars would create disturbances in the field, as would collisions between objects. In particular, binary pulsars have long been promising sources for ordinary gravitational waves, as they produce gravitational quadrupole radiation. This is also the case for the additional scalar degree of freedom [31,32], but unlike ordinary gravity, there is also the possibility for producing dipole radiation, since the scalar couples to the trace of the stress-energy tensor T^m rather than $T^m_{\mu\nu}$, thereby relieving it of the restrictions coming from conservation of energy and momentum. The potential for probing scalar-tensor theories of gravity through dipole radiation has been studied in, for instance, Refs. [33,34].

The other potential source of radiation, and more directly related to the toy models studied in this paper, is the creation of scalar waves through time variations in the trace of the stress-energy tensor of a matter source. This can occur either through time variations in the spatial distribution of the matter source or through conversion between nonrelativistic and relativistic matter, which leads to changes in the trace T_m. Supernovae are obvious candidates for such sources, where a considerable fraction of the energy density of the initial star is converted into radiation over a short period of time, thus reducing the amplitude of the source as seen by the scalar field and subsequently producing scalar waves. This process would also be more or less spherically symmetric, leading to monopole radiation as in our toy model, though without the periodic oscillations. Other potential sources for monopole radiation include spherical collapse, where waves are created by the changing shape of the source distribution, and variable stars, which might also give rise to periodic oscillations with a more or less well-defined wave number and group velocity. For constraints on screened modified gravity from monopole radiation, see for instance Ref. [35].

Finally, in certain models it is possible to generate cosmological scalar waves when phase transitions occur. This was shown using N-body simulations in Ref. [8] in the context of the symmetron model. In this particular model a phase transition takes place close to redshift zero, when a certain symmetry is broken and the scalar field suddenly

changes its value from 0 to 1. This sudden change gives a kick to the scalar field which is not homogeneous in space, thus producing scalar waves. In a disformally coupled version of this model, in which the speed of sound decreases in high-density regions [36], these waves were found to pile up inside dark matter halos. The determination of observational consequences of such effects is a work in progress.

Regarding simulations, the fact that the speed of sound of scalar fields decreases with mass may be of crucial importance when working on high-resolution regions. The reason for this is that in theories that include screening mechanisms, scalar fields typically become massive when the density increases (i.e. in the center of the dark matter halos). While quasistatic simulations are likely to give inaccurate results under these conditions, it is also important to keep in mind that in these high-density regions, the scalar fields will be screened, and thus there will be no measurable modified gravity effects in the quasistatic regime. Experiments similar to those presented in Ref. [9], but with higher resolution, are necessary to fully understand if the screening will cancel the dynamical effects associated with the low speed of sound. A failure of the quasistatic approximation inside dark matter halos should not be considered as a problem, but as an opportunity to find new observables that might provide a unique signature of modified gravity. The modeling of the collision between two galaxies provides one scenario where dynamical effects might be important. In such a collision, the matter distribution will suddenly change its trajectory, leading to a displacement between the perturbations in the matter distribution and the scalar field. If the speed of sound is small, a part of the original perturbation in the scalar field is expected to continue along the original trajectory of the galaxies undistorted up to a phase; see Fig. 3. Such effects can only be confirmed through high-resolution N-body simulations.

IV. ON THE EFFECTIVE SPEED OF SOUND

Finally, we briefly comment on the relation between the group velocity c_g, describing the propagation of linear waves in the scalar field, and the speed of sound c_s appearing in the perfect fluid description of the scalar field in cosmological perturbation theory. Einstein's equations are sourced by the energy-momentum tensor $T_{\mu\nu}$, which for a canonical scalar field takes the form

$$T_{\mu\nu} = \partial_\mu\phi\partial_\nu\phi - g_{\mu\nu}(\partial^\mu\phi\partial_\mu\phi + V(\phi)). \tag{41}$$

This can be written in perfect fluid form by associating a rest frame energy density ρ_ϕ and pressure p_ϕ, and a fluid four-velocity U_μ with the scalar field,

$$U_\mu \equiv \frac{\partial_\mu\phi}{|\partial^\alpha\phi\partial_\alpha\phi|^{1/2}}, \tag{42}$$

$$\rho_\phi \equiv -\frac{1}{2}\partial^\alpha\phi\partial_\alpha\phi + V(\phi), \tag{43}$$

$$p_\phi \equiv -\frac{1}{2}\partial^\alpha\phi\partial_\alpha\phi - V(\phi), \tag{44}$$

so that $T_{\mu\nu}$ takes the form

$$T_{\mu\nu} = (\rho_\phi + p_\phi)U_\mu U_\nu + p_\phi g_{\mu\nu}. \tag{45}$$

By considering perturbations to the energy density and pressure, $\delta\rho_\phi$ and δp_ϕ, and to the cosmological FLRW background evolution, one finds that the clustering of the scalar fluid is determined by an effective speed of sound c_s [14]:

$$c_s^2 = \frac{\partial_X p_\phi}{\partial_X \rho_\phi}, \qquad X = \frac{1}{2}\partial_\mu\phi\partial^\mu\phi. \tag{46}$$

For a scalar field with a canonical kinetic term, the effective speed of sound is equal to the speed of light, preventing the field from clustering inside the horizon [15]. Since the speed of sound determines how small perturbations in a fluid propagate, this is sometimes taken to mean that perturbations in a canonical scalar field always propagate at the speed of light. However, the speed of sound as defined in (46) refers to the propagation of perturbations in the energy density and pressure as seen from the fluid rest frame, defined as the frame where spatial variations in the scalar field vanish $\partial_i\phi = 0$. This is clearly not the case in the rest frame of the matter source, which is what we are considering here.

The perfect fluid description also puts constraints on the allowed dynamics of the scalar field. In particular, the gradients of the field are constrained by the requirement that U^μ be a proper four-velocity [37]:

$$U_\mu U^\mu = -1, \qquad U_0 > 0. \tag{47}$$

This implies that the derivatives of the scalar field must be nonvanishing $|\partial_\mu\phi| > 0$, and that the time derivative of the field $\dot{\phi}$ cannot change sign. None of these conditions are satisfied for the simple static background approximation we have employed in studying the propagation of perturbations in the field. In addition, as already mentioned, the speed of sound is defined with respect to the rest frame of the scalar fluid, which is a natural reference frame when the only degrees of freedom are the metric and the scalar field, but not when considering scalar waves induced by a matter source, where the natural frame is the matter rest frame. In this frame the scalar fluid has a nonvanishing four-velocity, and hence the flow of energy and momentum is different from that of the scalar field reference frame. For example, the energy density $\tilde{\rho}_\phi$ as seen by an observer moving with a four-velocity U_μ relative to the scalar fluid is given by

$$\tilde{\rho}_\phi = T_{\mu\nu} U^\mu U^\nu, \tag{48}$$

which means that in the matter rest frame, energy propagates as a combination of sound waves with respect to the fluid rest frame and through the flow of the fluid itself. In fact, in Ref. [38], the authors consider a classical scalar field coupled to gravity and find an effective speed of sound

$$c_s^2 = \frac{\delta p}{\delta \rho} \approx \frac{k^2}{4m_\phi^2}. \tag{49}$$

This is similar to the limiting spread velocity c_σ for a Gaussian distribution discussed in Sec. II A, since the spread of a Gaussian in real space is the inverse of the spread in Fourier space, $\sigma_0 = \sigma_k^{-1}$. Much more detailed accounts regarding the correspondence between a perfect fluid and a scalar field can be found in the literature (see e.g. Ref. [39]); we simply note that the speed of sound appearing in the fluid description and the group velocity associated with the propagation of scalar waves are different concepts and should not be confused.

V. SUMMARY AND CONCLUSIONS

We have looked at the propagation of scalar waves induced by matter sources in the context of modified theories of gravity which include screening mechanisms. The usual approach when studying these theories in the nonlinear regime of cosmological perturbations is based on the assumption that scalar waves travel at the speed of light. Within the context of standard gravity, it has been shown that in this case the speed can be approximated by infinity without loss of accuracy in the estimation of observables [40,41]. However, there is no study within modified gravity that supports this idea. Here we review the concepts of phase and group velocity in the context of modified gravity and find that mass terms and nonlinearities in the equations of motion can lead to propagation and dispersion velocities significantly different from the speed of light, contrary to usual beliefs.

The origin of the assumption of lightlike propagation for the additional scalar degree of freedom seems to originate from the speed of sound being equal to the speed of light in the perfect fluid approximation of the scalar field often used in cosmological perturbation theory. We point out that the necessary conditions for this approximation to be valid break down when considering scalar waves induced by matter sources, and that the propagation of these waves is best described by the group velocity. As the group velocity is the one associated with the propagation of signals, a reduction of its value will have direct impact on the behavior of these theories.

On cosmological scales, the background matter density and perturbations are small and slowly varying. For the class of models studied in this paper, the scalar becomes very light and the large-scale perturbations in the field will be linear for reasonable choices of model parameters. We therefore expect the assumption of lightlike propagation to be valid in this regime. We stress that this expectation only applies to models whose equation of motion reduces to the Klein-Gordon equation (7) in the linear regime, and does not extend to, for instance, models with noncanonical kinetic terms. On the other hand, the internal dynamics of galaxies and satellites submerged in large dark matter halos could be affected by the fact that the group velocity is small. In these cases, it will be necessary to take into account the fact that different parts of a galaxy will see changes in the environment at different times (i.e., a full nonstatic analysis should be made). Full 3D high-resolution simulations are required to measure the impact of this phenomenon in more realistic scenarios.

Furthermore, we consider a possible link between gravitational clustering of canonical scalar fields and the dispersion rate of perturbations in the field. We find that this rate is closely related to the speed of sound related to the time-averaged energy density and pressure of spatially localized scalar perturbations. Establishing whether this spread velocity is directly related to the Jeans length of the field requires the inclusion of gravitational effects on the perturbations which are beyond the scope of this paper.

Finally, we found that nonlinear terms in the equations of motion for the scalar field induce small-scale oscillations superimposed on the main waves generated by the source. Furthermore, these nonlinearities can reduce the amplitude of the oscillations compared to the linear case. Despite this, we find that the propagation speed of the main waves is still described by the group velocity. This constitutes a characteristic signature of modified gravity which could be potentially observed with future gravitational wave experiments (e.g. LISA). It is important to note that this observable is not degenerate with other effects. This differentiates it from other observables such as the power spectrum of cosmological density perturbations, for which the modified gravity signals are degenerated with the effects of baryons and neutrinos. Targeted studies on specific astrophysical objects should be made to predict the amplitude of these waves under realistic situations.

Our study is focused on a particular set of models where the matter coupling is conformal, but considering that models with more exotic matter couplings usually lead to considerable reductions in the speed of sound already in the perfect fluid approximation, the results are expected to be more general. More studies are required before having a complete picture of the problem and the validity of small-scale cosmological simulations. While the results found in this paper seem to constitute a problem for the community of simulations, we should look at the bright side and keep in mind that this new effect could lead to a completely new set of observables that can be used to test these theories for gravity.

ACKNOWLEDGMENTS

D. F. M. acknowledges funding from the Research Council of Norway and the use of computing facilities of the NOTUR cluster HEXAGON. C. L. L. acknowledges support from the Research Council of Norway through Grant No. 216756 and from STFC consolidated Grant No. ST/L00075X/1. J. Ø. L. acknowledges support from the Centre for Dark Matter Research (DAMARA) at the Department of Physics and Technology, University of Bergen, funded by the Bergen Research Foundation, the University of Bergen, and the Norwegian Research Council.

[1] T. Clifton, P. G. Ferreira, A. Padilla, and C. Skordis, Phys. Rep. **513**, 1 (2012).
[2] V. M. Mostepanenko, R. S. Decca, E. Fischbach, G. L. Klimchitskaya, D. E. Krause, and D. López, J. Phys. A **41**, 164054 (2008).
[3] J. Khoury and A. Weltman, Phys. Rev. Lett. **93**, 171104 (2004).
[4] K. Hinterbichler and J. Khoury, Phys. Rev. Lett. **104**, 231301 (2010).
[5] A. Nicolis, R. Rattazzi, and E. Trincherini, Phys. Rev. D **79**, 064036 (2009).
[6] J. Khoury, arXiv:1011.5909.
[7] D. F. Mota and D. J. Shaw, Phys. Rev. D **75**, 063501 (2007).
[8] C. Llinares and D. Mota, Phys. Rev. Lett. **110**, 161101 (2013).
[9] C. Llinares and D. F. Mota, Phys. Rev. D **89**, 084023 (2014).
[10] J. Noller, F. von Braun-Bates, and P. G. Ferreira, Phys. Rev. D **89**, 023521 (2014).
[11] S. Bose, W. A. Hellwing, and B. Li, J. Cosmol. Astropart. Phys. 02 (2015) 034.
[12] D. F. Mota, D. J. Shaw, and J. Silk, Astrophys. J. **675**, 29 (2008).
[13] H. A. Winther and P. G. Ferreira, Phys. Rev. D **92**, 064005 (2015).
[14] J. Garriga and V. F. Mukhanov, Phys. Lett. B **458**, 219 (1999).
[15] D. Bertacca, N. Bartolo, and S. Matarrese, Adv. Astron. **2010**, 904379 (2010).
[16] B. Li, D. F. Mota, and J. D. Barrow, Astrophys. J. **728**, 109 (2011).
[17] G. Whitham, *Linear and Nonlinear Waves*, Pure and Applied Mathematics: A Wiley Series of Texts, Monographs and Tracts (Wiley, New York, 2011).
[18] I. Sawicki and E. Bellini, Phys. Rev. D **92**, 084061 (2015).
[19] M. Roshan and S. Abbassi, Phys. Rev. D **90**, 044010 (2014).
[20] M. Roshan and S. Abbassi, Astrophys. J. **802**, 9 (2015).
[21] M. Zumalacarregui, T. S. Koivisto, and D. F. Mota, Phys. Rev. D **87**, 083010 (2013).
[22] C. G. Boehmer, J. Burnett, D. F. Mota, and D. J. Shaw, J. High Energy Phys. 07 (2010) 053.
[23] M. Roshan and S. Abbassi, Astrophys. Space Sci. **358**, 11 (2015).
[24] N. N. Bogoliubov and D. V. Shirkov, *Introduction to the Theory of Quantized Fields* (Interscience, New York, 1959).
[25] L. Shampine, J. Comput. Appl. Math. **211**, 131 (2008).
[26] J. D. Jackson, *Classical Electrodynamics*, 3rd ed. (Wiley, New York, 1998).
[27] L. Brillouin, Ann. Phys. (Berlin) **349**, 203 (1914).
[28] A. Sommerfeld, Ann. Phys. (Berlin) **349**, 177 (1914).
[29] A. Silvestri, Phys. Rev. Lett. **106**, 251101 (2011).
[30] R. Cawley and E. Marx, Int. J. Theor. Phys. **1**, 153 (1968).
[31] C. de Rham, A. Matas, and A. J. Tolley, Phys. Rev. D **87**, 064024 (2013).
[32] P. Brax, A.-C. Davis, and J. Sakstein, Classical Quantum Gravity **31**, 225001 (2014).
[33] P. C. C. Freire, N. Wex, G. Esposito-Farese, J. P. W. Verbiest, M. Bailes, B. A. Jacoby, M. Kramer, I. H. Stairs, J. Antoniadis, and G. H. Janssen, Mon. Not. R. Astron. Soc. **423**, 3328 (2012).
[34] D. E. Krause, H. T. Kloor, and E. Fischbach, Phys. Rev. D **49**, 6892 (1994).
[35] A. Upadhye and J. H. Steffen, arXiv:1306.6113.
[36] R. Hagala, C. Llinares, and D. F. Mota, Astron. Astrophys. **585**, A37 (2016).
[37] I. Sawicki, I. D. Saltas, L. Amendola, and M. Kunz, J. Cosmol. Astropart. Phys. 01 (2013) 004.
[38] W. Hu, R. Barkana, and A. Gruzinov, Phys. Rev. Lett. **85**, 1158 (2000).
[39] N. Bilic, G. B. Tupper, and R. D. Viollier, Phys. Rev. D **80**, 023515 (2009).
[40] N. E. Chisari and M. Zaldarriaga, Phys. Rev. D **83**, 123505 (2011).
[41] S. R. Green and R. M. Wald, Phys. Rev. D **85**, 063512 (2012).

Bibliography

[1] Combination of higgs boson searches with up to 4.9 fb-1 of pp collisions data taken at a center-of-mass energy of 7 tev with the atlas experiment at the lhc. Technical Report ATLAS-CONF-2011-163, CERN, Geneva, Dec 2011.

[2] Search for squarks and gluinos with the ATLAS detector using final states with jets and missing transverse momentum and 5.8 fb^{-1} of $\sqrt{s}$=8 TeV proton-proton collision data. Technical Report ATLAS-CONF-2012-109, CERN, Geneva, Aug 2012.

[3] Search for supersymmetry in events with large missing transverse momentum, jets, and at least one tau lepton in 21 fb^{-1} of $\sqrt{s} = 8$ tev proton-proton collision data with the atlas detector. Technical Report ATLAS-CONF-2013-026, CERN, Geneva, Mar 2013.

[4] Georges Aad et al. Observation of a new particle in the search for the Standard Model Higgs boson with the ATLAS detector at the LHC. *Phys.Lett.*, B716:1–29, 2012.

[5] Georges Aad et al. Search for Supersymmetry in Events with Large Missing Transverse Momentum, Jets, and at Least One Tau Lepton in 7 TeV Proton-Proton Collision Data with the ATLAS Detector. *Eur. Phys. J.*, C72:2215, 2012.

[6] Georges Aad et al. Summary of the ATLAS experimentŠs sensitivity to supersymmetry after LHC Run 1 Ů interpreted in the phenomenological MSSM. *JHEP*, 10:134, 2015.

[7] R. Aaij et al. First evidence of the $b^0_s \to \mu^+\mu^-$ decay. Technical Report arXiv:1211.2674. CERN-PH-EP-2012-335. LHCB-PAPER-2012-043, CERN, Geneva, Nov 2012. Comments: 3+6 pages, 2 figures, submitted to Phys. Rev. Lett.

[8] R. Aaij et al. Strong constraints on the rare decays $B_s \to \mu^+\mu^-$ and $B^0 \to \mu^+\mu^-$. *Phys.Rev.Lett.*, 108:231801, 2012.

[9] B. P. Abbott et al. Observation of gravitational waves from a binary black hole merger. *Phys. Rev. Lett.*, 116:061102, Feb 2016.

[10] P. A. R. Ade et al. Planck 2015 results. XIII. Cosmological parameters. 2015.

[11] Ian Johnston Rhind Aitchison and Anthony J G Hey. *Gauge theories in particle physics: a practical introduction; 3rd ed.* Graduate student series in physics. IOP, Bristol, 2004.

[12] D. S. Akerib et al. First spin-dependent WIMP-nucleon cross section limits from the LUX experiment. 2016.

[13] B. C. Allanach. SOFTSUSY: a program for calculating supersymmetric spectra. *Comput. Phys. Commun.*, 143:305–331, 2002.

[14] B. C. Allanach and Matthew J. Dolan. Supersymmetry With Prejudice: Fitting the Wrong Model to LHC Data. *Phys. Rev.*, D86:055022, 2012.

[15] B.C. Allanach, C. Balazs, G. Belanger, M. Bernhardt, F. Boudjema, et al. SUSY Les Houches Accord 2. *Comput.Phys.Commun.*, 180:8–25, 2009.

[16] B.C. Allanach and C.G. Lester. Multi-dimensional mSUGRA likelihood maps. *Phys.Rev.*, D73:015013, 2006.

[17] Ben Allanach, Are Raklev, and Anders Kvellestad. Consistency of the recent ATLAS $Z + E_T^{\rm miss}$ excess in a simplified GGM model. *Phys. Rev.*, D91:095016, 2015.

[18] Benjamin Allanach and Fernando Quevedo. Supersymmetry and extra dimensions. lecture notes for the Cambridge mathematics tripos Part III Supersymmetry course, 2015.

[19] Johan Alwall, Michel Herquet, Fabio Maltoni, Olivier Mattelaer, and Tim Stelzer. MadGraph 5 : Going Beyond. *JHEP*, 06:128, 2011.

[20] L. Amendola and S. Tsujikawa. *Dark Energy: Theory and Observations*. Dark Energy: Theory and Observations. Cambridge University Press, 2010.

[21] E. Aprile et al. Limits on spin-dependent WIMP-nucleon cross sections from 225 live days of XENON100 data. *Phys. Rev. Lett.*, 111(2):021301, 2013.

[22] Howard Baer, Michal Brhlik, Diego Castano, and Xerxes Tata. b —> s gamma constraints on the minimal supergravity model with large tan Beta. *Phys.Rev.*, D58:015007, 1998.

[23] Howard Baer, Javier Ferrandis, and Xerxes Tata. Are supersymmetric models with large tan(beta) natural? *Phys.Lett.*, B561:145–152, 2003.

[24] Howard Baer, Eun-Kyung Park, and Xerxes Tata. Collider, direct and indirect detection of supersymmetric dark matter. *New J. Phys.*, 11:105024, 2009.

[25] Tom Banks. Supersymmetry Breaking and the Cosmological Constant. *Int. J. Mod. Phys.*, A29:1430010, 2014.

[26] R. Barate et al. Search for the standard model Higgs boson at LEP. *Phys.Lett.*, B565:61–75, 2003.

[27] E. Barberio et al. Averages of $b-$hadron properties at the end of 2006. 2007.

[28] W. Beenakker, R. Hoepker, and M. Spira. Prospino: A program for the production of supersymmetric particles in next-to-leading order qcd. 1996.

[29] E. Behnke et al. First Dark Matter Search Results from a 4-kg CF_3I Bubble Chamber Operated in a Deep Underground Site. *Phys. Rev.*, D86(5):052001, 2012. [Erratum: Phys. Rev.D90,no.7,079902(2014)].

[30] G. Belanger, F. Boudjema, A. Pukhov, and A. Semenov. micrOMEGAs 3: A program for calculating dark matter observables. *Comput. Phys. Commun.*, 185:960–985, 2014.

[31] Gianfranco Bertone, editor. *Particle Dark Matter*. Cambridge University Press, 2010. Cambridge Books Online.

[32] Milutin Blagojevic and Friedrich W. Hehl. Gauge Theories of Gravitation. 2012.

[33] Philippe Brax. Screened modified gravity. *Acta Phys. Polon.*, B43:2307–2329, 2012.

[34] Amos Breskin and Rüdiger Voss. *The CERN Large Hadron Collider: Accelerator and Experiments*. CERN, Geneva, 2009.

[35] Rene Brun and Fons Rademakers. {ROOT} - an object oriented data analysis framework. *Nuclear Instruments and Methods in Physics Research Section A: Accelerators, Spectrometers, Detectors and Associated Equipment*, 389(1Ű2):81 – 86, 1997. New Computing Techniques in Physics Research V.

[36] T. Buanes, T. Burgess, Ø. Dale, A. Kastanas, A. Lipniacka, and T. Sjursen. Search for supersymmetry in the coannihilation region with taus, jets and missing transverse energy in the final state. February 2012.

[37] Thomas Burgess, Jan Øye Lindroos, Anna Lipniacka, and Heidi Sandaker. Finding viable Models in SUSY Parameter Spaces with Signal Specific Discovery Potential. *JHEP*, 1308:098, 2013.

[38] M. Cahill-Rowley, J.L. Hewett, A. Ismail, and T.G. Rizzo. pMSSM Studies at the 7, 8 and 14 TeV LHC. 2013.

[39] Sean Carroll. *Spacetime and Geometry: An Introduction to General Relativity*. Benjamin Cummings, 2003.

[40] Serguei Chatrchyan et al. Search for $B^0\_s \to \mu^+\mu^-$ and $B^0 \to \mu^+\mu^-$ decays. *JHEP*, 04:033, 2012.

[41] S. Y. Choi. Complementarity of the CERN Large Hadron Collider and the e+ e- International Linear Collider. *Eur. Phys. J.*, C59:543–556, 2009.

[42] Timothy Clifton, Pedro G. Ferreira, Antonio Padilla, and Constantinos Skordis. Modified Gravity and Cosmology. *Phys.Rept.*, 513:1–189, 2012.

[43] Lisandro Dalcan, Rodrigo Paz, and Mario Storti. {MPI} for python. *Journal of Parallel and Distributed Computing*, 65(9):1108 – 1115, 2005.

[44] J. de Favereau, C. Delaere, P. Demin, A. Giammanco, V. Lemaître, A. Mertens, and M. Selvaggi. DELPHES 3, A modular framework for fast simulation of a generic collider experiment. *JHEP*, 02:057, 2014.

[45] Keith R. Dienes and Christopher Kolda. Twenty open questions and a postscript: Supersymmetry enters the era of the LHC. In Gordon L. Kane, editor, *Perspectives on supersymmetry. Vol.2*, pages 154–221. 2010.

[46] A. Djouadi, Manuel Drees, P. Fileviez Perez, and M. Muhlleitner. Loop induced Higgs and Z boson couplings to neutralinos and implications for collider and dark matter searches. *Phys.Rev.*, D65:075016, 2002.

[47] A. Djouadi, M. M. Muhlleitner, and M. Spira. Decays of supersymmetric particles: The Program SUSY-HIT (SUspect-SdecaY-Hdecay-InTerface). *Acta Phys. Polon.*, B38:635–644, 2007.

[48] Matt Dobbs and Jorgen Beck Hansen. The HepMC C++ Monte Carlo event record for High Energy Physics. *Comput. Phys. Commun.*, 134:41–46, 2001.

[49] Manuel Drees. An Introduction to supersymmetry. In *Current topics in physics. Proceedings, Inauguration Conference of the Asia-Pacific Center for Theoretical Physics (APCTP), Seoul, Korea, June 4-10, 1996. Vol. 1, 2*, 1996.

[50] Manuel Drees, Rohini Godbole, and Probir Roy. *Theory and phenomenology of Sparticles: an account of four-dimensional N=1 supersymmetry in high-energy physics.* World Scientific, Singapore, 2004.

[51] John R. Ellis, Toby Falk, Gerardo Ganis, Keith A. Olive, and Mark Srednicki. The CMSSM parameter space at large tan beta. *Phys.Lett.*, B510:236–246, 2001.

[52] ESA and the Planck Collaboration. sci.esa.int. http://sci.esa.int/planck/51555-planck-power-spectrum-of-temperature-fluctuations-in-the-cosmic-microwave-b

[53] Y. Fujii and K. Maeda. *The Scalar-Tensor Theory of Gravitation.* Cambridge University Press, 2003.

[54] David Galbraith. davidgalbraith.org. http://davidgalbraith.org/portfolio/ux-standard-model-of-the-standard-model/.

[55] A. Gelman, S. Brooks, G. Jones, and X.L. Meng. *Handbook of Markov Chain Monte Carlo*. Chapman & Hall/CRC Handbooks of Modern Statistical Methods. CRC Press, 2010.

[56] P. Gondolo et al. DarkSUSY: Computing supersymmetric dark matter properties numerically. *JCAP*, 0407:008, 2004.

[57] P. Gondolo et al. DarkSUSY darksusy-5.0.5. Manual and short description of routines, June 2009.

[58] M. C. Gonzalez-Garcia and Yosef Nir. Neutrino masses and mixing: Evidence and implications. *Rev. Mod. Phys.*, 75:345–402, 2003.

[59] Ø. Grøn and S. Hervik. *Einstein's General Theory of Relativity: With Modern Applications in Cosmology*. Springer-Verlag New York, 2007.

[60] UCSB Experimental Cosmology Group. www.deepspace.ucsb.edu. http://www.deepspace.ucsb.edu/planck-2013-cosmology-release-march-21.

[61] Luigi Guzzo. Large scale structure from galaxy and cluster surveys. In *Dark matter in astro- and particle physics. Proceedings, 4th Heidelberg International Conference, DARK 2002, Cape Town, South Africa, February 4-9, 2002*, pages 3–15, 2002.

[62] Greg Hamerly and Charles Elkan. Learning the k in k-means. In *In Neural Information Processing Systems*, page 2003. MIT Press, 2003.

[63] W K Hastings. Monte carlo sampling methods using markov chains and their applications. *Biometrika*, 57(1):97–109, 1970.

[64] S. Heinemeyer. Feynhiggs: History of the code. http://wwwth.mpp.mpg.de/members/heinemey/feynhiggs/history.html.

[65] Kurt Hinterbichler and Justin Khoury. Symmetron Fields: Screening Long-Range Forces Through Local Symmetry Restoration. *Phys.Rev.Lett.*, 104:231301, 2010.

[66] E. Hubble. A Relation between Distance and Radial Velocity among Extra-Galactic Nebulae. *Proceedings of the National Academy of Science*, 15:168–173, 1929.

[67] Eric Jones, Travis Oliphant, Pearu Peterson, et al. SciPy: Open source scientific tools for Python, 2001. [Online; accessed 2015-11-17].

[68] Justin Khoury. Theories of Dark Energy with Screening Mechanisms. 2010.

[69] Justin Khoury and Amanda Weltman. Chameleon fields: Awaiting surprises for tests of gravity in space. *Phys.Rev.Lett.*, 93:171104, 2004.

[70] D. Larson et al. Seven-year wilkinson microwave anisotropy probe (wmap) observations: Power spectra and wmap-derived parameters. *The Astrophysical Journal Supplement Series*, 192(2):16, 2011.

[71] Jan Ø. Lindroos, Claudio Llinares, and David F. Mota. Wave propagation in modified gravity. *Phys. Rev. D*, 93:044050, Feb 2016.

[72] Claudio Llinares and David Mota. Releasing scalar fields: cosmological simulations of scalar-tensor theories for gravity beyond the static approximation. 2013.

[73] Stephen P. Martin. A Supersymmetry primer. 1997.

[74] M. M. McKerns, L. Strand, T. Sullivan, A. Fang, and M. A. G. Aivazis. Building a Framework for Predictive Science. *ArXiv e-prints*, February 2012.

[75] Knut Dundas Morå. Dark matter searches with atlas and fermi. Master's thesis, The University of Bergen, 2013.

[76] K A Olive et al. Review of Particle Physics, 2014-2015. Review of Particle Properties. *Chin. Phys. C*, 38(arXiv:1412.1408):090001. 15 p, 2014. All tables, listings, and reviews (and errata) are also available on the Particle Data Group website: http://pdg.lbl.gov.

[77] Keith A. Olive. The Violent Universe: The Big Bang. In *High-energy physics. Proceedings, 17th European School, ESHEP 2009, Bautzen, Germany, June 14-27, 2009*, pages 149–196, 2010.

[78] Frank E. Paige, Serban D. Protopopescu, Howard Baer, and Xerxes Tata. ISAJET 7.69: A Monte Carlo event generator for p p, anti-p p, and e+ e- reactions. 2003.

[79] P. J. E. Peebles and Bharat Ratra. The Cosmological constant and dark energy. *Rev. Mod. Phys.*, 75:559–606, 2003.

[80] Michael E. Peskin. Supersymmetry in Elementary Particle Physics. In *Proceedings of Theoretical Advanced Study Institute in Elementary Particle Physics : Exploring New Frontiers Using Colliders and Neutrinos (TASI 2006)*, pages 609–704, 2008.

[81] Michael E. Peskin and Dan V. Schroeder. *An Introduction To Quantum Field Theory (Frontiers in Physics)*. Westview Press, 1995.

[82] Python Software Foundation, `https://docs.python.org/2/library/multiprocessing.html`. *multiprocessing - Process-based "threading" interface*, 2015.

[83] Torbjorn Sjostrand, Stephen Mrenna, and Peter Z. Skands. A Brief Introduction to PYTHIA 8.1. *Comput.Phys.Commun.*, 178:852–867, 2008.

[84] C. Strege, G. Bertone, F. Feroz, M. Fornasa, R. Ruiz de Austri, et al. Global Fits of the cMSSM and NUHM including the LHC Higgs discovery and new XENON100 constraints. *JCAP*, 1304:013, 2013.

[85] Gerard 't Hooft. Naturalness, chiral symmetry, and spontaneous chiral symmetry breaking. *NATO Sci. Ser. B*, 59:135, 1980.

[86] The High-Z SN Search Team. www.cfa.harvard.edu. https://www.cfa.harvard.edu/supernova//HighZ.html.

[87] WMAP Science Team. http://map.gsfc.nasa.gov/. http://map.gsfc.nasa.gov/universe/uni_shape.html.

[88] Cem Salih Ün, Şükrü Hanif Tanyıldız ı, Saime Kerman, and Levent Solmaz. Generalized soft breaking leverage for the mssm. *Phys. Rev. D*, 91:105033, May 2015.

[89] Thomas P. Waterhouse. An Introduction to Chameleon Gravity. 2006.

[90] S. Weinberg. *Cosmology*. Cosmology. OUP Oxford, 2008.

[91] Jan Øye Lindroos. Chameleon fields and compact object. Master's thesis, University of Oslo, 2009.